Scilight

Global Environmental Science

www.sciltp.com/journals/ges

Review

Support-Modulated Synergy in Dual-Atom Catalysts: Toward Rational Design and Enhanced Mechanisms for CO_2 Photoreduction

Shan Hu †, Ziyu Xia †, Quanying Li, Xiaoyan Liu and Dieqing Zhang *

The Education Ministry Key Laboratory of Resource Chemistry, Joint International Research Laboratory of Resource Chemistry, Shanghai Key Laboratory of Rare Earth Functional Materials, College of Chemistry and Materials Science, Shanghai Normal University, Shanghai 200234, China

* Correspondence: dqzhang@shnu.edu.cn

† These authors contributed equally to this work.

How To Cite: Hu, S.; Xia, Z.; Li, Q.; et al. Support-Modulated Synergy in Dual-Atom Catalysts: Toward Rational Design and Enhanced Mechanisms for CO_2 Photoreduction. *Glob. Environ. Sci.* **2026**, *2*(4), 426–470. https://doi.org/10.53941/ges.2026.100027

Publication History

Received: 13 February 2026
Revised: 5 April 2026
Accepted: 14 July 2026
Published: 21 October 2026

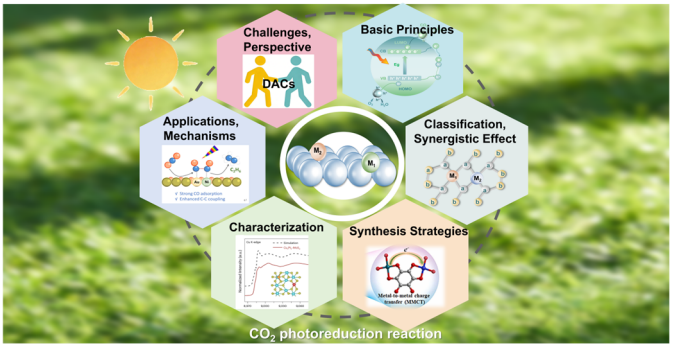
Keywords

dual-atom catalysts;
CO_2 photoreduction;
synergy effect;
support regulation

Highlights

- The superior advantages of DACs
- Catalytic performance regulatory pathways of various supports
- A comprehensive overview and a forward-looking perspective

Abstract: With the escalating global energy crisis and intensifying greenhouse effect, solar-driven photocatalytic CO_2 reduction technology for producing high-value chemicals or fuels has emerged as a highly promising and crucial strategy to address energy shortages and environmental issues simultaneously. Dual-atom catalysts (DACs), owing to ultrahigh atom utilization, flexibly tunable electronic structures, and unique dual-site synergistic effects, exhibit significant advantages in overcoming the activity limitations of conventional single-atom catalysts (SACs) and optimizing the reaction kinetics of CO_2 reduction. As an indispensable component of DACs, the support not only stabilizes the bimetallic active sites and prevents agglomeration, but also modulates the electronic states and coordination environments of the active sites through metal-metal and metal-support interactions, thereby enhancing CO_2 adsorption and activation, accelerating charge separation and transfer, and regulating reaction pathways. In this review, we systematically summarize recent advances in DACs for photocatalytic CO_2 reduction. Firstly, the design and synthesis strategies alongside advanced characterization techniques, particularly operando spectroscopies and machine learning, for DACs are discussed. Secondly, the synergistic mechanisms between dual atoms and the regulatory effects of various supports, including carbon-based materials, carbon nitride, oxides, sulfides, metal-organic frameworks (MOFs), and covalent organic frameworks (COFs), are detailed in steering CO_2 reduction pathways. Finally, the core challenges currently faced by DACs in this field are analyzed, and future development directions are prospected by integrating cutting-edge research trends. This review aims to provide theoretical guidance and technical references for the rational design and development of high-performance DACs toward efficient CO_2 photoreduction through a systematic review of existing research and exploration of mechanisms.



Copyright: © 2026 by the authors. This is an open access article under the terms and conditions of the Creative Commons Attribution (CC BY) license (https://creativecommons.org/licenses/by/4.0/).
Publisher's Note: Scilight stays neutral with regard to jurisdictional claims in published maps and institutional affiliations.

1. Introduction

Global warming poses a serious threat to human production and livelihood, and has become one of the most urgent challenges facing the world today [1]. This crisis is primarily driven by the overexploitation and consumption of fossil fuels, which have caused a continuous rise in global carbon dioxide (CO_2) emissions, resulting in a severe greenhouse effect and accelerating the depletion of energy resources [2]. Carbon neutrality, as a critical measure, can effectively mitigate global warming [3,4]. In this context, photocatalytic CO_2 reduction has emerged as a promising sustainable technology, offering a viable approach to reducing carbon emissions and promoting the carbon cycle [5,6]. The technology utilizes solar energy to convert CO_2 molecules into high-value products, including carbon monoxide (CO), methane (CH_4), methanol (CH_3OH), and ethylene (C_2H_4). Consequently, it not only helps lower atmospheric CO_2 concentrations but also produces renewable fuels, presenting a practical pathway toward a carbon-neutral cycle. As early as 1978–1979, Hemminger et al. [7] and Inoue et al. [8] discovered that under illumination, CO_2 and H_2O could react on the surface of semiconductors (e.g., $SrTiO_3$, TiO_2, WO_3, and ZnO) to generate CH_4, CH_3OH, and other carbon-containing compounds. Since then, CO_2 photoreduction has been recognized as a promising strategy for solar-to-chemical conversion. However, the photocatalytic CO_2 reduction reaction (PCO_2RR) faces significant challenges, including the high chemical stability of the CO_2 molecule with a C=O bond energy as high as 750 $kJ \cdot mol^{-1}$, insufficient active sites on the catalyst surface, rapid recombination of photogenerated charge carriers, inefficient CO_2 adsorption/activation, and sluggish reaction kinetics, resulting in low product yield and selectivity [9].

Traditional single-component semiconductor photocatalysts, owing to their single type of active site and limited space for electronic structure regulation, are difficult to simultaneously meet the requirements of CO_2 activation, charge separation, and selective conversion into specific products. The emergence of single-atom catalysts (SACs) has largely addressed the issue of low atom utilization inherent in traditional catalysts. Qiao et al. [10] reported the pioneering work on SACs in 2011. They synthesized atomically dispersed platinum on FeO_x (Pt_1/FeO_x) catalysts, which demonstrated superior activity and stability to those of traditional nanoparticles (NPs) for CO oxidation. SACs consist of isolated metal atoms serving as the active centers, along with the support as a whole. They maximize the exposure of surface metal active sites, possess unique features, including high surface free energy, quantum size effects, unsaturated coordination, and metal-support interactions, endowing them with highly uniform active centers and a tunable coordination environment [11–13]. Owing to the above characteristics, SACs exhibit unique electronic and geometric structures distinct from traditional metal NPs. Despite these numerous advantages and remarkable progress achieved, SACs still have obvious drawbacks. Since SACs contain only one specific type of active site, it is challenging to break the linear relationships between the adsorption energies of different intermediates in multi-step PCO_2RR that involves multiple active sites [14]. This limitation restricts further enhancement of the catalytic reactivity. As an extension and upgrade in the field of SACs, dual-atom catalysts (DACs) are constructed by creating two adjacent or proximate atomically dispersed metal sites (homonuclear or heteronuclear) on the support surface, forming a unique diatomic active center structure that confers unexpected properties [15–17]. The systematic development of DACs since 2010 was spurred by the pioneering synthesis and application of supported di-rhodium and di-iridium complexes by Yardimci and coworkers [18]. Subsequently, Li's group [19] contributed high-performance DACs tailored for electrocatalytic applications.

The structure of DACs not only retains the high atomic utilization inherent to SACs but also optimizes CO_2 adsorption modes, regulates the binding strength of reaction intermediates, and lowers reaction energy barriers through electronic interactions and spatial synergy between the dual-metal sites, thereby providing flexibility for tailoring the complex multi-electron CO_2 reduction reaction pathways. Furthermore, the asymmetric atomic sites in heteronuclear DACs induce a local built-in electric field due to non-uniform charge distribution, which promotes the separation and directional transfer of photogenerated charges and significantly enhances catalytic activity and product selectivity. On the other hand, the support plays a crucial role in DACs. Its surface properties, pore structure, electronic characteristics, and the provided coordination environment directly influence the dispersion, stability, and electronic state of the dual-metal sites, showing great potential in regulating catalytic performance for specific reactions [20,21]. The interaction mechanisms between different supports and dual-metal sites differ markedly, offering considerable flexibility for optimizing the performance of DACs.

Research on DACs has evolved beyond mere performance optimization toward the in-depth exploration of atomic-scale structural design and reaction mechanisms. Through advanced characterization techniques and theoretical calculations, the cooperative mechanisms between dual-atom sites, including electron transfer regulation, intermediate adsorption optimization, and reaction pathway reconstruction, are being increasingly elucidated. However, this burgeoning field remains in its infancy and faces multifaceted challenges. These include the precise synthesis and control of diatomic sites, *in situ* monitoring of active sites in complex reaction environments, enhancement of catalytic stability, and the scale-up of applications [22,23].

Herein, this review systematically summarizes the fundamental principles involved in the PCO_2RR and the

design and synthesis strategies for DACs. It emphasizes advanced characterization techniques crucial for probing atomic-scale structures and electronic states. The application of DACs with various support materials in CO_2 photoreduction is thoroughly discussed. The review elaborates on the latest research progress by delving into the synergistic mechanisms between dual atoms and the regulatory effects of different supports. Finally, it outlines the crucial challenges facing DACs and future development directions in light of current research trends. The review aims to provide theoretical guidance and technical references for the rational design of high-performance DACs with synergistic metal active sites. A schematic outline of the review is presented in Figure 1.

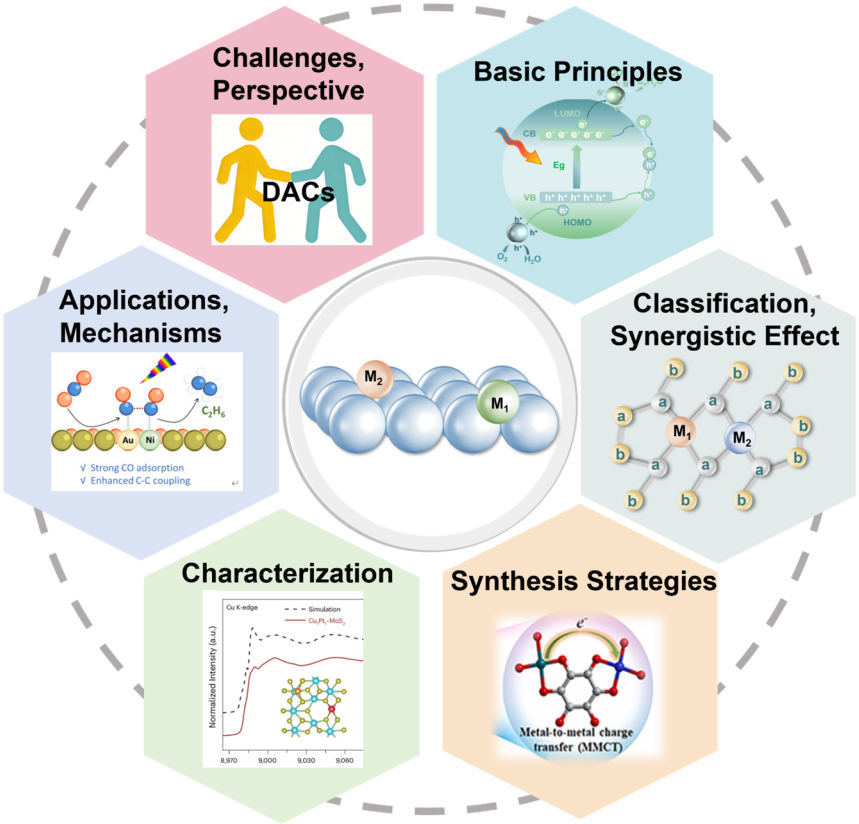


Figure 1. The schematic outline of the review.

2. Fundamental Principles of Photocatalytic CO_2 Reduction Reaction

2.1. Principle of Photocatalytic CO_2 Reduction Reaction

PCO_2RR is a solar-driven process that mimics natural photosynthesis, utilizing semiconductor photocatalysts to convert CO_2 into valuable carbon-based fuels and chemicals. The overall reaction involves multiple interconnected and sequential steps, necessitating precise regulation to ensure high efficiency. Crucially, the performance of PCO_2RR is primarily governed by three key properties of the photocatalyst: its light absorption capacity, the efficiency of charge separation/transport, and the availability and efficacy of active sites for CO_2 reduction [24,25]. As illustrated in Figure 2a, the process is initiated when a semiconductor photocatalyst absorbs incident photons with energy exceeding its band gap (Eg), exciting electrons (e^-) from the valence band (VB) to the conduction band (CB) and generating holes (h^+) in the VB. The effective separation and migration of these photogenerated charge carriers (e^- and h^+) are fundamental prerequisites for efficient catalysis in PCO_2RR. These separated charges then drive the reduction of CO_2 and oxidation of sacrificial agents, respectively. Surface modification strategies, such as metal/non-metal elemental doping, co-catalyst deposition, and heterojunction construction, are employed to enhance carrier mobility, suppress recombination, and thus improve overall performance [26,27]. Another key challenge in PCO_2RR lies in the redox potential alignment. The band edge positions of the semiconductor photocatalyst must thermodynamically encompass the specific reduction potential required for the target product, as illustrated in Figure 2b. Consequently, semiconductors with suitable band structures are crucial, as they must meet the dual requirements of strong light absorption and sufficient redox power. An ideal photocatalyst should exhibit a broad spectral response while maintaining a CB edge negative enough to drive CO_2 reduction and a VB edge positive enough to oxidize water (H_2O) or other sacrificial agents, thereby enabling efficient solar-to-chemical energy conversion.

 https://doi.org/10.53941/ges.2026.100027

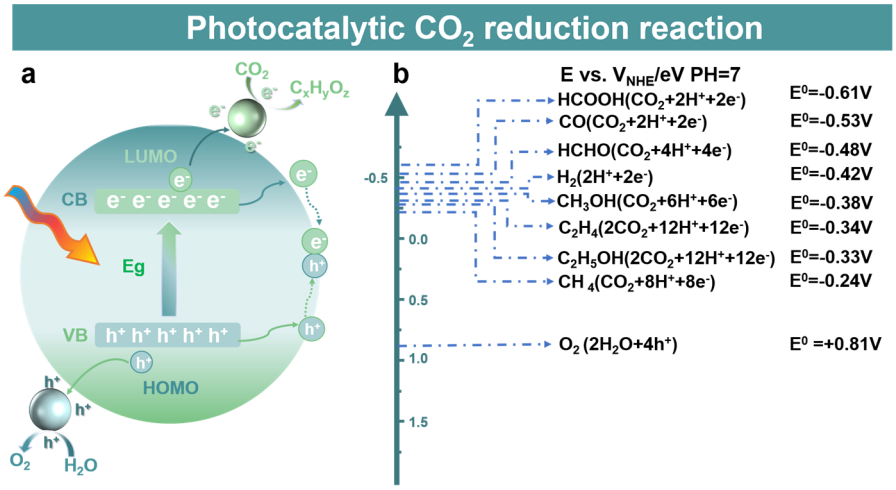


Figure 2. (**a**) Schematic of a semiconductor-based photocatalytic CO_2 reduction reaction system. (**b**) Relationship between the band positions of photocatalysts and the redox potentials for key CO_2 reduction products.

2.2. Reaction Pathways of CO_2 Photoreduction Reaction

The reaction pathway in photocatalytic CO_2 reduction is a complex multi-step process encompassing CO_2 adsorption, activation, and sequential proton-coupled electron transfer. The reaction pathway is jointly regulated by the catalyst properties, reaction conditions, and other factors [28,29]. Due to the linear molecular structure (O=C=O) and high chemical stability of the CO_2 molecule, its effective adsorption and activation require the catalyst surface to have specific reactive sites and surface properties. A critical step is the coordination interaction between the adsorbed CO_2 molecule and the active sites on the catalyst surface. This interaction is pivotal, as it directly determines the adsorption strength of CO_2. Furthermore, by modifying the electronic structure and geometry of the activated CO_2, the interaction regulates the subsequent activation energy barriers and ultimately steers the distribution of final products. Therefore, a fundamental understanding and precise control of the coordination mode of CO_2 at the active sites are essential prerequisites for achieving a breakthrough in high-performance catalytic systems from the ground up.

2.2.1. CO_2 Adsorption and Activation Modes

The CO_2 molecule forms chemical bonds with the reactive sites on the catalyst surface, resulting in changes to the molecular structure and electronic states, which are prerequisites for CO_2 activation. In current research, based on the differences in coordinating atoms, the adsorption and activation modes of CO_2 can be explicitly classified into three categories: carbon (C)-coordination, oxygen (O)-coordination, and synergistic C/O-coordination [30,31]. An in-depth mechanistic analysis of the three distinct coordination modes provides crucial guidance for the design of high-efficiency CO_2 conversion systems.

C-coordinated adsorption mode**:** The CO_2 molecule acts as an electron acceptor via its positively charged carbon atom, forming a monodentate coordinated adsorption configuration with electron-rich nucleophilic active sites on the catalyst surface (e.g., low-coordinated metal atoms or Lewis acid sites) as illustrated in Figure 3a. The feature of this interaction is direct electron transfer from the catalyst surface to the C atom of CO_2, which weakens the C=O bond and serves as an activation step for subsequent conversion [32]. This interaction can significantly elongate the C=O bond, induce strong polarization in the CO_2 molecule, and elevate the CO_2 molecule to a high-energy activated state. These changes create favorable conditions for deep reduction and C–C coupling processes. Therefore, the C-coordination mode is considered to play an important role in reaction pathways that yield multi-carbon (C_{2+}) products, such as C_2H_4 and ethanol (C_2H_5OH).

O-coordinated adsorption mode: The O-coordination mode (Figure 3b), as one of the most extensively studied activation modes, involves CO_2 binding to the catalyst surface through its negatively charged oxygen atoms, which act as electron donors to electrophilic sites (e.g., metal cations or surface hydroxyl groups). Specifically, it can be divided into O-coordinated monodentate adsorption and O-coordinated bidentate carbonate adsorption. In the O-monodentate configuration, a single oxygen atom of CO_2 coordinates with one surface site. The CO_2 molecule largely retains its linear geometry, resulting in a “terminal oxo-type” structure. In contrast, the O-bidentate carbonate configuration involves both oxygen atoms of CO_2 forming a “chelating-type” bond with two adjacent electrophilic sites. This coordination mode typically induces a pronounced bending of the CO_2 molecule and weakens the C=O bond. This bidentate mode is mostly observed on the bridging oxygen sites of metal oxides and predominantly directs the reaction pathway

toward C_1 products, such as carbon monoxide (CO) and formic acid (HCOOH).

Synergistic C/O-coordinated adsorption mode: This mode involves the bonding of the C atom and the O atom of the CO_2 molecule to the nucleophilic and electrophilic sites on the catalyst surface, respectively (Figure 3c). The configuration enables a bidirectional electron transfer, in which electrons flow from the nucleophilic site to the C atom while electron density is withdrawn from the O atom by the electrophilic site. The resulting concerted electron redistribution significantly weakens and cleaves the C=O bond, facilitating the formation of stable cyclic or chain-like intermediates. Owing to this profound activation, the synergistic C/O-coordination mode effectively steers the reaction pathway and is key to converting CO_2 into high-value products.

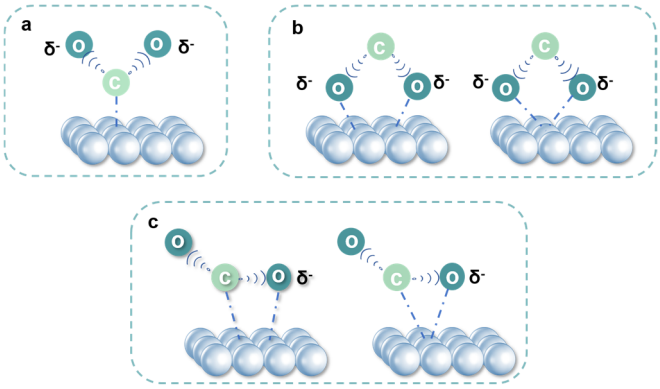


Figure 3. Representative configurations for CO_2 molecule adsorption on semiconductor catalyst surfaces. (**a**) C-coordinated, (**b**) O-coordinated, and (**c**) Synergistic C/O-coordinated adsorption mode.

The efficiency of CO_2 adsorption and activation is largely governed by the physicochemical properties of the catalyst surface. Through rationally designing and precisely modulating the catalyst surface, the interaction with CO_2 molecules can be effectively optimized, thereby enhancing overall catalytic performance. The primary strategies focus on electronic structure regulation and geometric structure engineering. In terms of electronic structure regulation, introducing heteroatoms into semiconductor catalysts is an effective approach [33,34]. For instance, the incorporation of nitrogen (N) atoms can create abundant basic sites, which strengthen the capture of acidic CO_2 molecules via acid-base interactions. Meanwhile, atoms such as O and sulfur (S) can provide additional lone electron pairs, serving as effective coordination sites to bond with CO_2 molecules. This enhances chemical adsorption and facilitates subsequent electron transfer and activation processes. In terms of geometric structure engineering, the construction of catalyst morphology and microstructure is equally crucial. Fabricating porous structures, hierarchical nanostructures, or increasing the specific surface area can significantly increase the number of exposed active sites, providing more contact interfaces for CO_2 adsorption [35,36]. Moreover, well-designed pore structures are conducive to the diffusion and mass transfer of reactants, ensuring efficient delivery of CO_2 molecules to active sites and promoting timely product desorption, thereby preventing the blocking of active sites and maintaining sustained high efficiency of the catalytic reaction.

2.2.2. Multistep Proton-Coupled Electron Transfer Reaction Pathway

After CO_2 adsorption and activation, the structurally bent and polarized CO_2 molecules undergo a series of complex proton-coupled electron transfer processes to be reduced step by step. Different intermediates and reaction pathways diverge depending on the number of electrons and protons transferred at each step, ultimately yielding a variety of products ranging from C_1 to C_{2+} species [37]. Notably, the formation of C_1 products (e.g., CO, CH_4) generally involves relatively simple proton-electron transfer steps with limited structural rearrangement, whereas the generation of C_{2+} products (e.g., C_2H_4, C_2H_5OH, and even C_3 species) requires additional C–C bond formation steps, making the reaction pathway significantly more complex and kinetically demanding. Typically, the initial single-electron reduction generates the highly reactive carbon dioxide radical anion ($CO_2^{\bullet-}$), which serves as a common pivotal intermediate for all subsequent pathways [38,39]. $CO_2^{\bullet-}$ is protonated to form different intermediates (e.g., *COOH, *CHO), which are ultimately converted into products including CO, HCOOH, CH_4, and CH_3OH. The formation of highly reduced products and C_{2+} products depends on either the further hydrogenation of *CO intermediates or C–C coupling. The *CO species can undergo sequential hydrogenation to generate intermediates like *CHO, $*CH_2O$, and $*CH_3O$, eventually leading to CH_3OH or CH_4. In contrast, the production of C_{2+} products is dominated by kinetically challenging C–C coupling steps, among which *CO dimerization (*CO-CO) and $*CO\text{-}CH_x$ coupling are widely recognized as the primary pathways. These steps involve significant activation barriers due to the need to overcome repulsive interactions and reorganize adsorbate configurations on the catalyst surface. Therefore, facilitating these coupling processes is the key to steering selectivity toward multi-carbon products. DACs exhibit a unique advantage in this regard. The presence of two adjacent metal atoms enables effective d-orbital overlap and electronic coupling, which can stabilize the transition state of *CO dimerization and significantly lower the associated energy barrier. This electronic interaction enhances the orbital hybridization between adsorbed intermediates and metal centers, thereby promoting efficient C–C bond formation. Moreover, the dual-site configuration allows for the simultaneous adsorption of two *CO intermediates at an

 https://doi.org/10.53941/ges.2026.100027

optimal distance, providing a favorable geometric arrangement for C–C coupling. This spatial confinement effect is particularly critical for overcoming the scaling limitations typically observed on SACs or extended metal surfaces. Product selectivity is governed by the intricate interplay between the principles of thermodynamics and kinetic behavior, influenced by factors such as the electronic structure of the catalyst, the nature of active sites, and the reaction environment [40]. For instance, the pH value critically affects proton availability and surface charge; acidic conditions typically favor CO generation and desorption, whereas alkaline conditions promote the formate pathway. Both temperature and light intensity directly regulate reaction kinetics and charge carrier generation rates [41]. Introducing co-catalysts can tailor the electronic structure of the catalyst surface, thereby enhancing selectivity toward target products. Furthermore, identifying the active sites where chemical reactions occur on the catalyst surface is key to understanding the reaction pathway and optimizing performance. For DACs, the catalytic performance is dictated by a synergistic combination of atomic-scale features. The electronic structure regulates the adsorption strength of intermediates, the geometric configuration influences binding modes, and the redox capability affects electron transfer efficiency [42,43]. Importantly, in the context of C_{2+} product formation, the synergistic electronic interaction between dual atoms enables differential adsorption of *CO and *CH_x intermediates on adjacent sites, effectively facilitating sequential hydrogenation and coupling steps. This bifunctional mechanism not only accelerates intermediate conversion but also suppresses competing C_1 pathways. Critically, the spatial arrangement of dual-atom sites can act as a molecular template to precisely guide C–C coupling. Their electronic synergy enables the optimized and differential adsorption of various intermediates on adjacent sites, effectively decoupling and relaying sequential reaction steps. This unique capability steers reactions along desired pathways and breaks traditional linear scaling relations to achieve highly selective conversion. Therefore, a deep understanding of the complex CO_2RR process hinges on clarifying the interplay between the atomic structure of active sites and the adsorption, activation, and transformation behavior toward key intermediates. It provides a fundamental rationale for the rational design of the catalyst structures to precisely control product selectivity.

3. Classification and Synergistic Effect of Dual-Atom Catalysts

The design of dual-metal active sites in DACs is one of the distinctive features that distinguish them from other catalysts. These two adjacent active sites can significantly enhance reactant adsorption and activation through synergistic effects. The unique structure and performance of DACs are primarily governed by several key parameters: the interatomic distance, the connection mode between sites, and the combination of metal species. Recent studies on DACs indicate that when the distance between two metal atoms is reduced to approximately 2–3 Å, significant electronic interactions occur between them. On this basis, DACs can be classified into three categories (Figure 4): DACs with metal-metal bonds (2 Å < d < 3 Å), DACs with no contact sites (3 Å < d < 15 Å), and DACs with metal sites bridged by nonmetal atoms (2 Å < d < 3 Å) [44,45]. This precisely controlled interatomic distance plays a crucial role in optimizing reactant adsorption and intermediate formation. A suitable interatomic distance enables effective electronic interactions and spatial synergistic effects between the two active sites and promotes the synergistic adsorption and conversion of reactant molecules between the two sites, thereby enhancing the catalytic efficiency.

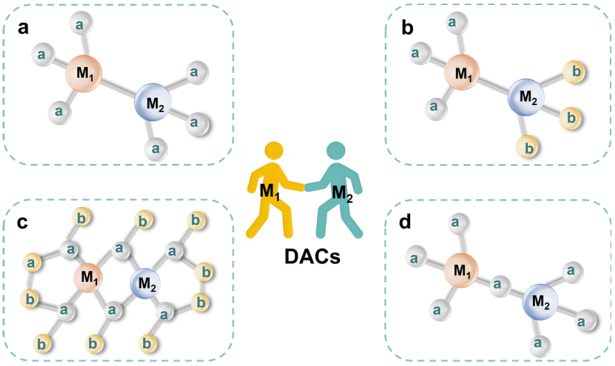


Figure 4. Three typical structures of DACs. (**a**,**b**) DACs with metal-metal bonds. (**c**) DACs with no contact sites. (**d**) DACs with metal sites bridged by nonmetal atoms. In the structural model, the dual metal centers are designated as M_1 and M_2, which may be homonuclear or heteronuclear metal atoms. The adjacent coordinating atoms are correspondingly labeled as "a" and "b", delineating the distinct coordination environment for each metal site.

3.1. Dual-Atom Catalysts with Metal-Metal Bonds

DACs featuring direct metal-metal bonds are characterized by interatomic distances typically ranging from 2 Å to 3 Å, which facilitate strong electronic interactions (Figure 4a,b). The formation of these bonds stems from the delocalization of outer valence electrons of metal atoms. At close proximity, these valence electrons are no longer confined to individual atoms but become free and shared, forming a binding force. Concurrently, the overlap of metal atomic orbitals generates bonding molecular orbitals, thereby stabilizing the metal-metal bond through a reduction in the overall energy of the system. Zhang et al. [46] employed a noncovalent assembly strategy, utilizing two types of noncovalent intermolecular forces, π-π stacking and Coulomb forces,

to spontaneously adsorb diatomic precursor molecules onto the carbon support, which were transformed into adjacent diatomic sites via thermal treatment. The resulting PtFe-DAC catalyst exhibited outstanding oxygen reduction reaction (ORR) performance. The $PtFeN_6$ site functions to reduce the electron binding energy of adsorbed O_2, increase electron density in the antibonding orbitals, and decrease O=O bond order for efficient activation. Furthermore, the introduction of Pt modulates the electronic structure of the Fe sites, evidenced by a downshifted d-band center and enhanced spin polarization, which significantly accelerates product desorption. In another work, Chen et al. [47] constructed a structurally robust and regenerable Ir_1-Cu_1 dual-atom system on a nanodiamond@graphene support (Ir_1Cu/ND@G), achieving high activity for low-temperature n-butane dehydrogenation. The superior performance of the Ir_1-Cu_1 dual-atom catalyst originates from its sterically favorable geometric configuration and modulated electronic properties, which collectively lower the C–H activation barrier, alter the rate-determining step, and facilitate product desorption. Zhao et al. [48] fabricated adjacent S/N dual-coordinated Co atoms and N-coordinated Mn atom sites, anchored in N-doped carbon support (CoN_2S-MnN_3) via an adsorption-pyrolysis process. The strong interaction within the Co–Mn diatomic pair, coupled with the orbital multi-electron filling effect induced by asymmetric charge distribution, optimizes the adsorption energy of reaction intermediates, leading to outstanding ORR activity.

3.2. Dual-Atom Catalysts with No Contact Sites

In this type of DAC, the two metal atoms are dispersed and anchored via the support without direct interatomic connection, typically maintaining a spatial distance in the range of 3 Å < d < 15 Å (Figure 4c). Although not in direct contact, when the interatomic distance falls within this specific range, the bimetallic sites can engage in indirect electronic interactions by virtue of the electron-conducting properties of the support. The coordination between metal atoms and the support induces a distortion in the electron clouds of the metal atoms. The distorted electron clouds from different metal sites can undergo weak overlap through the electron cloud of the support itself, thereby collectively influencing the adsorption and activation efficiency of reactants. This structural configuration helps prevent activity attenuation caused by atomic aggregation or structural rearrangement during catalysis. Moreover, the spatial isolation effect provided by the support maintains the stability of the geometric configuration and electronic structure of the dual active sites, ensuring sustainable catalytic performance. Chala et al. [49] developed NiCu DACs (NiCu-SACs/N-C), where Ni and Cu were atomically dispersed as $Ni–N_3$ and $Cu–N_4$ without direct bonding. Under electrolysis conditions, the isolated Cu atoms underwent a dynamic and reversible transformation into clusters, with the single-atom state recovering upon applying high voltages. The *CO intermediate generated on neighboring Ni sites created new catalytic pathways that facilitated C–C coupling, enabling the formation of oxygenated C_{2+} products. Yao et al. [50] investigated NiCu DACs on N-doped carbon (NiCu-NC) to understand how inter-metal distance affects CO_2 reduction. They first conducted theoretical predictions using various models of SACs and DACs to evaluate the impact of inter-metal interaction on the electronic structure, activity, and selectivity, revealing a distance threshold for effective inter-metal interaction. A distance threshold of approximately 5.3 Å between adjacent $Ni–N_4$ and $Cu–N_4$ moieties was revealed to trigger effective electronic regulation, which enhances both the selectivity and the activity of the CO_2 reduction reaction. These predictions were confirmed by experiments, where the DACs outperformed SACs in onset potential and selectivity. Further electronic structure analysis clarified the mechanism of the non-bonding inter-metal interaction and the synergistic effect. Hei et al. [51] pioneered the application of DACs in aqueous zinc-iodine batteries (AZIBs) to achieve high performance. Through theoretical screening of potential atomic pairs such as Mn–Zn, they successfully synthesized a MnZn–NC DAC anchored on N-doped carbon matrix. Structural characterization confirmed that the Mn and Zn atoms were coordinated as $Mn–N_4$ and $Zn–N_4$, respectively, with no direct contact. The catalyst exhibited outstanding performance, delivering a capacity of 224 mAh g^{-1} at a current density of 1 A g^{-1} and remarkable cycling stability exceeding 320,000 cycles. Mechanistic studies revealed that electrons hop along the Mn–N–Zn bridge via a spin-exchange mechanism. This process not only broadens the Mn $3d_{xy}$ band and enhances the metallic character of the catalyst to facilitate charge transfer but also upshifts the d-band center of Zn, thereby strengthening its chemical adsorption toward iodine species. This "long-distance coordination" mechanism is expected not only to effectively maintain the dispersion and structural stability of the dual-atom sites, preventing aggregation and inactivation, but also to achieve high catalytic reactivity in PCO_2RR through precise electronic regulation.

3.3. Dual-Atom Catalysts with Metal Sites Bridged by Nonmetal Atoms

In nonmetal-bridged DACs, two metal atoms are connected via a non-metal atom through covalent or coordination bonds (e.g., N, O, S, or P), forming a stable diatomic active center (Figure 4d). The non-metal atom acts as both a bridging linker and an electron-modulating site. Meanwhile, the electronegativity difference between the two metal atoms induces an asymmetric electron

 https://doi.org/10.53941/ges.2026.100027

density distribution, facilitating electron transfer between the metal centers. This electronegativity-driven charge compensation effect further enhances the adsorption and activation capabilities of the metal atoms toward reactant molecules [52,53]. Common types of such bridges include N-bridged (M–N–M), O-bridged (M–O–M), and S-bridged (M–S–M) configurations. In N-bridged systems, electrons can be transferred between the two metal atoms through the N bridge, enabling electronic synergy. In certain catalytic reactions, one metal atom adsorbs the reactant molecule, while electrons are relayed via the N atom to involve the second metal atom in the reaction, thereby promoting the catalytic process. O atoms, possessing higher electronegativity than N, exert a more pronounced influence on the electron density of the metal centers. In O-bridged DACs, the O atom not only links the two metal atoms but may also bond with O species on the support surface. This strengthens the interaction between the diatomic site and the support, fine-tuning both catalytic activity and product selectivity. It is important to note that in such DACs, despite the close spacing between M_1 and M_2, no direct metal-metal bond exists. Furthermore, partially bridged diatomic sites and fully bonded diatomic sites have similar compositions, making it necessary to use careful characterization to distinguish between them. Sun et al. [54] synthesized an atomically dispersed catalyst with novel S-bridged Cu–S–Ni sites (Cu-S-Ni/SNC) using biomass wool keratin as the precursor. The abundant disulfide bonds in wool keratin overcome the limitations of conventional gas-phase S-ligand etching processes, enabling the precise anchoring of $N_2Cu–S–NiN_2$ dual-metal sites via S bridging. In the H-cell, Cu-S-Ni/SNC exhibited a CO Faradaic efficiency (FE) of 98.1% at −0.65 V versus reversible hydrogen electrode (RHE). By leveraging the bridging S atom, the Cu-S-Ni/SNC catalyst in a flow cell achieved a high current density of 550 mA cm^{-2} at −1.00 V. The Cu site, serving as the primary adsorption center, is dually regulated by adjacent Ni and S atoms, which enhances CO_2 activation and accelerates the formation of the *COOH intermediate. Liu et al. [55] established a geometric-electronic coupled design principle through a machine learning-derived catalytic hot spot map for diatomic ORR catalysts. They found that for a certain active center atom, the highly active region in the hot spot map was narrow, providing clear guidance for the design of diatomic ORR catalysts. Based on this design, they predicted and subsequently experimentally verified a highly active Co-N-Mn/NC ORR catalyst. Structural analysis revealed that the Co-N-Mn/NC DACs comprise separate $Co–N_4$ and $Mn–N_4$ groups sharing a bridging N atom. This structure has an appropriate atomic distance to ensure that there is a verified active center interaction between the two groups. The Co-N-Mn/NC catalyst exhibited an $E_{1/2}$ of 0.90 V and a J_k of 48.64 mA cm^{-2} at 0.85 V, with a peak power density of 271 mW cm^{-2} and a specific capacity of 806 mAh g^{-1} Zn toward zinc-air battery tests.

3.4. The Synergy Effect of Dual-Atom Catalysts

The synergistic effects in DACs are mainly reflected in three interrelated aspects: the bifunctional effect, the interatomic distance effect, and the electronic effect [49,56]. In the bifunctional effect, two adjacent and chemically distinct metal atoms assume well-defined roles in the catalytic cycle. This division of labor decouples challenging sequential steps, allowing them to proceed in parallel, thereby optimizing the reaction pathway and significantly lowering the overall energy barrier. For instance, one metal site may preferentially adsorb and activate CO_2, while the neighboring site facilitates H_2O dissociation to provide the essential proton source for CO_2RR. Jiao et al. [57] constructed an asymmetric $TeN_2–CuN_3$ double-atomic site catalyst. In this design, the Te site is responsible for CO_2 activation, while the Cu center facilitates H_2O dissociation. Operando spectroscopy confirms that the two adjacent metal sites work in a cooperative yet distinct manner: Te captures and activates CO_2, and Cu helps to break the O–H bond of H_2O, providing the necessary protons for the reduction reaction. This clear division of labor synergistically lowers the energy barrier of the rate-determining step and promotes proton transfer kinetics. As a result, the $TeN_2–CuN_3$ catalyst exhibits a broad potential range, high CO selectivity, improved kinetics, and good stability in electrochemical CO_2 reduction. Another compelling example is the FeCo dual-metal site system. Single Co metal sites preferentially catalyze H_2 evolution via H_2O adsorption and O–H cleavage, whereas photoinduced conversion to Fe–Co bimetallic sites enables simultaneous H_2O dissociation and CO_2 adsorption, allowing stepwise hydrogenation to generate CO and HCOOH. By transitioning from monometallic to bimetallic sites, the competitive reaction pathways are successfully steered from H_2 evolution toward CO_2 reduction [58].

The interatomic distance effect operates from a spatial-geometric perspective. The precise distance between the two metal atoms determines whether they can optimally interact with one or multiple reaction intermediates simultaneously. When the spacing matches the bond length of the target C–C coupling intermediates (e.g., two *CO species), the diatomic site can act as a molecular template, shortening the distance between intermediates through spatial confinement and greatly facilitating the key step of C–C coupling. Meanwhile, an optimal distance also facilitates bidentate adsorption configurations for multi-atom intermediates, stabilizing key transition states. Wu and co-workers [59] constructed a trimetallic active site consisting of a Ni single atom and an adjacent Mn_2 dimer anchored on NH_2-MIL-125(Ti) nanosheets (Ni_1/Mn_2-MIL), achieving highly

selective photocatalytic CO_2 reduction to C_3H_8. The close proximity between the Ni single atom and the Mn_2 pair enables a synergistic cascade: the Ni site preferentially activates CO_2 to CO, while the neighboring Mn_2 dimer facilitates the *COCHO coupling step. Strong electronic interactions between Ni and Mn, enabled by their spatial adjacency, modulate the charge distribution and lower the formation energy barrier of the key C_3 intermediate *CH_2OCOCO. As a result, Ni_1/Mn_2-MIL delivers a C_3H_8 production rate of 32.2 μmol g^{-1} h^{-1} with an electron-based selectivity of 81.3% under sacrificial-agent-free conditions. Zhang et al. [60] constructed equidistant Pt dimer pairs on Bi_3O_4Br via aggregation of Pt-TCPP molecules, achieving efficient photocatalytic CO_2 reduction to C_2H_4. This well-defined inter-site distance enables adjacent Pt atoms to cooperatively adsorb *CO and *CHO intermediates, significantly lowering the C–C coupling energy barrier. DFT calculations reveal that the dimer configuration reduces the *COCHO formation barrier by 0.22 eV compared to single-atom sites. Experimentally, the equidistant Pt pair structure delivers an 8-fold higher C_2H_4 yield and a 10-fold increase in turnover frequency relative to single-atom counterparts. The above studies highlight the critical role of inter-site distance engineering in optimizing intermediate adsorption geometry and overcoming the kinetic bottleneck of C–C coupling for photocatalytic multi-carbon production.

The electronic effect regulates catalytic activity through electronic interactions (e.g., charge transfer, orbital hybridization) between the two metal atoms. Such interactions can collectively modulate the d-band center position of the dual-atom sites or establish internal charge transfer channels between them [61]. As a result, on the one hand, the adsorption strength of the dual-atom sites toward reactants and intermediates is tuned to the optimal range in line with the Sabatier principle, avoiding excessively strong or weak adsorption [62]; on the other hand, the formation of internal charge channels greatly accelerates the redistribution of photogenerated electrons from the support to the active sites and even between the dual sites, thus optimizing reaction kinetics and improving charge utilization efficiency [63]. A representative example of electronic synergy is the non-interacting Ni and Fe dual-atom pair sites in N-doped carbon ((Ni, Fe)-N-C DSAC). Based on theoretical simulations, the Fermi level and d-band center of the Fe atom are efficiently regulated in these non-interacting dual-atom pair sites through electronic interaction (orbital hybridization). As a result, the (Ni, Fe)-N-C DSAC exhibits superior photothermal catalytic performance for CO_2 reduction to CO, CH_4, and CH_3OH. The additional Ni atom acts as a new active site contributing to *COOH and *HCO_3 dissociation, optimizing the corresponding energy barriers and enabling specific dual reaction pathways for CO_2 reduction [64]. Cui and co-workers [65] reinforced electronic synergy in NiFe dual-atom catalysts by introducing metalloid boron to construct B, N co-coordination with polarized $(N–B)_n$ bridges. Unlike conventional N-coordinated NiFe/NC with weak electronic interaction, B, N co-coordination induces reversed electron transfer from Fe to Ni, creating an electron-enriched Ni site and an electron-deficient Fe site. This electronic redistribution synergistically promotes *COOH formation on Ni and *CO desorption on Fe, dramatically boosting CO_2 reduction. The resulting NiFe/BNC catalyst delivers 99% CO Faradaic efficiency at 200 mA cm^{-2}, far outperforming NiFe/NC. This work demonstrates that strengthening electronic synergy via heteroatom coordination is a powerful strategy for designing high-performance dual-atom catalysts.

The three effects do not exist in isolation but are interrelated and mutually reinforcing. The electronic effect lays the electronic structural foundation for synergism, while the interatomic distance effect provides the necessary spatial geometry; together, they ultimately manifest as the efficient bifunctional catalysis observed in reactions. Specifically, the synergy between electronic and geometric effects offers a promising route to break the ubiquitous scaling relations that fundamentally limit SACs. In SACs, the adsorption energies of different intermediates (e.g., *COOH, *CO, *OOH) are linearly correlated due to the single fixed coordination environment of the metal center, leading to an intrinsic trade-off that prevents simultaneous optimization of activity and selectivity. Introducing a second metal center in DACs with precisely tuned interatomic distance and electronic coupling decouples these linear correlations: one site can be engineered to bind a specific intermediate more strongly while the adjacent site binds another intermediate more weakly, effectively bypassing this scaling relation. Through purposeful design and regulation of electronic redistribution, interatomic spacing, and their synergistic interplay, comprehensive optimization from molecular adsorption and pathway selection to kinetic processes can be achieved. This constitutes the synergistic reaction mechanism underlying the high-performance catalytic conversion of DACs, offering a paradigm shift beyond the scaling relation limitations of traditional SACs.

4. Synthesis Strategies for Dual-Atom Catalysts

Compared to SACs, DACs feature two adjacent catalytic sites, allowing for precise modulation of the electronic structure of the metal active center by tuning parameters such as the composition and coordination of the metal sites. Such control is pivotal for the efficient activation and conversion of CO_2. For different catalytic reactions, the tailored design of these dual-metal active sites in DACs is essential, as it provides a fundamental platform for investigating structure-activity relationships at the molecular level and guides the design and synthesis

 https://doi.org/10.53941/ges.2026.100027

of efficient catalysts. However, at present, the precise synthesis of DACs remains challenging. In most cases, DACs are synthesized by pyrolyzing mixtures of metal salts and ligands, a process that is difficult to control. The products from such synthetic routes are often heterogeneous, containing mixtures of SACs, NPs, and DACs with poorly controlled interatomic distances. Consequently, synthesizing DACs with well-defined structures and uniformly dispersed dual-atom sites remains a significant challenge. Furthermore, the structural properties (e.g., pore structure, coordination atoms) and chemical nature of the support directly determine the loading mode and stability of the dual-metal sites. Therefore, selecting appropriate synthesis strategies based on the characteristics of different supports is crucial for stabilizing dual-metal atoms to obtain well-defined DACs. We systematically introduce several synthesis strategies for DACs. Each method possesses distinct advantages and limitations, making each approach typically suitable for particular catalytic systems. It is important to recognize that achieving the precise construction of target dual-atom sites often necessitates the integrated and synergistic application of multiple synthetic approaches.

4.1. Precursor Pyrolysis Method

The precursor pyrolysis method is a mainstream approach for preparing carbon-based DACs (e.g., on graphene, carbon nanotubes, N-doped carbon, etc.). It involves mixing metal-containing precursors with carbon sources, followed by high-temperature pyrolysis under a controlled atmosphere to achieve atomic-level dispersion and stable anchoring of dual-metal sites. The key to this method lies in precisely regulating the ratio between metal precursors and the pyrolysis conditions to prevent metal agglomeration into clusters or NPs [66]. A representative example is the work by Mo et al. [64], who employed a Ni- and Fe-containing metal-organic complex as a precursor and performed pyrolysis under an inert atmosphere to prepare (Ni, Fe)-N-C DACs with dual sites of Ni–N_4 and Fe–N_4 (Figure 5a). Critically, the Ni–N–N–Fe configuration formed during pyrolysis ensures stable dispersion and maintains an appropriate spatial distance between the dual-metal sites. Among various parameters, pyrolysis temperature is a decisive factor in forming well-defined dual-atom sites. Excessively low temperatures may lead to incomplete precursor decomposition, resulting in unstable metal species, whereas overly high temperatures can induce metal atom migration and agglomeration. Therefore, precise control over the pyrolysis temperature, including the heating rate and holding time, is essential for optimizing the dual-site structure. Furthermore, heteroatoms (e.g., N, P, S) introduced into the carbon source can form strong coordination bonds with the metal atoms, providing additional stabilization for the dual-atom sites. Zhang et al. [66] recently proposed a general synthetic strategy for preparing homonuclear (Fe_2, Co_2, Ni_2, Cu_2, Mn_2, and Pd_2) and heteronuclear (Fe_1Cu_1, Fe_1Ni_1, Cu_1Mn_1, and Cu_1Co_1) DACs. They employed a macrocyclic precursor-mediated encapsulation-pyrolysis approach, which preserves the main framework of the molecular precursor during pyrolysis. A Robson-type binuclear complex (M^1M^2L) serves as the precursor and is first encapsulated in the pores of a zeolitic imidazolate framework (ZIF-8). Subsequent pyrolysis of the M^1M^2L@ZIF-8 composite leads to carbonization, producing the target M^1M^2-DAC. It should be pointed out that this pyrolysis method can cause some active metals to be incorporated into the support matrix, which could limit their availability during catalysis.

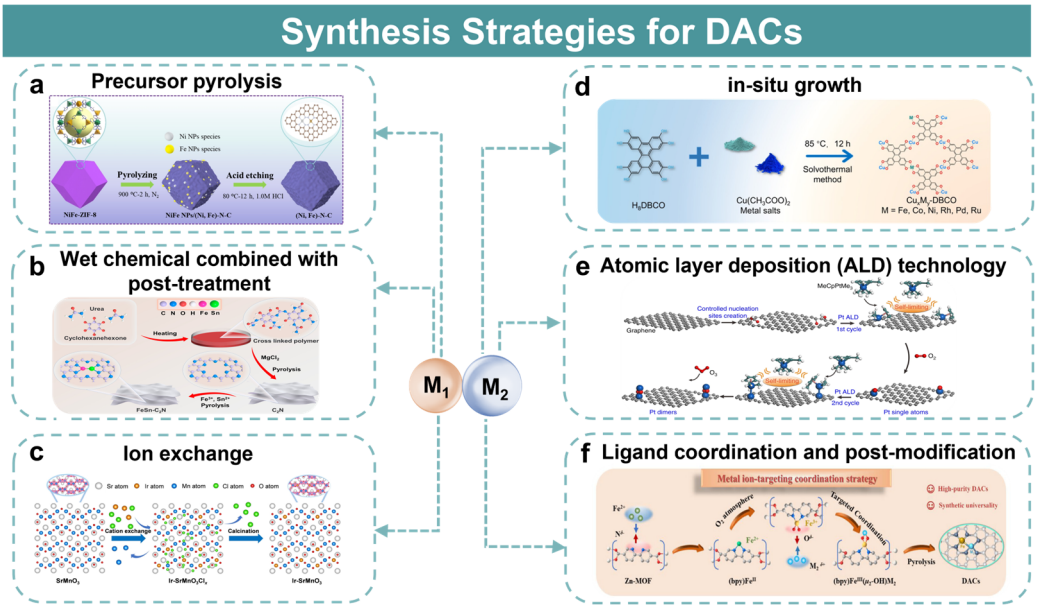


Figure 5. (**a**) Schematic illustration of (Ni, Fe)-N-C DSAC with adjacent Ni–N_4 and Fe–N_4 sites. Reprinted with permission from Ref. [64]. Copyright 2023, Wiley-VCH GmbH. (**b**) Schematic illustration of the Synthesis for the FeSn-C_2N Catalyst.

Reprinted with permission from Ref. [67]. Copyright 2024, American Chemical Society. (**c**) Schematic illustration of Ir-$SrMnO_{3-x}$ synthesis process. Reprinted with permission from Ref. [68]. Copyright 2024, Wiley-VCH GmbH. (**d**) Schematic illustration on the preparation of Cu_xM_y-DBCO MOFs catalysts. Reprinted with permission from Ref. [69]. Copyright 2025, American Chemical Society. (**e**) Schematic illustration of bottom-up synthesis of dimeric Pt_2/graphene catalysts [70]. (**f**) Metal ion-targeting coordination strategy to prepare DACs. Reprinted with permission from Ref. [71]. Copyright 2025, Wiley-VCH GmbH.

4.2 Wet Chemical Method Combined with Post-Treatment

The wet chemical method achieves uniform immobilization of metal precursors onto the support surface through solution-phase chemical reactions, followed by post-treatments (e.g., reduction, annealing) to form atomically dispersed dual sites. This approach typically involves multi-step sequential processes [72]. First, the support is immersed in a metal precursor solution, and then the metal species are introduced via impregnation, ion exchange, co-precipitation, or deposition-precipitation. Subsequently, a series of post-treatments, including centrifugation, drying, and pyrolysis, are performed to obtain atomic-scale catalysts. A representative application of this strategy is demonstrated by Yan et al. [73]. They loaded Ni and W salt precursors onto the surface of polymeric carbon nitride (CN) nanosheets via a wet chemical route. Subsequent calcination and reduction in a hydrogen-argon mixed atmosphere yielded Ni-W/CN DACs. By precisely controlling the precursor concentration and calcination temperature, the method achieved atomic-scale dispersion of Ni–N_4 and W–N_4 dual sites on the CN surface. The optimal Ni-W/CN catalyst exhibited significantly enhanced performance for photocatalytic CO_2-to-CO conversion (80.4 μmol g^{-1} h^{-1}), up to 10.5 times higher than that of pure CN. In another study, Chen et al. [74] loaded iridium ($IrCl_3$) and tungsten (ammonium paratungstate) precursors onto a defect-rich CeO_2 support via a wet-chemical co-impregnation method. After calcination at 400 °C, a dual-atom Ir-W_x/CeO_2 catalyst was formed. By fine-tuning the precursor ratio and calcination conditions during post-treatment, the distribution of the dual-atom sites and the catalytic performance were optimized. This led to a synergistic enhancement in both activity and selectivity for the selective oxidation of ammonia (NH_3). Liu et al. [75] adopted a wet-chemical method to load ruthenium (Ru) and copper (Cu) precursors onto N-doped graphene aerogel (NGA). A subsequent microsecond pulsed discharge post-treatment technique was applied, inducing the instantaneous high-temperature decomposition of the metal salt nanocrystals. This rapid process facilitated the atomic-level dispersion and anchoring of Ru and Cu atoms at defect sites within the NGA nanopores, forming an asymmetric Ru–N–Cu–N coordination active center. The RuCu DAs/NGA catalyst exhibited outstanding performance in the electrocatalytic reduction of nitrate to NH_3 at −0.4 V vs. RHE, achieving a FE for NH_3 of 95.7% and a high yield rate of 3.1 mg h^{-1} cm^{-2}, along with long-term operational stability.

The impregnation method, as a common wet-chemical approach, involves immersing a semiconductor oxide support featuring surface oxygen vacancies (e.g., TiO_2, ZnO, CeO_2, etc.) into the precursor solution containing two types of metal ions. Through adsorption, the metal ions are loaded onto the support surface, followed by drying, calcination, and reduction treatments to form dual-atom sites. The success of this method hinges on precise control over the concentration and pH of the impregnation solution, which directly regulates the adsorption amount and dispersion uniformity of the metal ions on the support surface. Excessively high metal ion concentrations often result in overloading and the formation of metal NPs, while maintaining an appropriate pH (typically between 4 and 6) can enhance the interaction between metal ions and surface hydroxyl (–OH) groups on the support, thereby improving dispersion. For example, Wang et al. [67] prepared a C_2N support with uniform N_6 cavities and edge-N unsaturated characteristics through the high-temperature pyrolysis of cyclohexanone and urea catalyzed by $MgCl_2$, creating favorable conditions for metal anchoring. Subsequently, Fe and Sn metal salts were introduced using a wet impregnation method, followed by a second pyrolysis step, which successfully yielded FeSn-C_2N DACs (Figure 5b). This achieved the orderly anchoring of Fe and Sn atoms within the N_6 cavities, constructing a stable structure. In a related advancement, Wang et al. [76] achieved controllable regulation from Co NPs to CoN_4 single atoms to Co_2N_5 dual atoms using an atomization and sintering strategy based on an N-stripping and thermal-migrating process. This strategy was successfully extended to fabricate 22 distinct types of DACs. Mekkering et al. [77] successfully prepared stable Pt DACs via a wet impregnation method using specific precursors under controlled drying and calcination conditions. Leveraging the synergy of the dual-atom sites, one Pt atom activates H_2O while the other binds NH_3BH_3, thereby increasing the supply of protonic hydrogen and hydronium ions and enhancing H_2O activation to boost the reaction. To further improve the dispersion of metal precursors, several support pretreatment and modification strategies are employed. Additionally, the carbon support can be pretreated (e.g., via oxidation or plasma treatment) to introduce oxygen-containing functional groups (–COOH, –OH), strengthening its interaction with metal ions. Alternatively, heteroatom doping or the intentional

creation of defects on the support promotes strong metal–support interactions and suppresses metal particle agglomeration [78,79]. There are also some reported works that adopt chelating agents, such as ethylenediaminetetraacetic acid (EDTA) and citric acid, to form stable complexes with metal ions, avoiding the agglomeration of metal ions during the loading process and improving the uniformity of dual-atom sites [80–82].

4.3. Ion Exchange Method and In Situ Growth Method

The ion exchange method is a widely employed strategy for preparing DACs. By exchanging target metal ions with the exchangeable cations in the support, it achieves uniform dispersion and anchoring of bimetallic atoms on the support, thus precisely constructing dual-atom active sites [83,84]. A novel Ir–Mn dual-atom electrocatalyst was synthesized by Liu et al. [68] via a facile ion-exchange method, where Ir was incorporated into $SrMnO_3$ (Figure 5c). The resulting catalyst exhibited exceptionally high activity and stability toward the OER. The ion exchange process proceeded in a self-limitation way, which favored the formation of Ir–Mn dual atoms within the $IrMnO_9$ unit. The incorporation of Ir modulates the electronic structure, endowing the adsorbed *O intermediates with parallel spin alignment, thus facilitating the direct coupling of the two adsorbed *O intermediates, and promoting O_2 release via the oxygen-oxygen radical coupling mechanism. In another study, Chen et al. [85] precisely introduced Ce atoms into the Cu-SSZ-13 zeolite framework via an ion exchange method, successfully constructing the Ce-Cu-SSZ-13 catalyst with Cu–Ce dual-atom sites. The precise localization of Ce species within the eight-membered rings (8MRs) leads to the formation of $[ZCe^{3+}(OH)_2]^+$ species, which in turn converts the phosphorus-sensitive $[ZCu^{2+}OH]^+$ sites into phosphorus-insensitive Z_2Cu^{2+} sites. The Ce-Cu-SSZ-13 catalyst can still maintain 90% NO_x conversion and 100% N_2 selectivity even at a low temperature of 210 °C, exhibiting excellent phosphorus tolerance.

The *in situ* growth method involves the direct formation of dual-atom active sites on a specific support through controlled chemical or physical processes of precursors on its surface. By precisely regulating parameters such as concentration, temperature, and atmosphere, metal atoms of the precursors form specific coordination structures on the support surface, thus realizing precise regulation. Generally, bimetallic precursors are synchronously introduced during the preparation of semiconductor oxides, allowing for the one-step fabrication of DACs. This approach offers precise control over the doping concentration and distribution of dual metal sites, minimizes metal agglomeration that can occur in subsequent loading steps, and ultimately enhances both the activity and stability of the catalyst. Yan et al. [86] reported a strategy for synthesizing dual-atom iron catalysts (Fe_2/NC) via *in situ* generation of Fe_2Cl_6 (g) dimers from $FeCl_3$ (s) followed by direct sublimation conversion. First, N-doped carbon (NC) was prepared by pyrolyzing ZIF-8, during which Zn evaporated, creating a porous support to immobilize Fe. Next, a mixture of anhydrous $FeCl_3$(s) and NC was heated to 300 °C under the Ar atmosphere. This step facilitated the sublimation of $FeCl_3$, the formation of Fe_2Cl_6 vapor, and its subsequent capture by the NC support. Finally, the Fe_2Cl_x/NC synthetic intermediate was collected and heated at 300 °C under a 5% H_2 atmosphere to remove Cl ligands on Fe sites. This treatment effectively stabilized Fe dimers and promoted their bonding with N sites on the NC, thus forming well-defined Fe_2/NC. Li et al. [69] used conductive metal-organic frameworks (CMOFs) as templates to construct Cu-Ni DACs via the *in situ* growth method (Figure 5d). This approach leverages the high conductivity and stability of CMOFs to achieve uniform dispersion of Cu and Ni atoms, forming well-defined dual-atom active sites and realizing efficient electroreduction of nitrate to NH_3.

4.4. Atomic Layer Deposition (ALD) Method

Atomic layer deposition (ALD) method is a thin-film deposition technique that relies on self-limited processes in which precursor gases are introduced to a support and form atomic-scale layers on the surface [87,88]. This bottom-up approach could uniformly and precisely construct catalytic sites and is particularly advantageous for synthesizing atomically dispersed catalysts. ALD generally utilizes gas-phase reactions between metal precursors and a solid support. Yan et al. [70] successfully synthesized a DAC with Pt_2 dimers via a "bottom-up" approach using ALD technology (Figure 5e). To deposit Pt atoms, graphene with a large specific surface area was treated with acid oxidation to form isolated phenol or phenol-carbonyl pairs on its surface as nucleation sites. Subsequently, Pt atoms were deposited stepwise by alternately exposing the graphene to trimethyl(methylcyclopentadienyl)platinum(IV) ($MeCpPtMe_3$) and molecular O_2, ultimately constructing the Pt_2/graphene structure. Guo et al. [89] recently reported fabricating atomically dispersed transition-metal-modified Pt-based bimetallic catalysts using the ALD method. Through precisely depositing transition metals onto Pt single-atom sites, the modulation effects of different metals on the electronic structure of Pt were systematically revealed, and the associated mechanisms in CH_3OH steam reforming and water-gas shift reactions were clarified. Chen et al. [90] reported that by regulating the steric hindrance between metal precursors using ALD technology to control the Pt_1-Ni_1 interspace, the Pt_1Ni_1/C_3N_4 DACs can be precisely synthesized. The C_3N_4 nanosheet support was exposed at and cycled with 200 °C and under N_2 purge with trimethyl (methyl

cyclopentadienyl)-platinum ($MeCpPtMe_3$) and nickelocene ($NiCp_2$), respectively. The direct nucleation of $NiCp_2$ on Pt sites is inhibited due to steric hindrance between chemisorbed $MeCpPtMe_3$ and $NiCp_2$ precursors. Finally, O_3 was used to remove the ligands of chemisorbed precursors, leading to the formation of Pt_1Ni_1/C_3N_4 DACs.

4.5. Ligand Coordination Method and Post-Modification Method

The ligand coordination method is one of the pivotal approaches for synthesizing DACs. It exploits strong interactions between specific ligands and metal ions to anchor two metal atoms at the defined positions via ligand bridging or coordination, thereby forming dual-atom active centers [91,92]. The core of this method lies in selecting suitable ligand-metal ion combinations. Crucially, the spatial structure of the ligand must precisely regulate the distance between the dual-metal sites to prevent the formation of metal-metal bonds and subsequent agglomeration. The MOF-supported DACs are predominantly based on the ligand coordination principle. By leveraging functional groups within the MOF ligands (e.g., –COOH, –OH, or N heterocycles) to simultaneously coordinate with two different metal ions, MOF-based DACs featuring well-defined dual-atom sites can be constructed. A notable example is the work of Wang et al. [71], who proposed a metal-ion-targeted coordination (MITC) strategy, distinct from conventional high-temperature pyrolysis (Figure 5f). This approach employs a bipyridine (bpy) ligand coordinated to a primary metal (M_1) to construct an artificial monooxygenase-like structure, (bpy)$M_1(\mu_2$-OH). The electron-rich O atom serves as an anchoring site for a secondary metal (M_2). During subsequent pyrolysis, the pre-formed M_1–O–M_2 O-bridged configuration in the formed (bpy)$M_1(\mu_2$-OH)M_2 precursor facilitates the precise synthesis of the target heteronuclear DACs. In a recent study, Ma et al. [93] proposed a ligand confinement method, in which two metal precursors are simultaneously coordinated by diamine ligands on graphitic carbon nitride (g-C_3N_4), enabling the fabrication of both homonuclear and heteronuclear DACs with precisely controllable interatomic spacing. The pairing rate exceeded 82%, significantly higher than previously reported levels. By varying the diamine chain length, the atomic spacing could be precisely tuned within a range of 0.22 to 0.81 nm. Taking Pt_1-Au_1/g-C_3N_4-HA as an example, its activity in nitrate reduction to NH_3 reached 744 mg h^{-1} mg_{metal}^{-1}, markedly higher than the 255 mg h^{-1} mg_{metal}^{-1} of the unpaired system, validating the universality and application potential of this strategy.

The post-modification method is also commonly used to synthesize MOF-supported DACs. This method involves first introducing a primary single-atom site, followed by introducing a secondary metal precursor to establish direct metal–metal interactions. These interactions ensure the formation of the desired atomic pair structure during subsequent pyrolysis, thereby successfully constructing the DACs. For example, Zhou et al. [94] used tetrahydroxyquinone (THQ) as the ligand to coordinate transition metals with Cu ions and THQ ligands, constructing highly active atomically dispersed CuM-THQ (M = Co, Ni, Fe) sites on two-dimensional MOF supports. The –OH groups in the THQ ligand form stable coordination structures with the metal ions, ensuring the isolated dispersion and uniform distribution of the Cu–M dual sites. This method allows for precise control over the loading amount of the second metal, avoids competitive coordination between the two different metal ions during synthesis, and significantly enhances the controllability of the dual-atom sites. Wang et al. [95] reported a distinct post-modification strategy for the precise construction of DACs. By introducing metal-metal bond interactions, a stable dual-metal atomic structure was pre-constructed in the precursor. This reduces the uncertainty associated with the formation of dual-atom sites during the calcination process, thereby enabling the precise construction of DACs.

4.6. Other Synthetic Methods for Dual-Atom Catalysts

In addition to the synthesis methods mentioned above, researchers have also developed various other techniques for preparing DACs, such as a simple ball milling method, atom trapping method, metal ion adsorption strategy, and seed-mediated strategy, among others [44,96,97]. Wang et al. [98] redispersed Co atoms (0.23 wt%) from Co powder and anchored them on S, N co-doped carbon (SNC), where the Co–S forms dual-atom sites for benzylamine self-coupling (Figure 6a). Zhou et al. [99] employed the atom trapping method to prepare Pt_1Pd_1/CeO_2 DACs (Figure 6b). The as-prepared CeO_2 nanospheres were reduced to generate O vacancies, after which Pt_4^+ and Pd_2^+ precursors were introduced into the CeO_2-containing solution. A multi-step heat treatment then yielded strongly coupled Pt and Pd atoms situated at adjacent positions in Pt_1Pd_1/CeO_2. Jin et al. [100] developed a selective etching and metal ion adsorption strategy to accurately assign a second metal atom (M^2) adjacent to the single-atom site (M^1-N_x) for constructing diatomic sites (e.g., Fe-Pd, Fe-Pt, Fe-Ru, Fe-Zn, Co-Fe, Co-Ni, and Co-Cu, Figure 6c). The hydrogen peroxide selectively etches the positively charged carbon atoms near the M^1-N_x moiety (denoted as α-C) and produces a vacancy, which could capture the M_2 metal ions during the subsequent adsorption step. The DACs showed optimized electronic structure and enhanced OER activity. Zhang et al. [101] proposed a novel seed-mediated strategy and successfully constructed the Ag_1-Pd_1/CeO_2 catalyst with a well-defined Ag_1-Pd_1 dual-atom configuration. The approach involved first synthesizing Pd_1/CeO_2 SACs using K_2PdCl_4 as the

 https://doi.org/10.53941/ges.2026.100027

precursor. Subsequently, the residual Cl species bonded to isolated Pd_1 sites in the Pd_1/CeO_2 catalyst were utilized to achieve the directional adsorption of Ag^+. During the calcination process, the interaction between Pd–Cl–Ag promoted the formation of the Ag_1–Pd_1 dual-atom configuration, which effectively avoided the random dispersion of the two types of single atoms on the CeO_2 surface, ensuring the precise construction of paired sites.

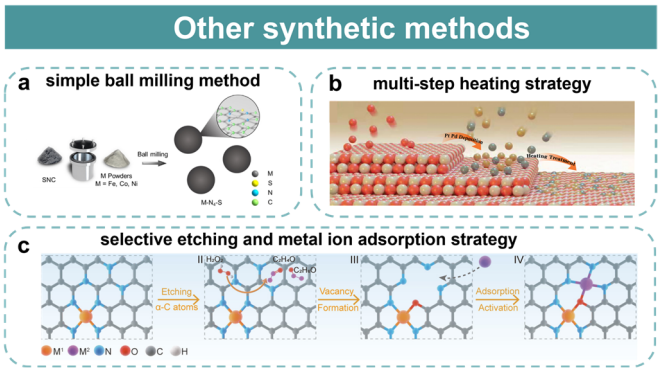


Figure 6. (**a**) Schematic illustration of the developed ball-milling approach. Reprinted with permission from Ref. [98]. Copyright 2021, Wiley-VCH GmbH. (**b**) Schematic illustration of the developed multi-step heating strategy for synthesizing Pt-Pd SAC-2. Reprinted with permission from Ref. [99]. Copyright 2022, Wiley-VCH GmbH. (**c**) Schematic illustration depicting the synthesis of DACs via H_2O_2 etching of α-C (phase II) to form a vacancy (phase III) and adsorption of second metal ions and subsequent activation by carbonization (phase IV). Reprinted with permission from Ref. [100]. Copyright 2025, American Chemical Society.

In addition, researchers have developed various other approaches for preparing DACs, ranging from scalable synthesis to precise atomic-level pairing. For instance, Wang et al. [76] reported a general NP-to-SA-to-DA atomization and sintering strategy, in which metal nanoparticles were first converted into single atoms and subsequently reorganized into dual-atom sites through thermal migration and N-leaching. This approach enabled the scalable synthesis of 22 different DACs, including Co_2N_5, Fe_2-N-HCS, and Ni_2-N-HCS, with excellent multifunctional ORR/OER/HER performance and long-term stability. Another representative method is the ligand-restricted strategy, in which flexible diamine ligands in solution preassemble two metal precursors into a "metal-ligand-metal" complex, which is then anchored onto a 2D carbon nitride support and thermally treated to remove excess ligand. This method produces high atomic pairing (>82%) and tunable interatomic distances, as demonstrated for Pt_1-Au_1 and Pt_1-Ni_1 DACs, achieving nearly threefold higher catalytic activity in nitrate-to-ammonia conversion than unpaired catalysts [93]. Collectively, these strategies highlight the versatility of DAC synthesis, bridging the gap between scalable production and precise atomic engineering, and offering generalizable pathways for designing high-performance multifunctional dual-atom catalysts.

The precise synthesis of DACs hinges on constructing a synergistic compatibility between the support and the dual-metal sites, a factor that directly dictates the catalytic activity, selectivity, and stability. The support must simultaneously ensure the stable anchoring and electronic modulation of the metal sites, while the dual atoms optimize the local reaction environment on the support surface through synergistic effects, thereby forming an integrated and functionally complementary system [102]. However, the precise regulation of electron transfer and synergistic catalysis between the support and diatomic sites remains a significant challenge, owing to the complex interplay of multiple factors such as support properties, diatomic combinations, and coordination environments. Consequently, creating specific binding sites for two metal atoms on the support surface is of paramount importance. Essential strategies include leveraging the electron transfer between the support and diatomic sites to modulate the electron density of active centers, as well as utilizing inherent support defects or engineered functional groups to synergistically optimize the reaction pathway. Employing a single synthetic strategy often proves inadequate for precisely controlling the concurrent adsorption and nucleation of two distinct metal precursors on the support, easily leading to mixtures of single atoms, clusters, or NPs, causing complicated structure-activity relationships. Therefore, it is imperative to thoroughly consider the metal/electron-support interaction, understand PCO_2RR pathways, and select appropriate synthetic strategies to tailor the local coordination environment of the dual-metal atoms.

5. Characterization of Dual-Atom Catalysts

The catalytic performance of DACs is highly dependent on their fine structure at the atomic scale. Specifically, parameters including the elemental identity of the metal sites, the local coordination environment (coordination number, ligand type), the precise interatomic distance, and the synergistic interaction mode between the dual sites play a crucial role in determining catalytic performance. The electronic state of the metal centers (e.g., oxidation state, spin state, charge distribution) collectively governs the catalytic behavior. This unique set of atomic-scale parameters constitutes a distinct "structural fingerprint" for the DACs. Consequently, the development of high-resolution, multi-dimensional, and accurate characterization techniques is of paramount importance for elucidating the structure-activity relationships and catalytic mechanisms of DACs, thereby guiding the rational design of DACs. Furthermore,

there is an urgent need to develop and integrate a suite of advanced characterization techniques capable of providing high spatial resolution and multi-dimensional chemical information at the atomic scale, while also allowing for *in situ* or operando observations under realistic reaction conditions. This chapter systematically introduces the crucial characterization methods for DACs, focusing on two primary dimensions for structural characterization and performance evaluation. Regarding structural characterization, the emphasis will be placed on addressing the following key issues: (1) Atomic-scale structure confirmation: direct observation and confirmation of the existence, location, and arrangement of isolated single-atom or dual-atom metal sites; (2) Electronic structure analysis: clarification of the oxidation state, coordination/bonding characteristics, and localized electronic environment of the metal active center; (3) Dynamic behavior monitoring: tracking the structural evolution of active sites and the formation/transformation of reaction intermediates in real time during catalytic processes.

The commonly used characterization techniques for DACs can be mainly classified into the following categories. Electron microscopy techniques, such as aberration-corrected scanning transmission electron microscopy, AC-STEM can directly achieve atomic-level imaging. X-ray spectroscopy techniques, covering X-ray absorption near-edge structure (XANES) and extended X-ray absorption fine structure (EXAFS), can provide element-specific electronic structures and coordination information. Other spectroscopic methods, including *in situ* Fourier transform infrared (FTIR) spectroscopy, Raman spectroscopy, X-ray photoelectron spectroscopy (XPS), and Mössbauer spectroscopy, are used for detecting surface species and reaction mechanisms. These highly sensitive techniques for characterizing dual-atom structures complement each other and together constitute indispensable tools for understanding the intrinsic relationship between the structure and performance of DACs.

5.1. Structural Characterization Techniques

5.1.1. Electron Microscopy Technology

Nowadays, aberration-corrected high-angle annular dark-field scanning transmission electron microscopy (AC-HAADF-STEM) is widely used to directly investigate the existence state of the metal species in DACs [103,104]. The AC-HAADF-STEM images are based on the atomic number (Z)-dependent contrast imaging principle, which enables the clear visualization of the dual-metal atom sites dispersed on the support surface (displayed as bright dots) and the direct confirmation of their atomic-scale dispersion characteristics. Through quantitative analysis of the images, the distance between adjacent dual-atom sites, the spatial arrangement, and the distribution density on the support surface can be further accurately determined, providing intuitive structural evidence for understanding their synergistic effects. By combining scanning transmission electron microscopy-electron energy loss spectroscopy (STEM-EELS) with atomic-level spatial resolution, it is possible to acquire element-specific EELS spectra at the same atomic locations imaged by AC-HAADF-STEM. This enables the acquisition of key chemical information about the metal sites, such as their local electronic structure, coordination atoms, and oxidation state. For instance, in the AC-HAADF-STEM images of the T-FeCo-N-C DACs by Yuan et al. [105], the isolated bright dots corresponding to atomically dispersed Fe and Co sites can be clearly observed (Figure 7a–c). To further determine the composition of the atomic pair, EELS was performed at the location indicated by the blue circle. The EELS spectrum shown in Figure 7d exhibits two peaks at 709.4 eV and 779.1 eV, corresponding to Fe and Co, respectively, providing preliminary confirmation of the presence of Fe–Co dual-atom pairs. Elemental mapping results further confirmed that the distribution of Fe and Co atoms is nearly uniform (Figure 7e).

Furthermore, transmission electron microscopy (TEM) can be used to observe the overall morphology of DACs and the microstructure of the support, such as nanosheets, regular crystals, or the pore structure, providing visual evidence of the structural features that anchored the dual-atom sites. Scanning electron microscopy (SEM) is primarily employed to characterize the macroscopic morphology and particle size distribution, aiding in the assessment of the dispersion of DACs. As an advanced tool for DAC characterization, environmental transmission electron microscopy (ETEM) combines atomic-level resolution with the capability to simulate near-realistic reaction conditions. This allows for a comprehensive analysis that bridges static structure with dynamic mechanistic insights under controlled atmospheres or during reactions. Under static conditions, ETEM can directly image and confirm the precise positions, coordination configurations, bonding states, and spatial arrangements of dual-atom active sites, effectively distinguishing them from impurities such as single-atom sites or metal nanoparticles. More importantly, by introducing reaction gases and applying specific conditions such as heating within the ETEM chamber, researchers can observe in real time and *in situ* the dynamic evolution of metal active sites under realistic reaction conditions. ETEM enables the direct observation of key dynamic processes, such as metal atom migration, transient reconstruction of active sites, and irreversible agglomeration leading to deactivation. Correlating this dynamic structural evolution with real-time catalytic performance provides in-depth insights into the structure-property relationships of DACs. This understanding is crucial for the rational design of high-performance and highly stable catalysts.

 https://doi.org/10.53941/ges.2026.100027

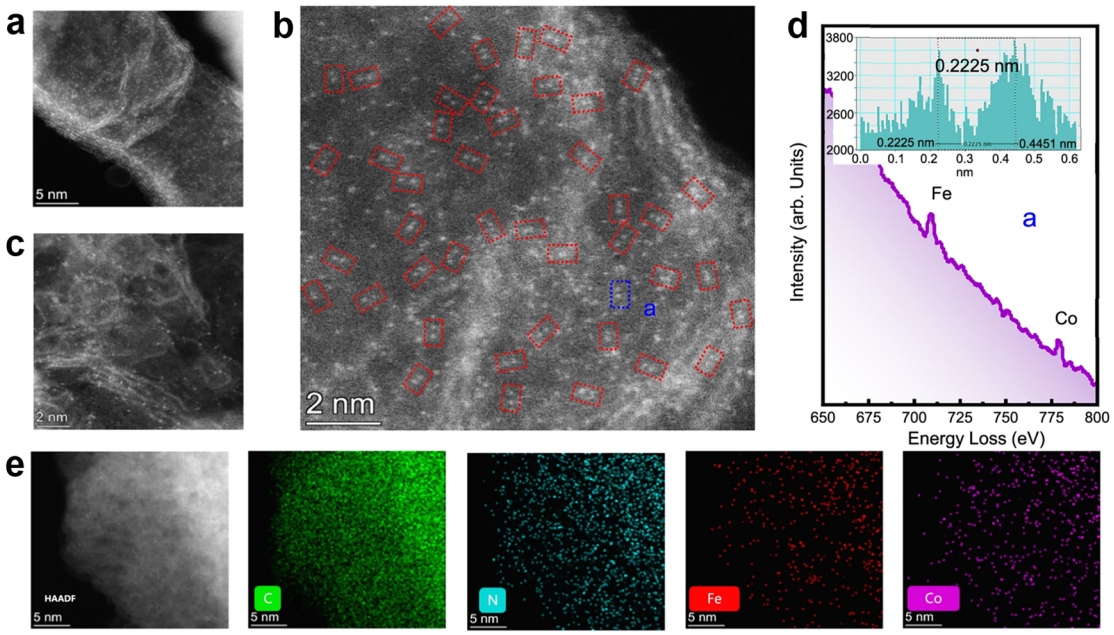


Figure 7. (**a**–**c**) AC-HAADF-STEM images showing the Fe-Co diatomic sites (red rectangles). (**d**) The EELS and intensity profile of Fe–Co diatomic site in the "a" area. (**e**) HAADF-STEM image and corresponding element mappings of T-FeCo-N-C [105].

5.1.2. X-ray Absorption Spectroscopy (XAS)

X-ray absorption spectroscopy (XAS) is an essential technology for exploring the atomic and electronic structures of DACs, encompassing key structural parameters such as coordination distance, coordination type, coordination number, atomic disorder, and metal oxidation state [106]. Synchrotron X-ray absorption fine structure (XAFS) spectroscopy, in particular, stands as an indispensable method for characterizing DACs, owing to its distinct advantages: (1) element selectivity, enabling targeted analysis of the two metal centers in DACs; (2) high sensitivity to local atomic environments, critical for resolving the intimate interactions between the two adjacent metal atoms; and (3) independence from long-range order, making it applicable to amorphous or low-crystallinity catalyst supports [107,108]. XAFS is divided into two regions: X-ray absorption near-edge structure (XANES), which operates within the photon energy range of 30 to 50 eV above the absorption edge, and extended X-ray absorption fine structure (EXAFS), covering the range of 30 to 1000 eV beyond the absorption edge [109]. For DACs, XANES spectroscopy provides valuable electronic structure information, including the oxidation states of metal atoms, electronic interactions between dual metals, and the metal-support electronic interactions. In contrast, EXAFS offers detailed geometric and bonding information around each metal center, such as the bond lengths between the metal atoms and their neighboring atoms, including the potential direct metal-metal bond in DACs, and the coordination environments of each metal site. Fourier transform (FT)-EXAFS spectroscopy plays a pivotal role in determining and analyzing the coordination configurations of the dual metal atoms in DACs. Unlike SACs, where metal-metal bonds are absent, DACs may exhibit a direct metal-metal bond, which can be identified in FT-EXAFS spectra through characteristic peaks corresponding to the metal-metal coordination distance. By comparative fitting of experimental FT-EXAFS spectra with theoretical models, researchers can further determine the coordination types (e.g., metal-N, metal-O, or metal-metal) and coordination numbers of atoms in the first and second coordination shells around each metal center, thereby clarifying the spatial arrangement of the dual atoms (e.g., adjacent, separated, or with specific geometric configurations) [110]. More importantly, the wavelet transform-extended X-ray absorption fine structure (WT-EXAFS) method is particularly useful for DAC characterization. It can effectively identify light element coordination (e.g., C, N, O) around each metal center, which is often challenging to distinguish in R-space or K-space due to overlapping atomic shells and similar backscattering effects. For DACs with complex local environments, WT-EXAFS helps differentiate the coordination environments of the two distinct metal atoms, providing insights into their individual roles in catalytic reactions. By integrating experimental insights into the local coordination environments and fitting parameters for the two metal atoms, reasonable structural models can be constructed through density functional theory (DFT) calculations. Moreover, the comparison of theoretically calculated near-edge spectra with experimental XANES data enables precise inference of the spatial atomic structure of the active dual-atom sites and their interactions with adsorbates. This is also

crucial for understanding how the synergy between the two metal atoms modulates catalytic activity.

Li et al. [111] employed a combination of XANES, EXAFS fitting, wavelet-transform analysis, and theoretical XANES simulations to elucidate the local configuration of Fe–W dual-atom sites in Fe,W-N-C. The Fe K-edge XANES spectrum exhibited an absorption edge located between those of FeO and Fe_2O_3, suggesting an average Fe oxidation state between +2 and +3 (Figure 8a). Notably, the Fe K-edge absorption of Fe,W-N-C shifted to lower energy relative to that of the Fe-N-C counterpart, indicating that the neighboring W site effectively modulates the electronic structure of the Fe center. In the Fourier transformed k^3-weighted Fe K-edge EXAFS spectrum, a prominent peak at approximately 1.5 Å was assigned to first-shell Fe–N coordination, whereas the absence of the characteristic Fe–Fe contribution at 2.2 Å confirmed the atomic dispersion of Fe species (Figure 8b). WT-EXAFS analysis further revealed a pronounced Fe–N scattering contribution centered at k ~4.7 $Å^{-1}$ without detectable metallic Fe–Fe features (Figure 8c). Similar XAFS analyses at the W L_3-edge demonstrated the atomically dispersed nature of the W species (Figure 8d–f). Quantitative EXAFS fitting showed that both Fe and W centers adopt fourfold N coordination, with Fe–N and W–N bond lengths of 1.90 Å and 2.09 Å, respectively (Figure 8b,e). Moreover, the weak features above 2.0 Å in the FT-EXAFS spectra, together with the WT-EXAFS intensity maxima at 5–7 $Å^{-1}$, suggested a non-negligible long-range interaction between the Fe and W centers (Figure 8b–f). Although the relatively long Fe–W distance precluded accurate fitting of a direct Fe–W scattering path, incorporation of the outer coordination shells yielded simulated EXAFS spectra that agreed well with the experimental spectra, further supporting the proposed Fe–N_4/W–N_4 diatomic configuration (Figure 8g). Importantly, theoretical Fe K-edge and W L_3-edge XANES spectra calculated using the Finite Difference Method for Near Edge Structure code exhibited good agreement with the corresponding experimental spectra in both spectral shape and characteristic peak positions, providing further validation of the proposed Fe–N_4/W–N_4 structural model (Figure 8h,i).

5.1.3. Other Characterization Techniques

Ambient-pressure X-ray photoelectron spectroscopy (AP-XPS) and near-ambient-pressure X-ray photoelectron spectroscopy (NAP-XPS) are representative *in situ* XPS techniques, which are characterized by their ability to operate under near-reaction or actual reaction conditions (e.g., atmospheric pressure, specific gas atmosphere, and reaction temperature), rather than in an ultra-high vacuum environment [112,113]. These tools can track the electronic interactions of bimetallic sites in real time during catalytic reactions and exhibit high sensitivity to the possible aggregation of metal dual-atom sites, which can be evaluated by the shift of characteristic peak binding energy. In addition, AP-XPS/NAP-XPS can also monitor the surface chemical states and structural evolution of DACs in real time, revealing the dynamic mechanism of the reconstruction process. Beyond the direct visualization of dual-atom distribution via AC-HAADF-STEM and the characterization of their local coordination environments using XAS spectra, XPS is widely employed to analyze the elemental composition and surface electronic states of DACs. This method can provide key electronic structure information such as the oxidation state, charge transfer, and bonding environment of the dual-atom sites, which serves as an important supplement and verification for other spectroscopic results [114]. Furthermore, for DACs containing specific elements, Mössbauer spectroscopy, due to its high-resolution capability for Fe isotopes, can precisely distinguish the local electronic structure and coordination symmetry of the Fe species of Fe-based DACs by analyzing the hyperfine interaction parameters, including isomer shift, quadrupole splitting, and magnetic hyperfine field [105]. Zhao et al. [115] conducted Mössbauer spectroscopy analysis on the conjugated bridged porphyrin iron dimer (FePc = FePc), accurately identifying the active site as OH-$Fe^{3+}N_4$ (S = 5/2), and differentiating the various iron species present in the monomer, dimer, and polymer states. At the molecular structure and reaction mechanism levels, Fourier transform infrared (FTIR) spectroscopy and Raman spectroscopy are commonly used to identify surface functional groups, monitor the interactions between adsorbed molecules and support or active sites, and thereby infer the reaction pathways. By using appropriate probe molecules, FTIR spectroscopy can identify the changes in vibration frequencies of certain bonds and characterize the relative proportion of metal sites or NPs. For instance, by using a CO probe, the types, oxidation states, and relative distributions of bimetallic sites can be distinguished through changes in characteristic vibration frequencies of the FTIR spectra. Nuclear magnetic resonance (NMR) spectroscopy, by detecting changes in the spin environment of atomic nuclei, can obtain information about the bonding characteristics of ligands around the metal center, the adsorption configuration of intermediates, and the species transformation pathways, thereby elucidating the mechanism of active sites at the molecular level. *In Situ* diffuse reflectance infrared Fourier transform spectroscopy (DRIFTS) further expands the dynamic characterization capabilities of infrared technology, allowing for real-time tracking of the vibration signals of surface functional groups under actual reaction atmospheres and temperatures, and directly reflecting the entire process of adsorption, activation, formation and decay of intermediates, and product desorption of reactants at bimetallic sites. At the

 https://doi.org/10.53941/ges.2026.100027

molecular level, it provides direct experimental evidence for revealing the cooperative mechanism and reaction network of bimetallic species. Additionally, electron paramagnetic resonance (EPR) spectroscopy focuses on detecting unpaired electrons in the system and is suitable for elucidating the generation and evolution of active species (e.g., free radicals, defects, or paramagnetic metal centers) in photocatalytic processes, thereby providing important evidence for revealing reaction mechanisms and the rational design of efficient photocatalysts.

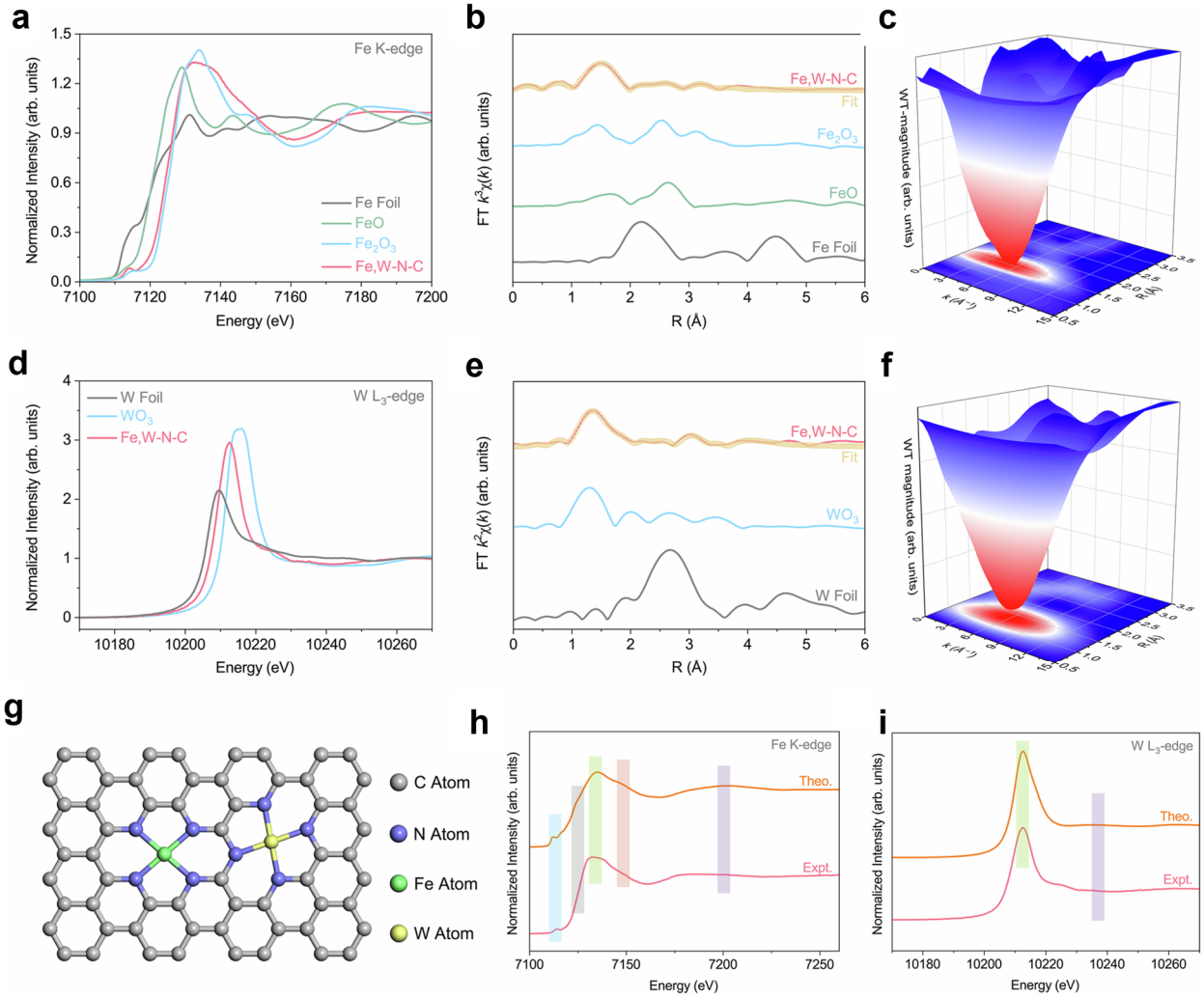


Figure 8. (**a**) Normalized Fe K-edge XANES spectra of Fe foil, FeO, Fe_2O_3, and Fe,W-N-C catalyst. (**b**) Fourier transform k^3-weighted Fe K-edge EXAFS spectra at R space and FT-EXAFS fitting curves of Fe,W-N-C. (**c**) 3D contour wavelet transformed Fe K-edge EXAFS map of the Fe,W-N-C catalyst. (**d**) Normalized W L_3-edge XANES spectra of W foil, WO_3, and Fe,W-N-C. (**e**) k^2-weighted W L_3-edge FT-EXAFS spectra and FT-EXAFS fitting curves of Fe,W-N-C. (**f**) 3D contour wavelet transformed W L_3-edge EXAFS map of the Fe,W-N-C catalyst. (**g**) The atomic structure model of the Fe,W-N-C catalyst. (**h**) Comparison between the experimental Fe K-edge XANES spectrum of Fe,W-N-C and the theoretical spectrum calculated for the atomic structure in (**g**). (**i**) Comparison between the experimental W L_3-edge XANES spectrum of Fe,W-N-C and the theoretical spectrum calculated for the atomic structure in (**g**) [111].

5.1.4. Operando/*In Situ* Spectroscopy Techniques

Despite the significant advances of conventional ex situ XAS techniques in resolving the static geometric and electronic structures of DACs, they inherently fail to capture the dynamic evolution of active sites under realistic reaction environments. To address this limitation, *in situ* and operando spectroscopic techniques have emerged as indispensable tools for probing catalytic processes in real time. In particular, operando XAFS enables direct monitoring of the coordination environment, oxidation states, and electronic structures of dual-atom sites under working conditions, such as light irradiation, CO_2 atmosphere, and aqueous environments. This capability is especially crucial for DACs, which are often thermodynamically metastable and susceptible to dynamic restructuring during catalysis. For example, Wu et al. [59] reported a tri-site catalytic system consisting of a Ni single atom and adjacent Mn_2 dual-atom sites anchored on NH_2-MIL-125(Ti) for the selective photoreduction of CO_2 to propane (C_3H_8). By employing operando XAFS in combination with complementary *in situ* spectroscopies, the authors directly revealed the dynamic electronic evolution and charge transfer

behavior of the Ni_1/Mn_2 sites. Under the Ar atmosphere, the Mn and Ni K-edge XANES spectra exhibit shifts toward lower energy upon light irradiation, indicating electron accumulation at both metal centers. Upon introduction of CO_2, the absorption edges shift positively, suggesting that the accumulated electrons are subsequently transferred to adsorbed CO_2 molecules, thereby initiating its activation and reduction. These observations provide direct evidence that the dual-atom sites function as dynamic electron reservoirs and relay centers during the catalytic process, rather than static active sites.

Beyond single-technique analysis, operando XAFS can be further integrated with complementary spectroscopic methods, such as *in situ* DRIFTS and Raman spectroscopy, to simultaneously correlate active-site evolution with surface reaction intermediates. Such multi-modal operando approaches enable a more comprehensive understanding of catalytic mechanisms by bridging electronic structure dynamics with reaction pathways. A representative example is provided by Shang and co-workers [116], who constructed a 2D/2D $FeSe_2$/protonated carbon nitride ($FeSe_2$/PCN) heterostructure and employed multi-scale *in situ* spectroscopies to visualize interfacial charge transfer during CO_2 photoreduction. By combining operando XAFS with *in situ* XPS, soft X-ray absorption spectroscopy (sXAS), and femtosecond transient absorption spectroscopy (fs-TA), Shang et al. explicitly tracked the charge migration across the heterointerface. The results reveal that photogenerated electrons transfer from PCN to $FeSe_2$ under illumination, as evidenced by the reduction of Fe and Se species and the modulation of absorption features, while fs-TA confirms accelerated carrier transfer kinetics and suppressed recombination. Operando XAFS further shows that Fe sites undergo reversible valence changes, reflecting sequential electron accumulation and transfer to CO_2 during the reaction. Together with operando DRIFTS and DFT calculations, these findings identify *COOH as the key intermediate and demonstrate that $FeSe_2$ lowers the formation energy barrier, thereby accelerating CO production. Overall, the integration of operando spectroscopic techniques provides a powerful framework for establishing structure–activity relationships of DACs under realistic working conditions, enabling deeper insights into dynamic active-site evolution and catalytic mechanisms.

5.1.5. Theoretical Modeling and Machine Learning-Aided Screening

The discovery and rational design of DACs have long relied on conventional trial-and-error approaches and density functional theory (DFT) simulations. However, the exponential growth of the structural space of DACs, owing to the combinatorial explosion of possible metal types, coordination environments, and support materials, has made exhaustive experimental and computational exploration impractical. In response to this challenge, the field is rapidly transitioning toward a systematic study of "computation-first" design, in which theoretical modeling and machine learning (ML) play increasingly pivotal roles in accelerating the identification and optimization of high-performance DACs. DFT calculations are an indispensable theoretical tool for deeply elucidating the microscopic mechanisms of photocatalytic reactions over DACs. At the atomic and electronic scale, DFT can precisely reveal the unique electronic structure and synergistic mechanisms of the two metal centers, assess the thermodynamic feasibility of reaction pathways, determine the kinetic energy barriers of elementary steps, and provide a foundation for constructing reliable structural models of DACs [117,118]. By analyzing parameters such as charge density distribution, d-band center shifts, and bond orders, DFT offers a systematic approach to understanding and predicting the structure-activity relationships linking the orbital configuration, electronic synergy, and catalytic activity of diatomic sites. This enables the quantitative elucidation of how dual metal sites, through electronic complementarity and spatial cooperation, regulate the adsorption-desorption behavior of important intermediates, thereby optimizing the reaction pathway. When combined with experimentally inferred or detected reaction intermediates, DFT can simulate the complete catalytic reaction pathway, calculate the energy barrier for each elementary step, identify the rate-determining step and key intermediates, and reveal the essential mechanism for the high selectivity toward specific products from an energy perspective. Furthermore, research from the perspective of support effects reveals that defects (e.g., N vacancies) or heteroatom doping (e.g., N or O atoms) on the support surface can significantly modulate the electronic structure of diatomic active sites by altering the electron distribution and coordination environment at the metal-support interface. For instance, N-doped carbon supports can enhance charge delocalization on the dual-metal atoms constituting the active sites, optimizing the adsorption strength of the *COOH intermediate in CO_2 reduction, thereby improving catalytic selectivity and conversion efficiency. By integrating the synergy between the diatomic configuration and the support microenvironment, DFT simulations provide multi-scale theoretical support, ranging from atomic structure to reaction mechanism, for the design of active sites in catalytic systems.

Despite the accuracy and mechanistic depth of DFT, its high computational cost renders it impractical for exhaustively screening the vast combinatorial space of DACs, which can easily exceed thousands or even tens of thousands of candidate configurations due to the combinatorial explosion of possible metal types, coordination environments, and support materials. In

 https://doi.org/10.53941/ges.2026.100027

response, ML has emerged as a complementary approach to bridge the gap between accuracy and throughput. ML methods, once trained on DFT-generated datasets, can predict catalytic properties such as adsorption energies, limiting potentials, and selectivity at a fraction of the computational cost, enabling rapid virtual screening across large candidate libraries. More importantly, the integration of DFT and ML offers powerful capabilities for performance prediction and materials design by introducing physically meaningful descriptors, such as the d-band center and Bader charge, to construct predictive models. A central challenge in ML-driven catalyst design lies in selecting appropriate descriptors that effectively encode the complex interplay of geometric, electronic, and environmental factors governing DAC performance. The d-band center (ε_d), originally developed within d-band theory for transition metal surfaces, has emerged as a powerful and widely used electronic descriptor in both DFT and ML studies of DACs. By capturing the energy position of the metal *d* states relative to the Fermi level, the d-band center serves as a quantitative proxy for the adsorption strength of key intermediates: a lower ε_d generally corresponds to weaker binding, and vice versa. For DACs, the situation is more complex due to the presence of two interacting metal centers, but recent studies have shown that appropriately defined d-band descriptors can effectively capture the cooperative effects of dual metal sites. Beyond the d-band center, other physically meaningful descriptors have proven valuable, including electronegativity, atomic radii, coordination numbers, bond lengths, and Bader charges. In addition to these predefined "handcrafted" descriptors, modern ML approaches increasingly leverage automatic feature learning techniques, such as graph neural networks operating on atomic structures, to extract high-dimensional representations directly from the catalyst geometry, bypassing the need for explicit descriptor engineering. The synergy between physically grounded descriptors and data-driven feature learning represents a promising direction for enhancing both the accuracy and interpretability of ML models in DAC discovery.

A representative paradigm of ML-accelerated DAC discovery follows the "3S" workflow: setting out data, selecting models, and screening catalysts [119]. In the first stage, a high-quality dataset is constructed through systematic DFT calculations on a representative subset of DAC candidates, with each candidate characterized by a set of descriptors that encode its essential physical and chemical features. In the second stage, various ML algorithms, ranging from conventional models such as random forest (RF), support vector machines (SVM), and gradient boosting regression (GBR) to advanced architectures like feedforward neural networks (FNNs), are trained and validated to map the descriptor space to target catalytic properties [120]. Model performance is typically assessed using metrics such as the coefficient of determination (R^2) and root mean square error (RMSE). In the third stage, the trained ML model is deployed to predict the catalytic performance of the remaining candidate space, rapidly identifying promising DACs for subsequent experimental synthesis and validation. This workflow has been successfully implemented in several recent studies.

A typical example is the integration of DFT and ML for the transition-metal diatomic-loaded graphitic carbon nitride (TM_1TM_2@g-C_3N_4) system. Bian et al. [121] first performed systematic DFT calculations to accurately obtain the adsorption energies of intermediates on 276 candidate catalyst surfaces. From these, they calculated the limiting potentials for CO and HCOOH generation, constructing a high-quality dataset. This dataset was then used to train an optimized FNN ML model, which accurately learned the complex mapping relationship between diatomic features and catalytic performance, enabling high-throughput rapid prediction of numerous possible combinations (Figure 9). Based on the ML predictions, several high-performance catalyst combinations were identified. RuHf@g-C_3N_4 and VV@g-C_3N_4 were selective toward CO, while MoMo@g-C_3N_4 and CrMo@g-C_3N_4 favored HCOOH production. These selected combinations were then comprehensively validated through further in-depth DFT calculations, which confirmed their electronic structure, visible-light response, and thermodynamic stability. Analyses of the work function, band structure, density of states, and optical properties revealed that the diatomic loading significantly optimizes the electronic structure and optical absorption properties of the catalysts, providing a strong guarantee for efficient PCO_2RR. Finally, the key synergistic mechanism for CO_2 activation at the dual-atom sites was elucidated through charge density difference analysis, Crystal Orbital Hamilton Population (COHP), and free energy surface calculations, further providing a reliable theoretical foundation for experimental synthesis. The research demonstrated that the d-electron count and electronegativity of bimetallic sites determined selectivity by tuning intermediate adsorption. With optimized *COOH adsorption, VV and RuHf sites led to CO production; conversely, with stabilized *HCOO adsorption, MoMo and CrMo sites resulted in selective HCOOH formation. Similarly, an interpretable ML framework based on AdaBoost Regressor was developed to screen 299 transition metal (TM)-based dual-atom photocatalysts anchored on gC_6N_6 for CO_2 reduction. A DFT dataset comprising 40 representative configurations randomly selected from all 299 combinations was used for training, with each candidate described by structure–property (Magpie) and structure-sensitive (Coulomb matrix eigenvalues) featurization. The AdaBoost regressor achieved excellent predictive performance for the potential determining step (PDS), with an R^2 of 0.95

and an RMSE of 0.06 eV. Feature importance analysis identified the mean electronegativity of the anchored metal atoms as the most critical descriptor governing photocatalytic activity. Screening of the full 299 candidates highlighted ScTi/gC_6N_6 and RhMo/gC_6N_6 as the most promising photocatalysts. To further validate the ML predictions, subsequent DFT calculations using the HSE06 hybrid functional were performed on these top candidates. The results confirmed that ScTi/gC_6N_6 and RhMo/gC_6N_6 exhibit suitable band edge positions straddling the redox potentials of CO_2 reduction, strong visible-light absorption due to reduced band gaps (2.02 eV and 2.41 eV, respectively, compared to 3.13 eV for pristine gC_6N_6), and favorable thermodynamic stability with negative formation energies. The heteronuclear diatomic configuration of ScTi and RhMo/gC_6N_6 is associated with its promising photocatalytic performance. This interpretable ML strategy, combined with rigorous DFT validation, enables accurate and rapid prediction of photocatalytic activity, substantially accelerating the discovery of efficient DACs for CO_2 conversion [122].

The integration of DFT and ML is not merely a matter of accelerating screening; it also offers new opportunities for uncovering fundamental catalytic principles. By combining symbolic regression with DFT data, it becomes possible to derive closed-form, interpretable expressions that relate catalytic activity to underlying physicochemical descriptors, thereby distilling complex structure-activity relationships into generalizable design rules. Furthermore, the synergy between DFT calculations and ML models enables a closed-loop optimization paradigm: ML predictions guide experimental synthesis and characterization, and the newly generated experimental data can in turn be fed back into the ML model to refine its predictions, creating an iterative learning cycle that progressively enhances both computational accuracy and experimental efficiency. Looking forward, the development of open-access DAC databases, the application of transfer learning to leverage data from related catalytic systems, and the integration of automated high-throughput experimentation with ML-driven virtual screening are expected to further accelerate the rational design of DACs.

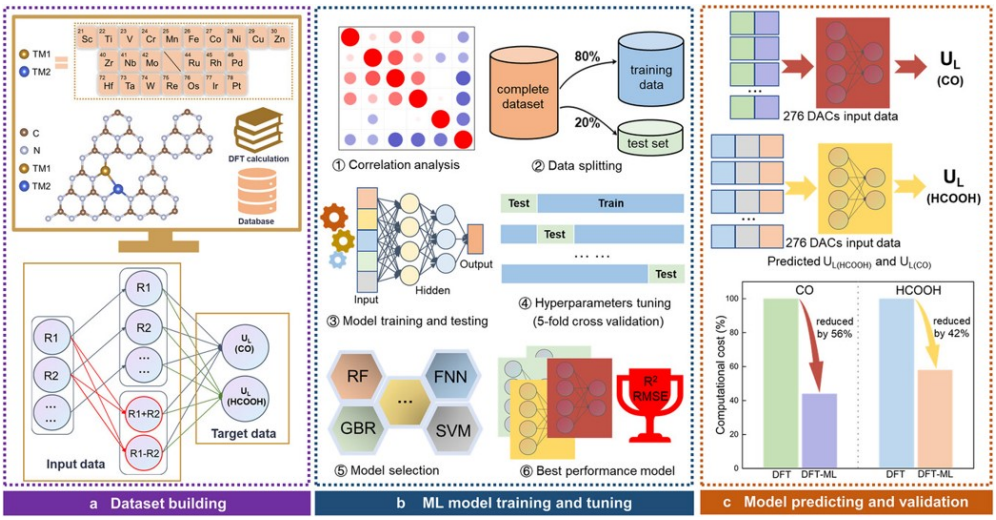


Figure 9. The overall schematic diagram of the DFT-ML screening of DACs for efficient CO_2 reduction. (**a**) Dataset building, (**b**) ML model training and tuning, (**c**) Model predicting and validation. Reprinted with permission from Ref. [121]. Copyright 2025, Wiley-VCH GmbH.

5.2. Performance Evaluation of Photocatalytic CO_2 Reduction Reaction

The performance characterization of DACs in the PCO$_2$RR aims to systematically evaluate their catalytic activity, product selectivity, and catalyst stability. Photocatalytic activity is quantitatively assessed by the product formation rate. Gaseous products (e.g., H_2, CO, CH_4, C_2H_4, etc.) are typically analyzed by gas chromatography equipped with a thermal conductivity detector (GC-TCD) or a flame ionization detector (GC-FID), while liquid products (e.g., HCOOH, CH_3OH) require qualitative and quantitative analysis by high-performance liquid chromatography (HPLC). For instance, GC-FID (flame ionization detector) is used to detect CO and hydrocarbons such as CH_4 and C_2H_4; GC-TCD (thermal conductivity detector) is used to detect H_2, O_2 and N_2; HPLC is used to detect liquid products such as HCOOH and CH_3OH. Product selectivity can be quantified by the molar fraction of a specific product (product distribution) or its electron selectivity (calculated based on the number of transferred electrons). The stability of DACs is primarily evaluated through cyclic experiments and long-term reaction tests, with the retention rate of product formation over multiple cycles commonly used as a quantitative indicator. Performance stability is closely related to the structural integrity of DACs because changes in atomic coordination, metal dispersion, or

support morphology can directly affect catalytic activity. Therefore, comparative characterization of fine structures before and after the reaction using advanced characterization techniques is essential for understanding structural changes and potential degradation pathways. In addition, DACs may be susceptible to photo-corrosion of the semiconductor support or metal leaching from active sites, especially under prolonged or high-intensity illumination. These phenomena can limit long-term operational stability and affect reproducibility. Furthermore, laboratory-scale tests typically employ monochromatic or high-intensity Xe lamps, while performance under real sunlight conditions may differ due to variations in photon flux, spectral distribution, and ambient temperature, highlighting the importance of outdoor or simulated solar-light experiments. Finally, considerations of scalability are crucial for practical applications because increasing catalyst mass or reactor volume can alter light penetration, photon utilization, and mass transport, which may not be fully captured in small-scale laboratory experiments.

In addition to product formation rates, selectivity, and stability, the intrinsic efficiency of photocatalysts can be evaluated by the apparent quantum yield (AQY) or apparent quantum efficiency (AQE), which quantitatively measure the fraction of incident photons converted into chemical products. For DACs, overall activity is often significantly enhanced due to synergistic electron redistribution and cooperation between metal sites; however, the AQY/AQE may not always exceed that of leading SACs. This is partly because DACs generally involve higher metal loading, which can lead to additional light scattering, thus reducing photon utilization efficiency. Moreover, a non-monotonic relationship exists between metal loading and AQY: too low a loading gives insufficient synergistic sites, while excessive loading could dilute the photon flux per active site, meaning that each site receives fewer photogenerated electrons. Furthermore, any thermocatalytic activity from metal sites should be subtracted when calculating the net photo-driven AQY, a step sometimes overlooked in DAC studies. The AQY/AQE also depends on the wavelength and intensity of incident light, the bandwidth of the incident light, reactor geometry, and optical path; therefore, direct cross-comparison of reported AQY values requires caution. It is strongly recommended to report wavelength-specific AQY together with photon flux (mW cm^{-2} or μmol photons s^{-1}), catalyst mass, and the spectral overlap between the light source and the absorption of the semiconductor. In addition, AQY should be distinguished by product: $AQY_{(CO)}$ and $AQY_{(CH4)}$ carry different meanings because CH_4 formation requires eight electrons and multiple photons sequentially on the same site. To provide a critical perspective, a benchmarking table summarizing activity, selectivity, AQY/AQE (with specified measurement conditions), stability, and light source for selected DACs and SACs is included (Tables 1 and 2). These considerations highlight that rational DAC design requires careful balancing of electron transfer pathways, light absorption, metal loading, and reaction conditions to achieve both high catalytic activity and high intrinsic photon-to-product conversion efficiency.

Table 1. Photocatalytic CO_2 reduction performance of SACs anchored on different supports.

Photocatalyst	Reaction Medium	Light Source	Products (μmol g^{-1} h^{-1})	Selectivity (%)	AQE	Stability (h)	Ref.
Ag_1@PCN	H_2O	300 W Xe lamp	CO (161.3) CH_4 (10.5)	94.0	2.4% (400 nm)	10	[104]
Cu/TiO_2	CH_3CN/H_2O (v:v = 5:1)	300 W Xe lamp	C_3H_8 (13.8) C_2H_4 (7.6) CO (18.6) CH_4	C_3H_8 and C_2H_4: 50.2	0.48% (385 nm)	15	[123]
Ru/CeO_2	H_2O	300 W Xe lamp	CH_4 (3.71), CO	CH_4: 92	0.514% (450 nm)	20	[124]
Au/CdS	H_2O	300 W Xe lamp (200–800 nm; 600 mW cm^{-2})	CO (32.2) CH_4 (11.3) H_2 (7.96)	62.6	/	/	[125]
Cu/TiO_2/$BiVO_4$	H_2O	300 W Xe lamp	CO (17.33)	100	/	15	[126]
Au_1/ZIS	CH_3CN/H_2O, TEOA, $Ru(bpy)_3Cl_2·6H_2O$	300 W Xe lamp (λ > 420 nm)	CH_4 (275) CO (78) H_2 (251)	CH_4: 77	0.12% (450 nm)	4	[127]
Cu-CCN	H_2O	300 W Xe lamp	CO (3.086)	100	/	/	[128]
Fe SAS/Tr-COF	H_2O, TEOA, CH_3CN	300 W Xe lamp (λ> 420 nm)	CO (980.3)	96.4	3.17% (420 nm)	20	[129]
Ni-SA-x/ZrO_2	H_2O	300 W Xe lamp	CO (11.8) H_2	92.5	0.92% (365 nm) 0.36% (420 nm)	5	[130]
Cu/CN-0.25	H_2O, $NaHCO_3$, H_2SO_4	300 W Xe lamp (AM 1.5)	CO (11.21) CH_3OH (1.75) CH_4 (0.61)	84.3	1.32% (average 353 nm)	9	[131]
2Au-CN	H_2O	300 W Xe lamp (UV–vis)	CO (6.58) CH_4 (1.58)	80.9	/	/	[132]
Ce-MOF- RuII-bpy	H_2O	300 W Xe lamp (400 < λ < 800 nm)	CH_3COOH (113.3), H_2 (6.5)	CH_3COOH: 99.5	0.93% (450 nm)	50	[133]

Table 1. *Cont.*

Photocatalyst	Reaction Medium	Light Source	Products (μmol g^{-1} h^{-1})	Selectivity (%)	AQE	Stability (h)	Ref.
CuSAs/ UiO-66-NH_2	TEOA, H_2O	300 W Xe lamp (cut-off filter of 400 nm)	C_2H_5OH (4.22) CH_3OH (5.33)	CH_3OH: 55.8	/	40	[134]
Pt_1@CN	H_2O	300 W Xe lamp (AM 1.5)	CO (84.8)	100	1.35% at 400 nm	10	[135]
Pt@Def-CN	H_2O	300 W Xe lamp	CH_4 (6.3) CO H_2	CH_4: 99	/	12	[136]
5T-15CN/BVNS	H_2O	300 W Xe lamp (420 nm cut-off filter)	CO (5.18) CH_4	/	/	12	[137]
Fe-g-C_3N_4	H_2O	300 W Xe lamp	CO (0.51)	/	3.8×10^{-5}% (1 g cat, 200 nm ~ 1000 nm)	/	[138]
Cu/WO_3	H_2O,	300 W Xe lamp	CH_3COOH (2.87) HCOOH CO CH_4	CH_3COOH: 67	/	5	[139]

Table 2. Photocatalytic CO_2 reduction performance of DACs anchored on different supports.

Photocatalyst	Reaction Medium	Light Source	Products (μmol g^{-1} h^{-1})	Selectivity (%)	AQE	Stability (h)	Ref.
CoRu-HCNp	H_2O	300 W Xe lamp	CO (27.3) CH_4	91.8 for 3 h	2.8% (385 nm)	10.5	[140]
1.0Ni0.5Au/In_2O_3	H_2O	300 W Xe lamp (320–780 nm)	C_2H_6 (3.58) CH_4 (1.36) CO (0.90)	C_2H_6: 61.3	2.69% (360 nm)	15	[141]
(Ni, Fe)–N–C	H_2O	300W Xe lamp (AM 1.5G)	CO (86.16) CH_4 (135.35) CH_3OH (59.81)	CH_4: 48.1	/	10	[64]
PtRu/g-C_3N_4	H_2O	300 W Xe lamp	CO (2304) CH_4 (849.29) H_2 (727)	59.4	H_2: 10.5% (365 nm) 8.6% (380 nm)	/	[142]
Cu/S-RPCN	H_2O	300 W Xe lamp	CH_3CH_2OH (50.4) CO CH_4	CH_3CH_2OH: 99.5	/	15	[143]
Co_1In_1/CN	H_2O	300 W Xe lamp	CH_4 (18.8) CO (5.1)	CH_4: 78.6	/	4	[144]
Ni-W/CN	TEOA, H_2O	300 W Xe lamp (AM 1.5)	CO (84.9) CH_4 (15.2)	84.8	/	5	[73]
Mn_1Co_1/CN	H_2O	300 W Xe lamp	CO (47)	99	/	5	[145]
Rh_2DAC	H_2O	Xe lamp	CH_4 (14.16) CO (5.16)	CH_4: 73.3	4.90% (420 nm)	24	[146]
E_7-Cu_5Au_1-TiO_2	H_2O	300 W Xe lamp	C_2H_4 (568.8) C_2H_6 (8.5) CH_4 (68.2) CO H_2	/	C_2H_4: 2.60% (350 nm)	>120	[147]
NiCo-TiO_2	Na_2SO_3, H_2O, CsOH	300 W Xe lamp (UV–vis light)	CH_3COOH (22.6) CH_3OH CH_4 CO	CH_3COOH: 71	/	53	[148]
TiO_2/sc-0.1Cl-0.5Ag	H_2O	300 W Xe lamp	C_2H_4 (244) CH_4 CO	C_2H_4: 64.3	0.73% (340 nm) 0.65% (365 nm) 0.32% (380 nm)	10	[149]
CMCI	H_2O	Xe lamp (AM 1.5 G and 420 nm cutoff filter)	C_2H_5OH (1410.9) CH_3OH CH_4 CO	C_2H_5OH: 93.7	8.46% (400 nm) 8.38% (420 nm) 4.81% (500 nm) 2.03% (550 nm) 0.88% (600 nm)	24	[150]
Mil_v/Cu	H_2O	300 W Xe lamp	CO (10.5) CH_4 (1.0) C_2H_4 (8.7)	C_2H_4: 43.1	/	20	[151]

 https://doi.org/10.53941/ges.2026.100027

Table 2. *Cont.*

Photocatalyst	Reaction Medium	Light Source	Products (μmol g^{-1} h^{-1})	Selectivity (%)	AQE	Stability (h)	Ref.
CuCo-THQ	H_2O, CH_3CN, TEOA, $[Ru(bpy)_3]Cl_2·6H_2O$	300 W Xe lamp (λ > 420 nm)	CO (1626)	100	/	10	[94]
LaNi-Phen/COF-5	BIH, CH_3CN, H_2O	300 W Xe lamp	CO (605.8) H_2 (11.7)	98.2	/	15	[152]
CoNi-COF-3	H_2O, CH_3CN, TEOA, $[Ru(bpy)_3]Cl_2·6H_2O$	300W Xe lamp (λ > 420 nm)	CO (2567) H_2	92.2	2.95% (450 nm)	10	[153]
CuNi/PCN	H_2O, 1% TEOA	300 W Xe lamp (λ > 420 nm)	C_2H_4 (254.3) CO (107.5) CH_4 (209.5)	C_2H_4: 45.2	2.21% (420 nm)	8	[154]
Er_1Nd_3/CN	H_2O, 5% TEOA	300 W Xe lamp	C_2H_5OH (1761.4) CH_3OH (987.7)	C_2H_5OH: 64.1	/	5	[155]
InCu/PCN	DMF, H_2O	300 W Xe lamp	C_2H_5OH (28.5) CO CH_4 H_2	92.4	/	32	[156]
$Cu_{4.2}Zr_6O_8$	H_2O	300 W Xe lamp (Full spectrum)	0.5 MPa CO_2 C_2H_5OH (87.8) CH_3OH (1.3) CO (1.3)	99	/	32	[157]

5.3. Characterization Techniques for Photogenerated Charge Properties

An in-depth investigation into the microscopic kinetic processes, such as the separation and transfer of photogenerated charges, provides crucial experimental evidence for revealing the unique synergistic mechanism in DACs. The separation and transfer efficiency of photogenerated charges directly affects the catalytic activity, which is mainly characterized by photoluminescence (PL) spectroscopy, time-resolved photoluminescence (TRPL) spectroscopy, photocurrent response measurements, and electrochemical impedance spectroscopy (EIS) [62,135]. PL spectroscopy reflects the electron-hole recombination through fluorescence intensity, where a lower fluorescence intensity indicates a lower recombination efficiency. TRPL analyzes the charge separation kinetics through fluorescence lifetime. To directly observe the ultrafast initial processes of charge behavior on the femtosecond to picosecond scale, ultrafast spectroscopic techniques such as transient absorption spectroscopy (TAS) are indispensable. It can directly track the complete dynamic trajectory of carriers after photoexcitation with femtosecond to picosecond resolution, capturing processes like hot carrier cooling, initial charge separation, and interfacial transfer [158,159]. In research on DACs, analyzing the kinetic decay components from TAS allows direct quantification of the intrinsic differences between dual-atom and single-atom sites. TAS analysis not only reveals a significantly faster electron injection rate into dual-atom sites, confirming that dual-atom sites act as efficient electron traps to suppress initial recombination, but also verifies the synergistic extension in the lifetime of trapped charge-separated states, which provides direct kinetic evidence that the dual-atom structure more effectively inhibits the secondary electron-hole recombination. In addition, photocurrent response and EIS are used to evaluate the charge transfer efficiency. Higher photocurrent density coupled with lower impedance indicates a stronger capability for charge separation and interfacial transfer. Kelvin probe force microscopy (KPFM) can characterize the variation of work function on the surface of DACs at the nanoscale, directly reflecting the separation of photogenerated charges [160].

6. Applications of Dual-Atom Catalysts Supported on Different Supports in PCO_2RR

In recent years, DACs have attracted extensive attention in the field of photocatalytic CO_2 reduction due to their unique dual-site synergistic effect and tunable electronic structure. Compared with single-atom systems, dual-atom sites can jointly regulate the adsorption and activation behaviors of intermediates through metal-metal interactions and metal-support interactions, thereby providing higher catalytic activity and product selectivity. Importantly, the performance of DACs depends not only on the metal sites themselves, but also on the precise regulation of the anchored support [43,161]. The crystal structure, electronic properties, and surface chemical environment of the support can precisely regulate the spatial configuration, electronic density of states, and charge distribution of dual-atom sites through strong metal-support interactions. Different supports induce significantly different microenvironments of active sites and synergistic mechanisms owing to their unique properties. The structural and electronic properties of supports modulate the dual-atom site structure, electronic states, and catalytic performance of DACs through metal-support interactions, resulting in distinct differences in the reaction pathways and synergistic mechanisms of DACs in PCO_2RR. These tuning effects can decouple the adsorption energies of key intermediates and partially break conventional scaling relations, thereby selectively guiding reaction pathways and

enhancing multi-electron transfer processes. Different supports create distinct microenvironments around the dual-atom sites, leading to variations in synergistic mechanisms and catalytic performance.

Carbon-based materials (e.g., graphene, carbon nanotubes, porous carbon, etc.) provide a stable coordination environment for dual atoms, and facilitate charge transfer and CO_2 adsorption, owing to their high specific surface area, tunable electronic conductivity, and abundant defect structures. Polymeric carbon nitride (C_3N_4), with its two-dimensional layered structure, abundant pyridinic N sites, and suitable band structure, can not only stabilize dual-atom sites through the coordination between N lone-pair electrons and metal atoms, but also promote the transfer of photogenerated electrons from the support to dual-atom active centers via the π-conjugated system, thereby improving carrier separation efficiency and providing abundant synergistic active sites. Metal oxides (e.g., TiO_2, In_2O_3, etc.) and sulfides are rich in surface vacancies, which can further stabilize and anchor dual-atom sites, and regulate charge separation and reaction pathways through strong metal-support interactions. In recent years, various bimetallic combinations have been successfully immobilized on the aforementioned supports and have exhibited catalytic performance superior to that of their corresponding single-atom counterparts in PCO_2RR. They have shown remarkable potential, especially in promoting C–C coupling, enabling the efficient conversion of CO_2 reduction from C_1 products to C_{2+} products. This chapter will systematically review DACs supported on carbon-based materials, carbon nitride, semiconductor oxides, sulfides, metal-organic frameworks (MOFs), and covalent organic frameworks (COFs), as well as their applications in photocatalytic CO_2 reduction, according to the support types. It will further clarify the support modulation effect, through which various supports influence the formation and stability of dual-atom sites via their structural features (e.g., defects, functional groups, porosity) and electronic properties for optimizing the metal d-band center and adjusting the band structure. Moreover, the unique catalytic synergistic mechanisms arising therefrom will be elaborated, including electronic synergy between bimetallic sites, support-mediated charge transfer, and specific stabilization effects on key intermediates, so as to reveal the indispensable and crucial role of supports in enhancing the activity, selectivity, and stability of DACs.

6.1. Carbon-Based Materials-Supported Dual-Atom Catalysts

Carbon-based supports play a pivotal role in DACs by virtue of their high electrical conductivity and excellent light absorption capacity. Heteroatoms (e.g., N, P) on their surface can form stable coordination structures with bimetallic atomic sites, facilitating the separation of photogenerated charges and enhancing the activation of CO_2. In PCO_2RR, carbon-based supported DACs usually exhibit excellent selectivity for C_1 products [162]. Among these, N-doped carbon supports form M–N coordination structures with bimetallic atoms through sites such as pyridinic N and pyrrolic N, which not only stabilize the dual-atom sites but also finely regulate their electronic states [163]. Mo et al. [64] developed a high-temperature pyrolysis and acid etching method to prepare well-defined N-coordinated Ni and Fe dual-single-atoms on the N-doped carbon substance ((Ni, Fe)-N-C) for gas-solid CO_2 photoreduction in the presence of H_2O in a concentrated solar photothermal system with a solar concentrator (Figure 10a). The (Ni, Fe)-N-C exhibited a superior photothermal catalytic CO_2 reduction performance for CO (86.16 μmol g^{-1} h^{-1}), CH_4 (135.35 μmol g^{-1} h^{-1}) and CH_3OH (59.81 μmol g^{-1} h^{-1}), all of which are higher than those of the Fe–N–C catalyst, respectively (Figure 10b–d). The PDOS in Figure 10e indicates that Ni and Fe metallic d-orbitals exhibit more obvious overlap with CO_2 p-orbitals near the Fermi level after absorbing CO_2 on (Ni, Fe)-N-C. The Fermi level and d-band center of the Fe atom are efficiently modulated in non-interacting Ni–Fe dual-atom pair sites in (Ni, Fe)-N-C DSAC, where electronic interaction is induced via electron orbital hybridization. As a new active site in the Ni–N–N–Fe configuration, the additional Ni atom primarily facilitates the dissociation of *COOH and $*HCO_3$ intermediates, optimizing the corresponding energy barriers during the reaction process (Figure 10f). This ultimately gives rise to specific dual reaction pathways for the solar-driven photothermal reduction of CO_2 to the initial product CO.

6.2. Polymeric Carbon Nitride (CN)-Supported Dual-Atom Catalysts

Graphitic carbon nitride (g-C_3N_4) is a typical metal-free polymeric semiconductor photocatalyst. Its advantages include a tunable band structure, a convenient synthesis method, and excellent coordination capability. However, it possesses intrinsic limitations, including insufficient active sites on the surface of the catalyst and rapid charge recombination. The polymeric carbon nitride (CN) with abundant lone-pair N atoms enables the formation of monodispersed metal-N (M–N) coordination motifs with strong metal-support interactions, which effectively promote charge separation and transfer, thereby enhancing the catalytic performance [164,165]. Consequently, g-C_3N_4 is considered a highly promising support material for constructing DACs.

 https://doi.org/10.53941/ges.2026.100027

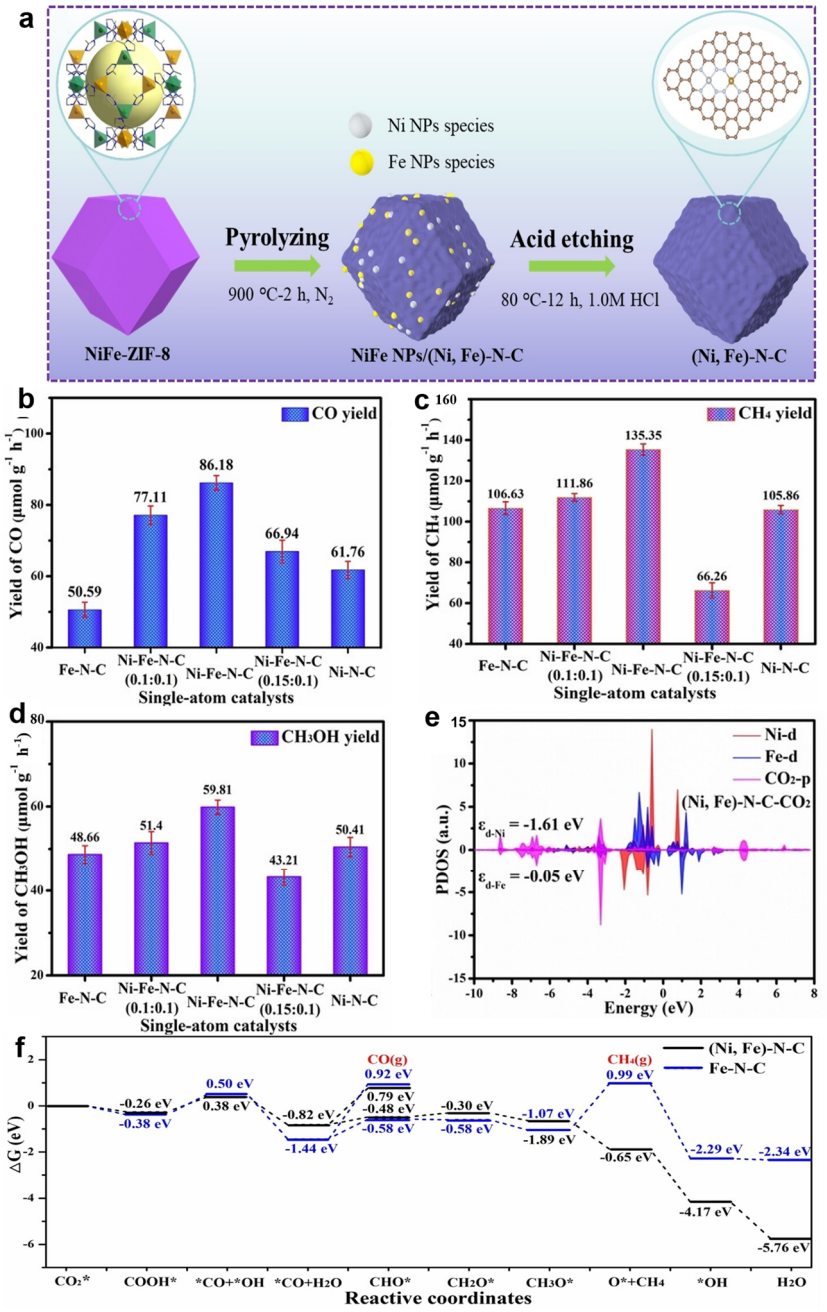


Figure 10. (**a**) Schematic illustration of (Ni, Fe)-N-C DSAC with adjacent Ni–N_4 and Fe–N_4 sites. (**b**–**d**) CO, CH_4 and CH_3OH yields from the CO_2 reduction with H_2O vapor over different SACs under simulated solar irradiation. (**e**) PDOS of before and after CO_2-adsorbed on (Ni, Fe)-N-C. (**f**) Calculated Gibbs free energy diagram for CO_2 reduction pathways to CO/CH_4 on Fe-N-C and (Ni, Fe)-N-C. Reprinted with permission from Ref. [64]. Copyright 2023, Wiley-VCH GmbH.

You et al. [142] reported a method involving the thermal polymerization of the chloroplatinic acid solution to synthesize a catalyst with Pt and Ru single atoms randomly anchored on the g-C_3N_4 surface, yielding partial Pt–Ru dimers and improved catalytic efficiency. The XAS experiments (Figure 11a,b), along with first-principles calculations, confirmed the presence of Pt–Ru bonds in the Pt–Ru dimer complex. The synthesized catalyst exhibited extraordinary photocatalytic activity and stability under full-spectrum irradiation in both the CO_2RR and HER processes. The CO production rate over PtRu/g-C_3N_4 is 2304 μmol g^{-1} h^{-1}, which is 26 times greater than that over PtSAs/g-C_3N_4 (88.45 μmol g^{-1} h^{-1}). Similarly, the CH_4 production rate over PtRu/g-C_3N_4 is 849.29 μmol g^{-1} h^{-1} (Figure 11c). Through in-depth experimentation, including pH-dependent chemical exchange saturation transfer (CEST) imaging nuclear magnetic resonance (NMR) method (Figure 11d,e), and theoretical analyses, it was revealed that the excellent performance was attributed to orbital coupling (mainly d_{xy} and d_{xz}) between the Pt atoms and the neighboring Ru atoms, which decreased the orbital energy levels and weakened the bond strength with intermediates (Figure 11f), resulting in improved CO_2RR and HER performance. Li et al. [143]

elaborately designed a red polymer carbon nitride (RPCN) consisting of S–N and Cu–N_4 dual active sites (Cu/S-RPCN) to address the challenge of limited efficiency of charge separation, sluggish kinetics of C–C coupling, and unfavorable formation of oxygenate intermediates for the solar-driven CO_2 reduction to C_2H_5OH. The Cu/S-RPCN achieved an impressive C_2H_5OH evolution rate of 50.4 μmol g^{-1} h^{-1} with 99.5% selectivity in pure water. Cu and S atoms within the Cu–N–S configuration could serve as trapping centers for electrons and holes, respectively, providing spatial separation for photogenerated charge carriers. The incorporation of S atoms optimizes the adsorption of *CO on Cu atoms and reduces the energy barrier for the formation of the *CO-COH intermediate. The adsorption strength of *$OCHCH_2OH$ intermediate on the Cu atoms via the O–Cu–C configuration influences C_{2+} product selectivity, as the cleavage of the Cu–O/Cu–C bonds dictates whether the pathway leads to C_2H_5OH or C_2H_4. The S–N–Cu structure weakens the Cu–O bond, thereby promoting the production of C_2H_5OH.

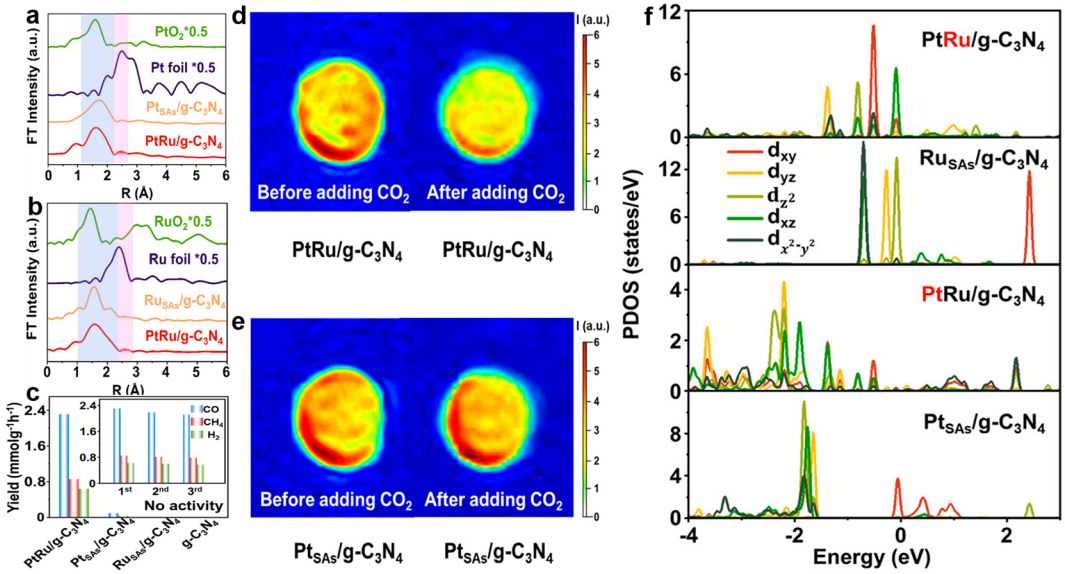


Figure 11. Fourier transform (FT)-EXAFS spectra in R space at the (**a**) Pt L_3-edge and (**b**) Ru K-edge for $Pt_{SAs}/g\text{-}C_3N_4$, PtRu/g-C_3N_4, and $Ru_{SAs}/g\text{-}C_3N_4$, together with PtO_2, Pt foil, RuO_2, and Ru foil as references (**c**) Yield of products formed during the PCO_2RR of different samples, the inset shows the cycling performance of PtRu/g-C_3N_4. (**d**) CEST images of the PtRu/g-C_3N_4 sample before and after adding CO_2 gas. (**e**) CEST images of the $Pt_{SAs}/g\text{-}C_3N_4$ sample before and after adding CO_2 gas. (**f**) The partial density of states of Ru d for $Ru_{SAs}/g\text{-}C_3N_4$ and PtRu/g-C_3N_4, and of Pt d for $Pt_{SAs}/g\text{-}C_3N_4$ and PtRu/g-C_3N_4. Reprinted with permission from Ref. [142]. Copyright 2024, American Chemical Society.

Hu et al. [144] successfully synthesized a Co and In DACA supported on C_3N_4 (Co_1In_1/CN) using an "assembly and pyrolysis" strategy. The structures of the bimetallic single atoms Co–N_4 and In–N_5 were determined through combined characterization using HAADF-STEM, XANES, EXAFS and DFT calculations. By constructing a dual single-atom catalyst featuring Co-N_4 and In-N_5 coordination structures, a synergistic effect between the Co and In atoms was triggered. Differential charge density and Gibbs free energy calculations demonstrated that the Co_1–In_1 dual-site structure possesses a superior electronic structure compared to SACs. This structure optimizes the adsorption energy of the critical *CHO intermediate and effectively reduces the energy barrier of the CO_2 → CH_4 process. Consequently, highly selective and active photocatalytic CO_2 reduction to CH_4 was achieved without using sacrificial agents or photosensitizers. The CH_4 and CO production rates reached 18.8 and 5.1 μmol g^{-1} h^{-1}, respectively. In a separate study, Yan et al. [73] prepared a unique noble-metal-free Ni–W dual-atom catalyst supported on polymeric carbon nitride (Ni-W/CN). This catalyst exhibited a CO production rate of 84.9 μmol g^{-1} h^{-1} with a CO selectivity of 84.8%, which was 10.5 times higher than that of pristine CN. A series of characterizations revealed that in the Ni-W/CN DAC, the W atom formed a robust interaction with CO_2 molecules, activating their anti-bonding π orbitals via electron transfer from its 5d orbital. Concurrently, the Ni site facilitated charge separation by accumulating photogenerated holes through its 3d orbital, thereby synergistically enhancing the overall photocatalytic activity.

The specific morphologies of C_3N_4 (e.g., hollow sphere structure, porous nanorod, etc.) can not only provide a high specific surface area to facilitate the adsorption and activation of CO_2, but also enhance the light-harvesting capability and greatly shorten the charge migration pathway via their unique geometric structures. Inspired by the natural photosynthetic system, Ou et al. [145] synthesized a Co-Mn dual single-atom carbon nitride (CN) photocatalyst, which simultaneously realized the reduction of CO_2 to CO and the oxidation of H_2O. Mn_1Co_1/CN exhibited optimal photocatalytic CO_2

 https://doi.org/10.53941/ges.2026.100027

reduction performance, with a CO evolution rate reaching 47 μmol g^{-1} h^{-1}. The immobilized Co and Mn single atoms could serve as redox sites, significantly boosting the CO evolution rate. Furthermore, this photocatalyst possessed high stability, with the selectivity for CO_2 reduction to CO approaching 100%. Experimental results and DFT calculations demonstrated that the Mn atomic centers on CN facilitated the oxidation of H_2O, while the Co atomic centers promoted the activation of CO_2. Ma et al. [146] first achieved an Rh_2 DAC on loose porous g-C_3N_4 hollow nanospheres with N-vacancies. They applied it to PCO_2RR, overcoming the current limitations of the high electron-hole recombination rate and prolonging the lifetime of the photogenerated carriers. The high specific surface area of the hollow nanosphere facilitated the uniform dispersion and anchoring of Rh_2 diatomic pairs, while the N-vacancies induced a stable 3N/Rh–Rh/2C1N coordination between the support and Rh_2 diatomic pairs. The local charges on the support framework with N vacancies tended to be transferred to the Rh_2 diatomic site through the 3N/Rh–Rh/2C1N bridge, which made the charge-enriched Rh_2 diatomic site the active center of the reaction, enhancing the charge separation efficiency of Rh_2/HCNS-Nv catalyst. Compared with Rh_1 SACs, further DFT calculations confirmed that the Rh_2 DAC could effectively stabilize the rate-limiting CHO^* intermediate, weaken the C–O bond strength in CH_3O^* species, and promote the generation and separation of CH_4, resulting in high CO_2 reduction efficiency and CH_4 electron selectivity of up to 91.65%.

6.3. Semiconductor Oxide-Supported Dual-Atom Catalysts

Semiconductor oxide supports, such as TiO_2, ZnO, In_2O_3, possess well-defined band structures and promote photogenerated charge separation [166]. The O vacancies on their surfaces can form strong interactions with bimetallic sites, effectively regulating CO_2 reduction reaction pathways. Notably, oxide-supported DACs exhibit unique advantages in producing C_{2+} products. As a classic photocatalyst, TiO_2 has good stability and light absorption performance. However, pure TiO_2 suffers from weak CO_2 adsorption and poor product selectivity. Introducing dual-atom sites can significantly enhance its selectivity for C_{2+} products. Xie et al. [147] initially proposed up-bottom ion-cutting architecture to synthesize atomic-level catalysts. By exploiting the vectored etching of Cu from a CuAu alloy (where Au atoms are isolated in the Cu lattice), the CuAu-DAs with subnanometer heteroatomic spacing supported by commercial TiO_2 (CuAu-DAs-TiO_2) were successfully fabricated. Figure 12a illustrates the ion-cutting architecture fabrication of Cu nanoclusters (Cu-NCs) decorated with Au-SAs (CuAu-NCSAs), CuAu-DAs, and Au-SAs/Cu-SAs supported by TiO_2 via adjusting the vectored etching time of the Cu_5Au_1 alloy. Due to the compact heteroatomic spacing (2–3 Å), CuAu-DAs-TiO_2 exhibited superior spatial proximity. Systematic Cu K-edge and Au L-edge XANES and EXAFS analyses, combined with wavelet transform, confirmed the formation of adjacent Cu-Au diatomic sites in E_7-Cu_5Au_1-TiO_2. Both Cu and Au atoms coordinate with lattice O of TiO_2, while a distinct Cu–Au coordination path was observed. The absence of Cu–Cu or Au–Au metallic bonds and the fitting results, which indicate that Cu is adjacent to only one Au atom, collectively demonstrated the successful construction of a Cu-Au diatomic structure (O-Cu-Au-O), originating from the initial alloy rather than from rearrangement during etching. The C_2H_4 production of CuAu-DAs-TiO_2 proceeded at a remarkable rate of 568.8 μmol g^{-1} h^{-1} without any sacrificial agent, which was superior to recently reported works in photoconversion of CO_2 and H_2O into C_2H_4 (Figure 12b), and no apparent catalyst deactivation was observed during the photocatalytic stability test for 120 h (Figure 12c). To elucidate the relationship between C-based intermediate conversion efficiency and different nanostructures, DFT calculations on various TiO_2-supported models were performed (Figure 12d). The results revealed that while *CO formation was spontaneous on all catalysts, its subsequent conversion was rate-determining. Crucially, the CuAu-DAs-TiO_2 model uniquely enabled a low-barrier (0.54 eV) C–C coupling pathway (*CO → *OCCO), a more favorable route compared to the higher-energy protonation pathways on other models (e.g., 1.41 eV for CO→CHO on Cu-SAs-TiO_2). This efficiency stems from the strongest *CO adsorption energy (−1.98 eV) on CuAu-DAs-TiO_2, which ensures high *CO coverage and optimal proximity with a C–C distance of 1.40 Å for dimerization (Figure 12e). In such CuAu-DAs structures, Cu-SAs were mainly responsible for the high-efficiency *CO generation rather than C–C coupling centers, while Au-SAs served as *CO coupling centers to rapidly consume the *CO arising from Cu-SAs according to the PCO_2RR, which synergistically promoted the high efficiency and sustainability of photoconversion of CO_2 into C_2H_4. The synergistic cooperation between adjacent Cu-SAs and Au-SAs reconfigured the surface reactant intermediate adsorption and drastically reduced the critical C–C coupling barrier. The synergistic mechanism in CuAu-DAs-TiO_2 simultaneously enhanced high-efficiency *CO formation and conversion, effectively mitigating CO poisoning and overcoming the activity-stability trade-off in photocatalytic CO_2 reduction to C_2H_4 (Figure 12f).

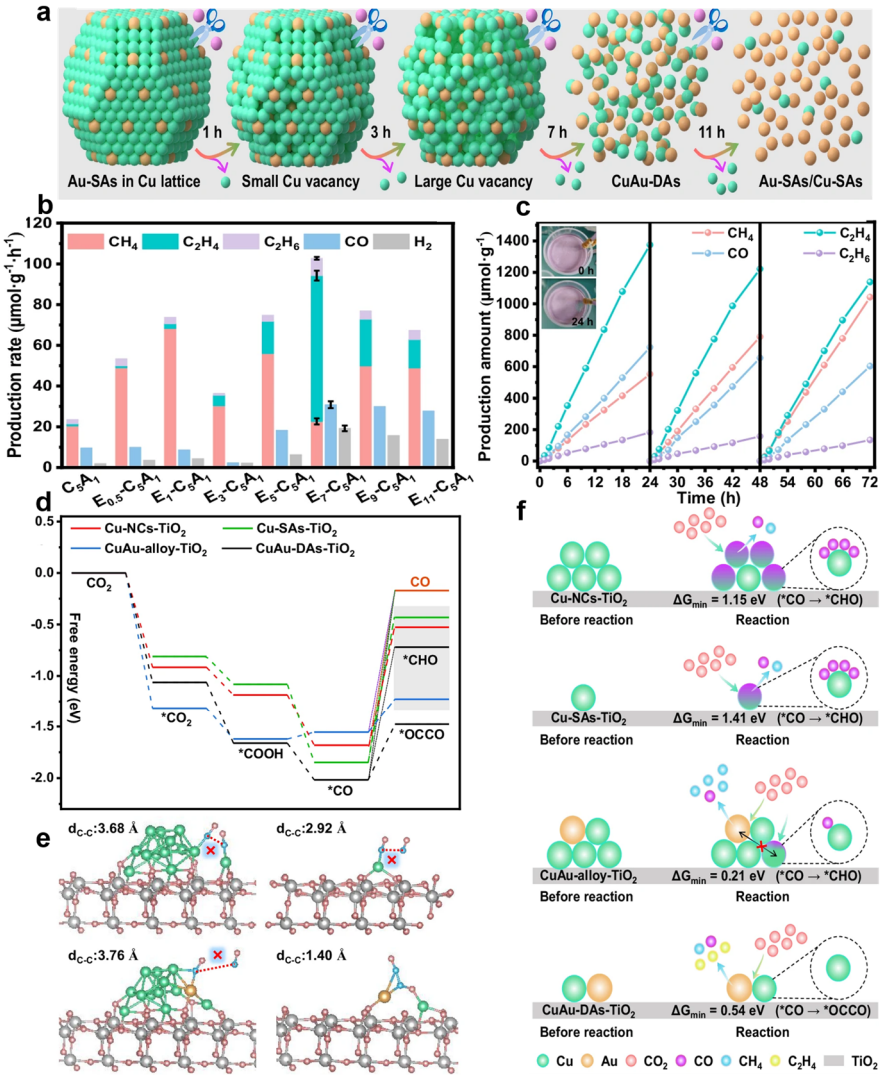


Figure 12. (**a**) Dynamic schematic illustration from isolated Au-SAs in the Cu lattice to CuAu-DAs during the vectored etching process (green sphere: Cu_0; orange sphere: Au_0; purple sphere: Fe^{3+}). (**b**) CH_4, C_2H_4, C_2H_6, CO, and H_2 production rates of the Et-Cu_5Au_1-TiO_2. (**c**) Long-term photocatalytic stability test of E_7-Cu_5Au_1-TiO_2. (**d**) The free energy diagram of CO_2 reduction to CO, *CHO, and *OCCO over different modeled surfaces. The asterisk (*) denotes the adsorption site on the catalyst. (**e**) The most energetically favorable *OCCO adsorption configurations. (**f**) Schematic illustration of the CO poisoning pathway during the PCO2RR on different models [147].

Taking the experimentally reported Cu-doped TiO_2 (Cu-TiO_2) with high C_3H_8 selectivity and well-defined structure as a prototype, Ren et al. [167] conducted a mechanism-guided design of a CO_2 reduction photocatalyst. Mechanistic studies highlighted three key factors for C_3H_8 formation: the formation of dual O vacancies (Vdi-O) for selectivity, C–C coupling for activity, and Vdi-O recovery for durability. More importantly, Vdi-O formation/recovery and C–C coupling are negatively correlated, indicating that an ideal catalyst should strike a balance between O vacancy (VO) formation and C–C coupling. Based on this, the team designed TiO_2 doped with two adjacent copper atoms (Cu–Cu–TiO_2) to enhance the performance of CO_2 photoreduction to C_3H_8. A simple descriptor (Nμ, effective d-electron count) based on intrinsic atomic properties was constructed to reveal the root cause of performance variations across different systems. The study found that dual Cu sites lower the formation energies of the first and second O vacancies, enhancing the formation and regeneration capability of dual O vacancies (Vdi-O). Meanwhile, the synergistic effect of dual sites significantly reduces the energy barriers for *CO-CHO coupling and *CO-COCHO coupling, promoting the sequential formation of C–C bonds and ultimately achieving highly selective C_3H_8 generation. Jia et al. [148] first synthesized a Ti-tannic metal-organic complex containing Ni and Co atoms via a low-temperature hydrothermal method to form an amorphous nanoparticle precursor structure. Subsequently, NiCo-TiO_2 DACs with asymmetrically coupled Ni and Co single-atom sites were successfully prepared by annealing the precursor. The NiCo-TiO_2 DACs

produced acetic acid (CH_3COOH) as the C_2 product, achieving a yield of 22.6 μmol g^{-1} h^{-1} and a high selectivity of 71%. The experimental data and theoretical calculations reveal that the Ni and Co single-atom sites not only significantly lower the energy barrier of electron transfer in photocatalysis, but also efficiently promote the C–C coupling toward CH_3COOH. Moreover, the asymmetric local electric field from dual-atomic sites further generates an asymmetric charge center, which promotes the separation of photocarriers and realizes the multi-electron process to accelerate PCO_2RR. DFT calculations have demonstrated the electronic modulations induced by the surface neighboring local asymmetric Ni and Co dual active single-atom sites, which not only improve the absorption of light excitation with fast electron transfer but also facilitate the C–C coupling via the advantage of lattice structures, resulting in the high selectivity and activity of photocatalytic generation of CH_3COOH. Spatially separated dual-site catalysts also play a crucial role in CO_2 photoreduction. Their core concept lies in precisely anchoring two functionally complementary active centers at distinct locations on the support, effectively decoupling the oxidation and reduction half-reactions through physical spatial separation, thereby significantly suppressing back-reactions and charge recombination [168]. Such catalysts typically rely on long-range electronic coupling mediated by the support or clear functional division of labor to construct tandem catalytic pathways. For example, one site may specialize in generating *CO intermediates, while another site is responsible for their further conversion, thereby separately optimizing the thermodynamics and kinetics of multi-step reactions and ultimately achieving synergistic improvement in activity and selectivity. Du et al. [149] constructed a chlorine (Cl)-bridged Ti–Ag dual-site catalyst to synergistically drive the efficient conversion of CO_2 to C_2H_4. Introducing Cl into the Ti–Ag dual-site spatially separates C–C bond formation from intermediate protonation, making *CO dimerization thermodynamically more favorable than *CO hydrogenation. Incorporating Cl into the TiO_2 lattice modulates the charge distribution on Ti sites and shifts the CO_2 adsorption configuration from a weak monodentate mode to a stronger bidentate binding mode, thereby promoting CO_2 activation and *CO generation for C–C coupling. *In Situ* characterization and DFT calculations reveal that Cl enables the Ti site in the Ti–Cl–Ag configuration to serve as the active center for CO_2 activation and C–C coupling, increasing the concentration of *CO intermediates and lowering the C–C coupling energy barrier. Meanwhile, the Ag site preferentially catalyzes H_2O dissociation, providing active hydrogen for subsequent protonation of *OCCO intermediates, thereby enhancing the overall C_2H_4 generation rate. The optimized Ti–Cl–Ag catalyst achieves a high C_2H_4 yield of 244 μmol g^{-1} h^{-1} with 64.3% selectivity, outperforming the O-bridged Ti–Ag catalyst, which predominantly favors deep hydrogenation of *CO.

In addition, besides TiO_2, DACs supported on other oxides such as CeO_2 and In_2O_3 have also been well applied in PCO_2RR. Wei et al. [141] constructed Ni-Au dual-atom sites (1.0Ni0.5Au/In_2O_3) on the In_2O_3 support via a facile impregnation thermal anchoring method, which was used for the highly selective photocatalytic reduction of CO_2 to C_2H_6 in a sacrificial-agent-free gas-solid system. The C_2H_6 production rate of this catalyst reached 3.58 μmol g^{-1} h^{-1} with an electron selectivity of 79.8% (Figure 13a,b). A series of photoelectrochemical characterizations (especially *in situ* XPS) demonstrated that electrons were transferred from the In_2O_3 support to the Ni-Au dual-atom sites, and strong electronic interactions existed between Ni and Au (Figure 13c–f). Meanwhile, the Ni-Au dual-atom sites significantly enhanced the separation and transfer kinetics of photogenerated electron-hole pairs. The immobilization of Ni–Au dual atoms not only exhibited significantly enhanced light absorption and conversion capabilities but also enabled Ni and Au atoms to assume distinct roles in intermediate adsorption and C–C coupling. Control experiments and *in situ* DRIFTS characterization revealed that the Au sites in the 1Ni0.5Au/In_2O_3 catalyst facilitate the C–C coupling step of C_1 intermediates, while the Ni sites significantly increase the local CO concentration around the active sites; the synergistic effect of both sites thus improves the efficient production of C_2H_6 (Figure 13g). Liu et al. [169] reported Au–Cu dual-atom sites anchored on oxygen-defective Bi_2WO_6 nanosheets for PCO_2RR. The introduction of oxygen vacancies not only stabilizes atomically dispersed Au and Cu species but also modulates their coordination environments. The resulting Au–Cu dual sites exhibit distinct functions, where Cu sites facilitate CO_2 adsorption and activation, while Au sites promote charge accumulation and proton-coupled electron transfer. This synergistic interaction significantly lowers the energy barrier for the key *CO–*CO coupling step (from 1.368 eV on single-metal sites to only 0.363 eV on the Au–Cu dual sites), thereby enabling efficient C–C bond formation. As a result, the catalyst achieves a high selectivity for C_{2+} products (C_3H_6 and C_2H_4) of 65.4% and a total C_{2+} production rate of 54.9 μmol·g^{-1}·h^{-1} under concentrated light irradiation (2.4 W·cm^{-2}). Operando DRIFTS and DFT calculations further confirm that the dual-site configuration stabilizes key intermediates such as *COCO and *COCOCO, steering the reaction pathway toward multi-carbon products.

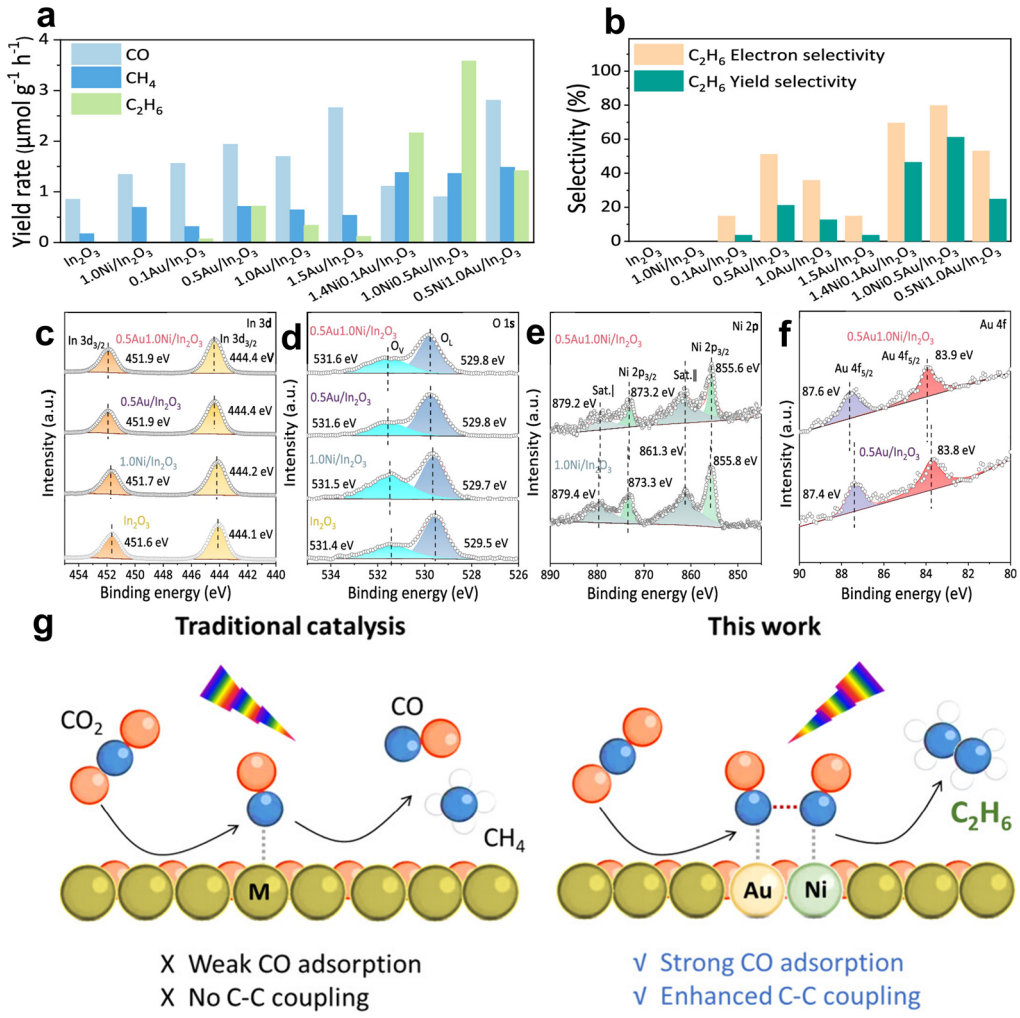


Figure 13. (**a**) Yield rate of products and (**b**) selectivity of products over different catalysts. The X-ray photoelectron spectroscopy (XPS) of (**c**) In 3d, (**d**) O 1s, (**e**) Ni 2P, and (**f**) Au 4f for the pristine In_2O_3 and 1.0Ni0.5Au/In_2O_3. (**g**) Schematic diagram of the efficient photocatalytic reduction of CO_2 to C_2H_6 by Ni-Au diatomic pair site catalyst compared with the traditional photocatalytic CO_2 reduction route. Reprinted with permission from Ref. [141]. Copyright 2026, American Chemical Society.

6.4. Sulfide-Supported Dual-Atom Catalysts

Metal sulfides are ideal supports for anchoring DACs. Sulfides, represented by CdS and $ZnIn_2S_4$, possess narrow band gaps and suitable band positions, endowing them with efficient visible-light harvesting capability and providing sufficient thermodynamic driving force for CO_2 reduction [170,171]. In addition, the abundant S atoms on their surfaces can not only act as electron traps to suppress charge recombination, but also serve as robust anchoring sites to stabilize bimetallic sites by forming strongly covalent M–S coordination bonds with metal atoms, regulate the d-band center of active sites and optimize the adsorption behaviors of key intermediates. Cui et al. [150] reported Cu-In dual sites in a chiral mesostructured copper-doped In_2S_3 (CMCI) for highly selective photocatalytic CO_2 reduction to C_2H_5OH under simulated solar irradiation without any additives. Cu^{2+} substitution for In^{3+} induces compressive strain and lattice distortion in cubic In_2S_3, while the mirror-image circular dichroism (CD) spectra of the antipodal CMCIs confirmed their chirality and handedness. The XAS and EXAFS results indicate that the oxidation state of Cu in L-CMCI is coordinated to approximately 3 S atoms on In_2S_3. The spin polarization of CMCI was investigated by magnetic tip conducting atomic force microscopy (mc-AFM), revealing opposite. spin-selective photoexcited electron transport with spin-up and spin-down states through L- and D-CMCI, respectively. In the case of racemic and non-chiral structures, there is no spin polarization. Upon photoexcitation, spin-flipping of the polarized electrons generates a spin screening effect that suppresses their return to the valence band, thereby prolonging carrier lifetimes and enhancing photocurrent generation. The catalyst achieved a C_2H_5OH yield of 1.4 mmol g^{-1} h^{-1} and a selectivity of 93.7%, over chiral mesostructured copper-doped In_2S_3 photocatalysts. This work demonstrates that the chiral structure of the catalyst can induce electron

spin polarization, promoting the formation and stability of the triplet OCCO (^{3}OCCO) intermediate. Subsequently, the surface Cu-In dual active sites can efficiently convert the ^{3}OCCO intermediates into chemically adsorbed *OCCO and *OCCOH intermediates, thereby facilitating the formation of C_2H_5OH through C–C coupling and inhibiting the generation of C_1 by-products.

Zhang et al. [172] developed an Au/Co dual single-atom (DSA) strategy on CdS nanoparticles to regulate photogenerated charge redistribution for enhanced photocatalytic CO_2 reduction. Atomic-resolution HAADF-STEM and EDX elemental mapping confirmed the atomic dispersion and homogeneous distribution of Au and Co species over CdS (Figure 14a). XANES and EXAFS spectra further revealed their electronic states and local coordination environments (Figure 14b–e). Both Au and Co exhibited higher oxidation states than their metallic counterparts, while the FT-EXAFS spectra showed dominant Au–S and Co–S contributions at approximately 1.8 Å without detectable Au–Au or Co–Co scattering. EXAFS fitting suggested coordination numbers of approximately 2 and 4 for Au–S and Co–S, respectively. WT-EXAFS analysis further displayed characteristic Au–S and Co–S intensity maxima at approximately 8.5 $Å^{-1}$ and 5 $Å^{-1}$, respectively, confirming the single-atom nature of the Au and Co species. The optimized CAC2 catalyst exhibited CO and CH_4 yields of 64.1 and 7.7 μmol g^{-1}, respectively, corresponding to approximately 2800% and 700% enhancements relative to pristine CdS (Figure 14f). The origin of this enhanced activity was elucidated by *in situ* XPS and theoretical calculations. Upon illumination, Au and Co single atoms in the monometallic systems accumulated photogenerated electrons, whereas CAC2 exhibited opposite shifts in the Au 4f and Co 2p binding energies, indicating electron depletion around Au and electron accumulation around Co. Charge-density-difference calculations reproduced this asymmetric electron distribution (Figure 14g), while electrostatic potential analysis showed that the potential energy of CdS lies between those of Au and Co, providing a driving force for the unusual electron-transfer pathway from Au through CdS to Co (Figure 14h,i). Consequently, electron-rich Co and electron-deficient Au regions generate an atomic-scale polarization field that promotes charge separation and CO_2 activation. *In Situ* DRIFTS further identified *COOH, *CHO, *CH_2O, *CH_3O, and *CH_3 intermediates during photocatalysis, supporting a multistep CO_2-to-CH_4 reduction pathway. DFT calculations further showed that the energy barrier for the rate-limiting CO_2 chemisorption step decreased markedly from 1.25 eV on Co single-atom CdS to 0.48 eV on the Au/Co DSA system. These results demonstrate that the Au/Co dual-single-atom configuration induces reversed and spatially asymmetric electron redistribution, thereby facilitating CO_2 adsorption, activation, and subsequent multielectron photoreduction.

6.5. MOF-Supported Dual-Atom Catalysts

Metal-organic frameworks (MOFs) are a class of novel photocatalytic materials featuring highly ordered crystal structures, large specific surface areas, designable metal nodes, and functionalizable organic ligands [173]. They provide a unique platform for investigating photocatalytic reaction mechanisms and constructing highly efficient active sites. In particular, MOFs constructed from flexible metal centers and organic ligands with well-defined structures possess precisely tunable band gaps and band edge positions, as well as uniform and monodispersed active sites, which can serve as an ideal platform for precisely manipulating the selectivity of catalytic products [174]. Different from traditional semiconductors, the metal nodes of MOFs can simultaneously serve as electron channels and reaction sites, while their ligands can not only enhance light absorption and regulate band structures, but also participate in efficient electron-hole separation and intermediate stabilization [175]. More importantly, MOFs allow the construction of isolated, dual-atom and even polymetallic synergistic active sites at the molecular level, thereby providing more possibilities for optimizing the PCO_2RR. Song et al. [151] synthesized O vacancy-rich Mil-125(Ti)-NH_2 (abbreviated as Mil_v) using Mil-125(Ti)-NH_2 (abbreviated as Mil) as the precursor, and then anchored Cu single atoms to prepare the Mil-125(Ti)-NH_2/Cu (abbreviated as Mil_v/Cu) photocatalyst. The low-dose real-space imaging technique was used to resolve the atomic structure of building units in Mil_v/Cu (Figure 15a). The enlarged low-dose HRTEM image of Mil_v/Cu (Figure 15b) reveals the bulk lattice structure viewed from the [001] direction, further confirmed via the corresponding theoretical models. They also identified the arrangement of Cu atoms from the magnified real-space imaging, and intensity profiles extracted from dotted lines (Figure 15c) straightforwardly indicate the identified locations of Cu atoms. The normalized XANES spectra (Figure 15d) and EXAFS spectra (Figure 15e) confirm that the Cu exists in the form of single atoms. Notably, a unique peak at 2.02 Å, ascribed to the Cu–Ti bond, demonstrates the strong binding between Cu and Ti. The WT-EXAFS analysis further confirmed the existence of the Cu–O configuration. Each Cu atom is coordinated to two O atoms in Mil_v/Cu, denoted as Cu–O_2. *In Situ* XPS and ESR showed the photogenerated electron migration behavior of Ti → Cu, while transient absorption spectroscopy indicated that the charges achieved ultrafast separation and redistribution within 3.0 ps (Figure 15f). Compared with Mil, the CO_2 photo-reduction electron consumption of Mil_v/Cu increased by 2.8 times, and the solar-to-chemical energy conversion efficiency reached 0.62%, with a C_2H_4 electron selectivity of up to 78.3% (Figure 15g). The *CO_3^{2-} peaks at 1260, 1360, and 1630 cm^{-1}, as well as the *HCO_3^- peak at 1280 cm^{-1} show the obvious adsorption of

CO_2 on the surface of Mil_v/Cu. The signals at 1468 and 1557 cm^{-1} can be ascribed to *COOH, representing the crucial conversion from CO_2 to CO, further demonstrated by the linear-absorbed *CO peak at 2077 cm^{-1} and bridge-absorbed *CO peak at 1936 cm^{-1} (Figure 15h). DFT further reveals that the Cu–Ti bimetallic sites can induce a strong d-p hybridization of the *CHOCO intermediate, and enable the structural self-regulation under excitation, allowing thermodynamically unfavorable C–C coupling to occur spontaneously. Its behavior is similar to the excited-state structure response of the natural photosynthetic reaction center (Figure 15i,j).

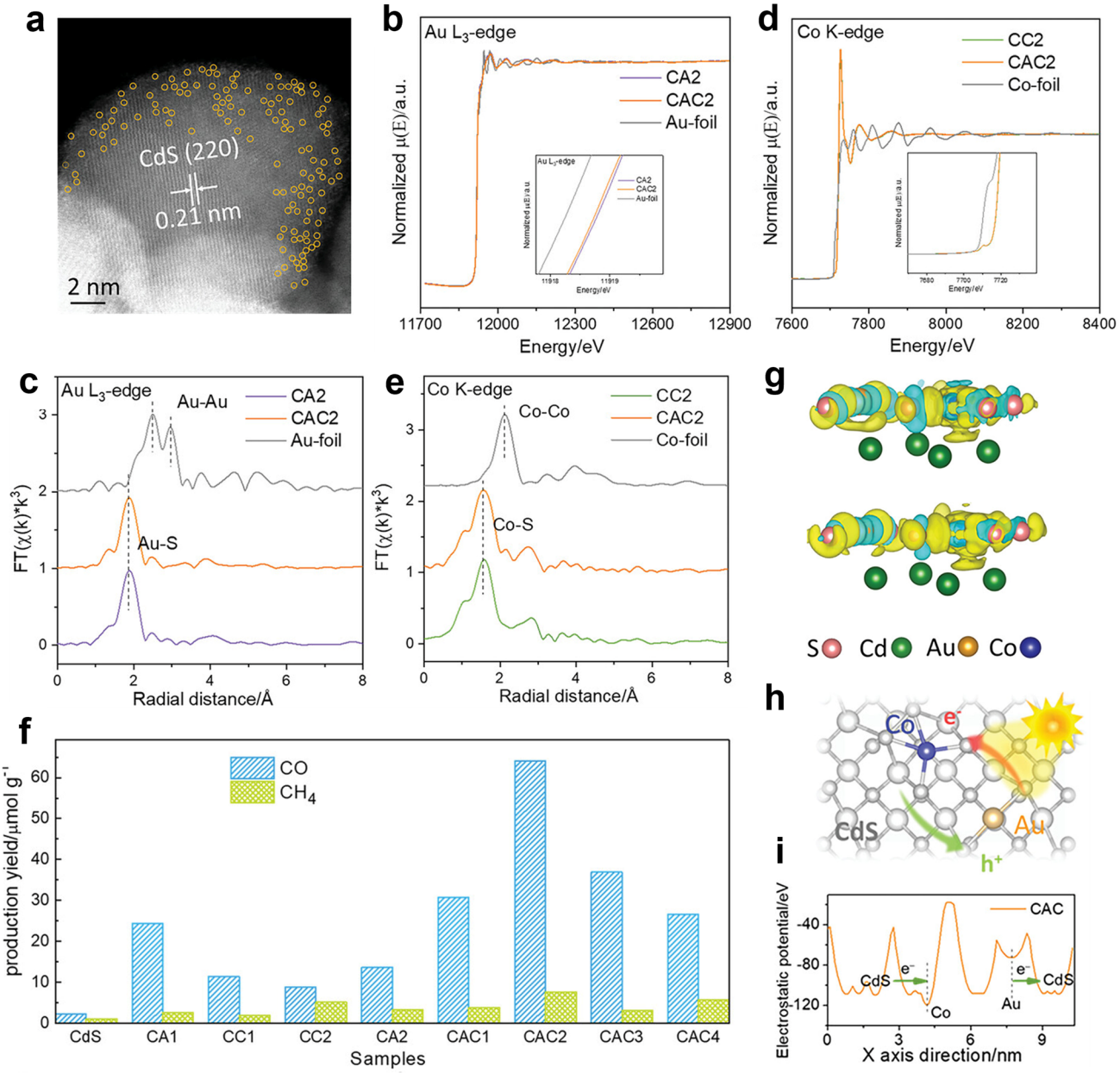


Figure 14. (**a**) Atomic-resolution HAADF-STEM image of CAC2. (**b**) XANES and (**c**) corresponding EXAFS spectra for Au L_3-edge for CAC2, CA2, and Au-foil. (**d**) XANES and (**e**) corresponding EXAFS spectrafor Co K-edge for CAC2, CC2, and Co-foil. (**f**) Photocatalytic CO_2 reduction performance of CdS, CA1, CC1, CC2, CA2, CAC1, CAC2, CAC3, and CAC4 under visible-light illumination ($\lambda > 400$ nm). (**g**) Charge density distribution of CAC before (top side) and following (bottom side) introduction of extra electrons in the model. The iso-surface value is 0.0045e $Å^{-3}$. Charge depletion and accumulation are labeled in cyan-color and yellow, respectively. (**h**) Scheme for charge redistribution between DSA ad CdS nanoparticles under illumination. (**i**) Electrostatic potential energy along the x-axis for CAC model [172].

 https://doi.org/10.53941/ges.2026.100027

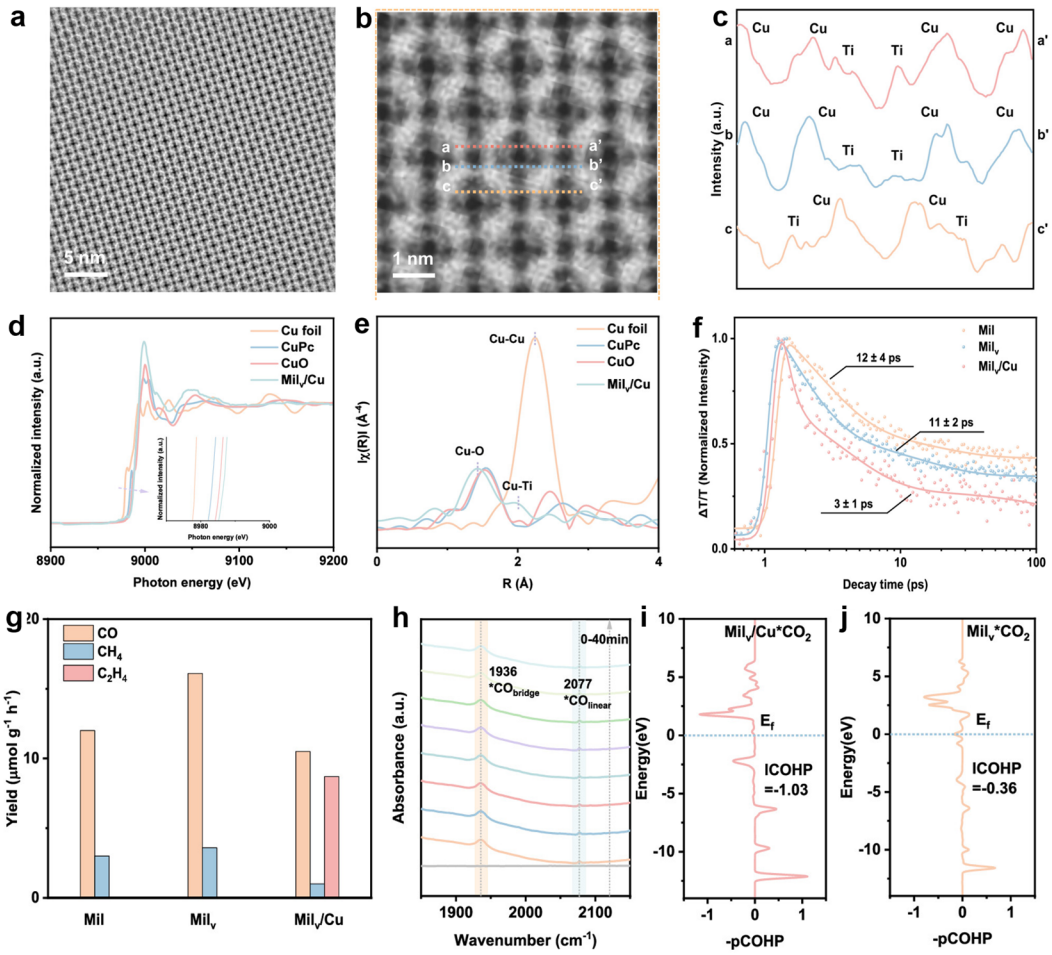


Figure 15. (**a**) Low-dose real-space TEM image of Mil$_v$/Cu. (**b**) Magnified low-dose real-space HRTEM image and corresponding model of the Mil$_v$/Cu structure for detailed analysis. (**c**) Intensity profiles extracted from the dotted lines in panel. (**d**) Normalized XANES spectra at the Cu K-edge of Mil$_v$/Cu. (**e**) Fourier transforms of EXAFS spectra at the Cu K-edge. WT of EXAFS of the Cu K-edge. (**f**) TA decay curves of Mil, Mil$_v$, and Mil$_v$/Cu. Solid lines are fits to the data, and the average lifetimes are presented. (**g**) Photocatalytic yield of Mil, Mil$_v$, and Mil$_v$/Cu. (**h**) *In Situ* DRIFTS measurements between 1850 and 2150 cm^{-1} over Mil/Cu. COHP between (**i**) Mil/Cu and CO_2, and (**j**) Mil and CO_2. Reprinted with permission from Ref. [151]. Copyright 2025, American Chemical Society.

Wu et al. [176] first proposed a dual-regulation strategy to concurrently modulate the reduction center via heteroatom substitution and the oxidation center via 2,2,6,6-tetramethylpiperidoxyl (TEMPO) coordination in cobalt porphyrin-based MOFs (Co-MOFs), resulting in a series of strong redox photocatalysts (TEMPO@Co-XN$_3$-MOF, X = N, O, and S) for efficient CO_2 photoreduction. Among them, the dual-modulated TEMPO@Co-SN$_3$-PCN exhibits excellent photocatalytic performance, with a CO yield as high as 2000 μmol g^{-1}, which is more than 10 times and 50 times that of the single-modulated Co-SN$_3$-PCN and the traditional Co-N$_4$-PCN, respectively. Meanwhile, it realizes the photooxidation of lactic acid to pyruvic acid (85% yield) and the *in situ* carbonylation reaction of CO (90% yield), providing a new pathway for photosynthesis with negative carbon emissions. Substitution of N atoms in Co–N$_4$ with heteroatoms (O/S) regulates the coordination environment of Co (Co–ON$_3$ and Co–SN$_3$), which significantly enhances CO_2 adsorption/activation and lowers the reaction energy barrier. The introduction of TEMPO effectively traps photogenerated holes, promotes the migration of holes from ligands to TEMPO, significantly suppresses electron-hole recombination, and improves charge separation efficiency. Fluorescence lifetime measurements showed that the lifetime of TEMPO@Co-SN$_3$-PCN was extended to 1.7 ns. PL spectroscopy and photoelectrochemical measurements demonstrated that the dual-modulated catalyst possessed the lowest charge recombination rate and the smallest charge transfer resistance. The synergistic effect of the reduction center and oxidation center enabled efficient charge separation and utilization, while facilitating CO_2 reduction and lactic acid oxidation. Zhou et al. [94] successfully regulated the active sites of the photocatalyst via a feasible strategy of modulating isolated metal sites in MOFs. By coordinating transition metals (Co, Ni, Fe) with Cu ions and tetrahydroxyquinone (THQ) ligands, they constructed atomically dispersed

bimetallic-site two-dimensional MOF catalysts (CuM-THQ, M = Co, Ni, Fe) with high activity. Under visible-light irradiation with a photosensitizer, the CuCo bimetallic sites exhibited an excellent CO evolution rate of 1626 μmol g^{-1} h^{-1}, which was 37 times that of the monometallic Cu-THQ, with a selectivity approaching 100%. In contrast to the ligand-to-metal charge transfer (LMCT) in Cu-THQ, the atomically isolated Co sites in CuCo-THQ induced an extended charge separation distance via metal-to-metal charge transfer (MMCT). The fluorescence lifetime was prolonged from 1.21 ns to 2.49 ns. The isolated Cu sites acted as electron acceptors and exhibited high orbital hybridization activity with adsorbed CO_2, thereby facilitating CO_2 adsorption and activation. The Co sites optimized the adsorption energy of the *COOH intermediate, reducing the energy barrier of the rate-determining step (CO_2 → *COOH) from 0.88 eV to 0.55 eV. In addition, the Co sites weakened the adsorption strength of the Cu sites toward the *CO intermediate, avoiding its over-hydrogenation to form CH_4. Meanwhile, the uniform spacing of Cu sites (6.69 Å) in the MOF framework inhibited the coupling of C_1 intermediates to form C_{2+} products, thus ensuring high CO selectivity.

6.6. COF-Supported Dual-Atom Catalysts

Covalent organic frameworks (COFs) are a class of porous polymers with periodic structures and high crystallinity, which are formed by connecting organic units via covalent bonds [177]. Similar to MOFs, COFs possess high specific surface areas, tunable pore sizes, and designable chemical environments. Meanwhile, the all-organic skeletons of COFs generally exhibit superior chemical stability and more flexible π-electron conjugated systems [153]. These characteristics render them ideal platforms for anchoring metal active sites and constructing high-efficiency photocatalysts. Owing to the intrinsic large pores, COFs can integrate active metal sites into extended frameworks, and the metal atoms have well-defined coordination environments. By precisely introducing metal atoms into their pores or ligand sites via post-synthesis, single-atom or dual-atom catalytic centers with well-defined structures can be constructed, which effectively facilitate the separation of photogenerated charges, the adsorption and activation of CO_2, and the selective generation of target products.

Zhou et al. [152] adopted an electrostatically driven self-assembly method, skillfully designed and synthesized an atomically dispersed bimetallic photocatalytic material, LaNi-Phen/COF-5, with the assistance of the ligand phenanthroline as the bridging linker (Figure 16a). XAS results demonstrate that the two metals existed in the form of single atoms and formed La–Ni dual-atom sites with an interatomic distance of approximately 2.8 Å. After metal coordination, the light absorption of LaNi-Phen/COF-5 underwent a red shift, with its band gap reduced to 2.86 eV. In comparison with Ni-Phen/COF-5, the light absorption of La-Phen/COF-5 exhibited a distinct red shift, indicating that the rare-earth metal La, acting as a photoactive center, was conducive to light harvesting (Figure 16b). The La single-atom sites served as photoactive centers for photogenerated carrier generation, while the Ni single-atom sites acted as catalytic active centers for the highly selective CO_2-to-CO reduction. Moreover, the monodispersed La–Ni dual-atom sites exhibited obvious interactions and synergistic effects. The photocatalytic performance of the LaNi-Phen/COF-5 catalyst was tested and analyzed, showing a maximum CO evolution rate of 605.8 μmol g^{-1} h^{-1} with a selectivity as high as 98.2% (the H_2 evolution rate was 39.9 μmol g^{-1} h^{-1}), along with excellent photocatalytic cycling stability (Figure 16c,d). Further mechanistic analysis of the PCO_2RR, conducted via theoretical calculations, reveals that the formation energy of *COOH was 0.65 eV, which constituted the key step for improving the CO yield. Analysis of the HOMO-LUMO charge transition process of LaNi-Phen/COF-5 indicates that the HOMO energy level is mainly located on Ni-Phen, whereas the LUMO energy level is situated on La-Phen. As the photoactive center and electron donor, La guided the migration of photogenerated electrons to the active centers through the COF-5 framework, enabling the efficient reduction of CO_2 to CO (Figure 16e). Wang et al. [153] synthesized four crystalline porous benzothiadiazole-based COFs with different carbonyl groups via a Schiff base reaction. Subsequently, these benzothiadiazole-based COFs were functionalized with Co and Ni as active centers through interactions between the metals and the thiadiazole units. Among the as-synthesized COFs metalated with Co and Ni dual sites, CoNi-COF-3 achieved an impressive CO generation rate of 2567 μmol g^{-1} h^{-1} and a high selectivity of 92.2% under conditions involving sacrificial agents and photosensitizers. This performance was significantly superior to that of catalysts with single metal sites. Experimental and theoretical results reveal that the superior photocatalytic performance is attributed to the synergic effect of the fully β-ketoenamine-tautomerized COF-3 configuration and dual-metal sites, which not only facilitated the photogenerated charge carrier dynamics but also reduced the energy barriers of *COOH formation and promoted CO_2 adsorption and CO desorption. This work provides valuable insights into the future design of improved COF photocatalysts for high-performance CO_2 conversion.

 https://doi.org/10.53941/ges.2026.100027

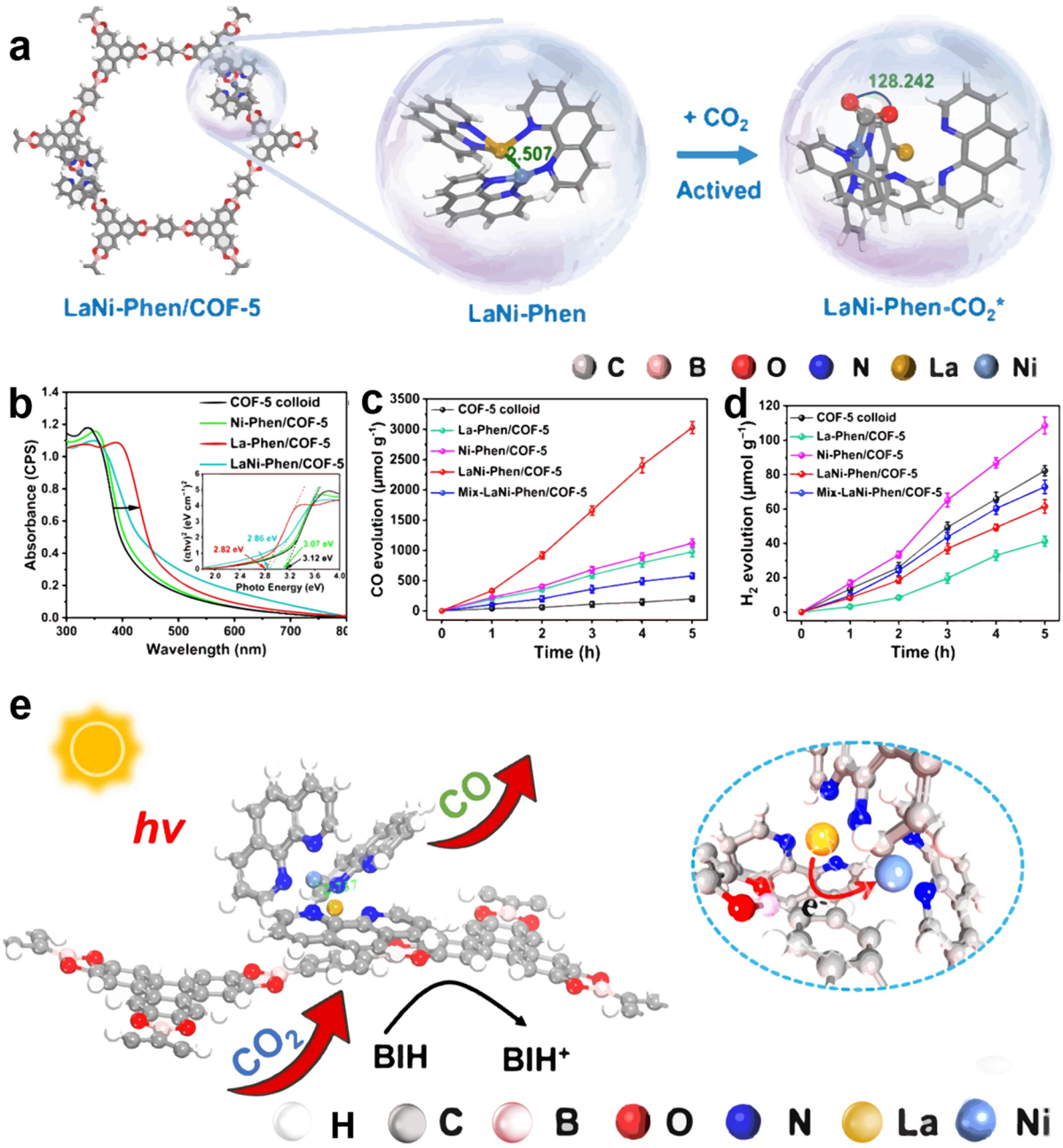


Figure 16. (**a**) Schematic diagram of the photocatalytic CO_2 reduction in LaNi-Phen/COF-5. (**b**) UV-vis diffuse reflectance spectra of COF-5 colloid, Ni-Phen/COF-5, La-Phen/COF-5 and LaNi-Phen/COF-5. (Inset: Tauc plots of LaNi-Phen/COF-5) (**c**,**d**) Time-dependent CO (**c**) and H_2 (**d**) evolution curves under UV-vis light irradiation (λ > 380 nm) within 5 h using COF-5 colloid (black spheres), La-Phen/COF-5 (green spheres), Ni-Phen/COF-5 (pink spheres), LaNi-Phen/COF-5 (red spheres), and mix-LaNi-Phen/COF-5 (blue spheres). (**e**) Schematic illustration of charge transfer in the photocatalytic CO_2 reaction over LaNi-Phen/COF-5. Adapted from Ref. [152].

DACs supported on different carriers exhibit significant differences in performance for photocatalytic CO_2 reduction, and the carrier effects are mainly reflected in the following aspects: (1) Electronic structure regulation: Carriers modulate the d-band centers of bimetallic sites via heteroatom coordination to optimize intermediate adsorption, and regulate the kinetic behavior of electron transfer through metal-support interactions. (2) Structural stability: Improving the electrical conductivity and chemical stability of carriers, as well as precisely controlling the spacing and coordination environment of dual-atom sites, is conducive to long-term catalytic stability. (3) Product selectivity: DACs supported on carbon-based carriers are dominated by C_1 products, while DACs supported on oxide carriers have advantages in the generation of C_{2+} products. DACs supported on MOF and COF carriers hold great potential for the production of C_{2+} products.

7. Challenges of Dual-Atom Catalysts in Photocatalytic CO_2 Reduction Reaction

Despite the significant progress made by DACs in the field of photocatalytic CO_2 reduction, several challenges still need to be addressed for their practical application, including synthetic precision, catalyst stability, understanding of reaction mechanisms, and large-scale application.

7.1. Insufficient Synthetic Precision

The catalytic performance of DACs is highly dependent on the coordination environment of dual-atom sites, but current synthetic methods still struggle to achieve precise regulation of the coordination structures of dual-atom sites. On the one hand, it is difficult to control the loading amounts of bimetallic sites: an excessively low loading leads to insufficient active sites, while an excessively high loading tends to induce metal agglomeration to form clusters and NPs. On the other hand, it is hard to accurately control the spacing and coordinating atoms of dual-atom sites. The distribution of bimetallic sites is random, and their coordination structures are susceptible to synthetic conditions, making precise regulation difficult. Moreover, the currently characterized coordination environments are all local and averaged concepts, usually presented as a distribution, which fails to accurately characterize the proportion of specific coordinating atoms. It is also difficult to precisely characterize and reproduce the bond lengths/bond angles as well as the local strain states of the support. In addition, the synthesis of heteronuclear DACs faces greater challenges. The adsorption, diffusion and reduction kinetics of the two metal precursors on the support surface are different, and the competitive coordination of metal ions tends to lead to the formation of single-metal sites, while it is difficult to ensure that they can always be synchronously and adjacently trapped at the preset anchoring sites of the support.

7.2. The Catalytic Stability Needs Further Improvement

DACs are prone to activity degradation during long-term PCO_2RR reactions, mainly attributed to the following reasons: (1) Loss and agglomeration of dual-atom sites. Under prolonged illumination and reaction atmosphere (e.g., H_2O, CO_2), photogenerated carriers and thermal effects may break the metal-support coordination bonds, leading to the migration and agglomeration of metal atoms. (2) Instability of the support's own structure. For instance, supports such as MOFs are susceptible to crystal structure collapse under light and hydrothermal conditions, while sulfide supports may undergo photo corrosion. For DACs supported on defective metal oxides or carbon-based supports, activity decay may stem from the reconstruction, coverage, or annihilation of vacancy anchoring sites, which in turn induces the agglomeration of metal sites. (3) Poisoning of active sites. Strong adsorption of key intermediates results in the poisoning of active sites, gradually altering the electronic state and coordination structure of metal centers and thus leading to their deactivation. For example, the excessive adsorption of *CO intermediates on metal sites can hinder the further adsorption and activation of reactants, reducing the catalytic activity.

7.3. Insufficient Understanding of Reaction Mechanisms

Despite the progress made by *in situ* characterization techniques and theoretical calculations in characterizing the microstructure of DACs and investigating the reaction mechanism of photocatalytic CO_2 reduction, the dynamic evolution and mechanism of dual-atom sites have not been fully elucidated. Under photoexcitation and reactant adsorption, the oxidation state, spin state, and coordination environment of dual-atom sites are likely to undergo reversible and dynamic evolution. Current *in situ* techniques lack the capability to simultaneously track such dynamic evolution across temporal scales (from femtoseconds to seconds) and spatial scales (atomic level). On the other hand, controversies remain regarding the transformation pathways and synergistic mechanisms of intermediates in multi-step reactions. "Synergy" is a macroscopic description; it remains unclear whether its microscopic essence is realized through direct spatial electron transfer, indirect mediation by the support, or a combination of both. A unified understanding has not yet been reached regarding the specific pathways of C–C coupling and the division of roles of dual-atom sites in different reaction steps. It is difficult to explore whether two intermediates are adsorbed on dual-atom sites for reaction simultaneously or sequentially on a single atom. In addition, it is challenging to quantify the role of the support in PCO_2RR. The support may act as an electron buffer pool, proton source, or participate in coordination. The impact of metal-support interactions on the reaction mechanism needs to be further investigated, and quantifying the energy contribution of metal-support interactions in specific reaction steps is a great challenge faced by current theoretical calculations.

7.4. Large-Scale Application Faces Bottlenecks

At present, research on DACs is mainly limited to small-scale laboratory synthesis and performance testing, and large-scale preparation technologies remain immature. Traditional synthetic methods suffer from low yields and high costs, which are difficult to meet the demands of practical applications. DACs using noble metals exhibit outstanding performance but are prohibitively expensive. In contrast, for DACs based on cheap metals, it is hard to ensure the structural uniformity of the catalysts during large-scale preparation, leading to a significant decline in catalytic performance. The photocatalytic efficiency and long-term stability of DACs

 https://doi.org/10.53941/ges.2026.100027

still need to be further improved to meet the requirements of industrial applications. In addition, most research on DACs focuses on the catalysts themselves, lacking collaborative research and integrated innovation with reaction systems, photoreactor design, mass transfer optimization, and product separation systems.

8. Future Outlook

To address the current challenges of DACs in photocatalytic CO_2 reduction, in combination with the cutting-edge research directions, the future development trends will mainly focus on the following aspects:

8.1. Development of Precise Synthesis Strategies

Develop high-precision synthesis technologies to achieve the controllable preparation of dual-atom sites. On the one hand, advanced synthetic strategies such as ALD and spatial/ligand confinement are employed to precisely regulate the loading amount, spacing, and coordination environment of bimetallic sites, thus ensuring the uniform distribution of the sites. On the other hand, by integrating ML and high-throughput calculations, the structure-activity relationship between the structure of dual-atom sites and catalytic performance is established to rapidly screen optimal metal combinations and support types, thereby guiding experimental synthesis. In addition, novel binuclear metal complex precursors such as bimetallic MOFs and metal clusters are developed; by leveraging their unique rigid skeletons, researchers can retain the pre-designed metal spacing and ligand environment to the maximum extent during pyrolysis or assembly processes. This enables the *in situ* generation of dual-atom sites and improves the synthesis efficiency and structural stability of DACs.

8.2. Optimization of Catalytic Stability

The stability of DACs is enhanced via support modification and site decoration. On the one hand, the support is functionalized to strengthen metal-support interactions. Heteroatoms such as P and S are introduced into the support to form more stable M–N–P and M–N–S coordination structures. Alternatively, rigid ligands are incorporated into MOF supports to improve the hydrothermal stability of their crystal structures. On the other hand, core-shell or heterostructures are constructed to protect dual-atom sites and prevent the leaching and agglomeration of metal sites. In addition, interface engineering is employed to regulate the adsorption strength of reaction intermediates, which avoids the poisoning of active sites while enhancing the activation ability of CO_2. It is necessary to develop stability testing and structure-monitoring systems, establish standardized methods for evaluating light, thermal, and chemical stresses, and couple online mass spectrometry, chromatography, and *in situ* spectroscopy to correlate activity degradation with structural changes in real time.

8.3. In-Depth Investigation of Reaction Mechanisms

The dynamic catalytic mechanisms of DACs are revealed by combining advanced *in situ* characterization techniques with multi-scale theoretical calculations. Time-resolved *in situ* and operando spectroscopy techniques (e.g., *in situ* DRIFTS/Raman spectroscopy, operando synchrotron XAS spectroscopy) are developed to monitor both the evolution of surface intermediates and the dynamic restructuring of dual-atom sites. In particular, *operando* EXAFS/XANES spectroscopy techniques enable the direct correlation between catalytic performance and the electronic/geometric evolution of active sites, which is crucial for DACs that are often thermodynamically metastable and prone to structural reconstruction under light irradiation and in aqueous environments. *In Situ* electron microscopy is employed to directly observe the dynamic behaviors of dual-atom sites during the reaction process. Meanwhile, more accurate reaction kinetic models are constructed by integrating DFT calculations with machine learning, clarifying the microscopic mechanisms of dual-atom synergy, metal-support interactions, and intermediate transformation. In addition, isotope labeling experiments are carried out to trace the carbon migration pathways of CO_2 molecules in catalytic reactions, identify the origin of product formation, and provide more direct theoretical support for catalyst design.

8.4. Breakthroughs in Large-Scale Application Technologies

Develop efficient and low-cost large-scale synthesis technologies to promote the practical application of DACs. Apply technologies such as microwave-assisted synthesis and continuous flow reaction to the large-scale preparation of DACs, so as to improve the yield and production efficiency. Optimize the synthesis process, reduce the proportion of noble metals, and develop noble-metal-free DACs to cut down costs. Meanwhile, construct efficient photocatalytic reaction systems, and combine technologies such as photothermal synergistic catalysis and photoelectric coupling catalysis to enhance solar energy utilization efficiency and CO_2 conversion efficiency. In addition, carry out research on the application of DACs in CO_2 reduction from actual flue gas, and address the impact of impurity gases (e.g., SO_2, NO_x) in practical systems on catalytic performance.

8.5. Exploration of Novel Supports and Dual-Atom Systems

Expand novel support materials and develop DAC systems with superior performance. For instance, explore two-dimensional materials (e.g., MXenes, black phosphorus) as supports for DACs, and leverage their high

conductivity and unique electronic structures to facilitate the separation of photogenerated charges. Explore novel dual-atom systems, such as rare-earth metal or transition metal and main-group metal or transition metal dual-atom sites, to develop DACs with unique electronic structures, breaking through the performance bottlenecks of traditional transition metal-based DACs. In addition, construct multi-atom site catalysts (e.g., tri-atom, tetra-atom catalysts) to further optimize the synergistic catalytic effect and realize more complex CO_2 conversion reactions.

9. Conclusions

DACs, by virtue of their unique dual-site synergistic effect and ultrahigh atomic utilization efficiency, provide a highly promising solution for overcoming the long-standing limitations of photocatalytic CO_2 reduction in both activity and selectivity. As an indispensable component, the support plays a decisive role in regulating the local coordination structure, electronic state, and reaction microenvironment of dual-atom sites through metal-support interactions, thereby steering distinct reaction pathways. Such atomic-level tunability opens new opportunities to address the intrinsic trade-off between catalytic activity and stability in conventional systems. Nevertheless, the practical application of DACs is still confronted with numerous challenges, including insufficient synthetic precision, poor stability under working conditions, unclear dynamic reaction mechanisms, and difficulties in large-scale preparation. To bridge the gap between fundamental research and practical application, it is essential to establish quantitative performance benchmarks for photocatalytic systems. For example, achieving high product selectivity (e.g., >90%), high apparent quantum efficiency (AQE), and long-term operational stability (e.g., >100 h without significant performance decay) will be crucial for evaluating the industrial viability of DACs. In the future, research should move beyond conventional trial-and-error approaches toward the rational design and fabrication of DACs with atomic-level precision. This requires developing precise synthesis technologies, revealing the structure-activity relationship using advanced *in situ* characterization techniques, designing DAC systems oriented toward large-scale production and stability, exploring novel supports and dual-atom systems, and thoroughly investigating their PCO_2RR mechanisms. In particular, integrating operando spectroscopic techniques with theoretical calculations and data-driven methods will enable predictive catalyst design and controllable synthesis at the atomic scale. This review systematically summarizes the synthetic strategies, advanced characterization methods, catalytic performance, and reaction mechanisms of DACs based on different supports. More importantly, it provides a clearer technical blueprint by combining quantitative performance targets with precision manufacturing strategies, thereby promoting the transition of photocatalytic CO_2 reduction from empirical exploration to atomic-level precision engineering.

Author Contributions

S.H.: Conceptualization, investigation and original draft. Z.X.: Figure preparation, original draft and editing. Q.L. and X.L.: Investigation, review & editing. D.Z.: Supervision, review & editing, funding acquisition. All authors have read and agreed to the published version of the manuscript.

Funding

This work was supported by the National Natural Science Foundation of China (Nos. 22376142, 22305157, 22022608, and 22176127), Shanghai Eastern Talent Plan Leading Project (No. LJ2024115), the Shanghai Engineering Research Center of Green Energy Chemical Engineering (No. 18DZ2254200), “111” Innovation and Talent Recruitment Base on Photochemical and Energy Materials (No. D18020), the Shanghai Postdoctoral Excellence Program (No. 2024498), and the China National Funding Program for Postdoctoral Researchers (No. GZC20250829).

Institutional Review Board Statement

Not applicable.

Informed Consent Statement

Not applicable.

Data Availability Statement

Not applicable.

Conflicts of Interest

The authors declare no conflict of interest.

Use of AI and AI-Assisted Technologies

During the preparation of this work, the authors used DeepSeek-V4 to revise grammatical errors and enhance language quality. After using this tool, the authors reviewed and edited the content as needed and take full responsibility for the content of the published article.

References

1. Figueres, C.; Le Quéré, C.; Mahindra, A.; et al. Emissions Are Still Rising: Ramp up the Cuts. *Nature* **2018**, *564*, 27–30.
2. Peters, G.P.; Andrew, R.M.; Canadell, J.G.; et al. Carbon Dioxide Emissions Continue to Grow amidst Slowly Emerging Climate Policies. *Nat. Clim. Change* **2020**, *10*, 3–6.
3. Zhang, S.; Chen, W. Assessing the Energy Transition in China towards Carbon Neutrality with a Probabilistic Framework. *Nat. Commun.* **2022**, *13*, 87.

4. Li, L.; Zhang, Y.; Zhou, T.; et al. Mitigation of China's Carbon Neutrality to Global Warming. *Nat. Commun.* **2022**, *13*, 5315.
5. Kornienko, N.; Zhang, J.Z.; Sakimoto, K.K.; et al. Interfacing Nature's Catalytic Machinery with Synthetic Materials for Semi-Artificial Photosynthesis. *Nat. Nanotechnol.* **2018**, *13*, 890–899.
6. Bonchio, M.; Bonin, J.; Ishitani, O.; et al. Best Practices for Experiments and Reporting in Photocatalytic CO_2 Reduction. *Nat. Catal.* **2023**, *6*, 657–665.
7. Hemminger, J.; Carr, R.; Somorjai, G. The Photoassisted Reaction of Gaseous Water and Carbon Dioxide Adsorbed on the $SrTiO_3$ (111) Crystal Face to form Methane. *Chem. Phys. Lett.* **1978**, *57*, 100–104.
8. Inoue, T.; Fujishima, A.; Konishi, S.; et al. Photoelectrocatalytic Reduction of Carbon Dioxide in Aqueous Suspensions of Semiconductor Powders. *Nature* **1979**, *277*, 637–638.
9. Morikawa, T.; Sato, S.; Sekizawa, K.; et al. Solar-Driven CO_2 Reduction Using a Semiconductor/Molecule Hybrid Photosystem: From Photocatalysts to a Monolithic Artificial Leaf. *Acc. Chem. Res.* **2022**, *55*, 933–943.
10. Qiao, B.; Wang, A.; Yang, X.; et al. Single-Atom Catalysis of CO Oxidation Using Pt_1/FeOx. *Nat. Chem.* **2011**, *3*, 634–641.
11. Ding, J.; Liu, L.; Yang, H.B.; et al. Integrative Catalytic Pairs Driving Complex Chemical Reactions. *Nat. Rev. Chem.* **2025**, *9*, 826–840.
12. Liu, L.; Corma, A. Metal Catalysts for Heterogeneous Catalysis: From Single Atoms to Nanoclusters and Nanoparticles. *Chem. Rev.* **2018**, *118*, 4981–5079.
13. Shi, X.; Wen, Z.; Gu, Q.; et al. Metal-Support Frontier Orbital Interactions in Single-Atom Catalysis. *Nature* **2025**, *640*, 668–675.
14. Cui, X.; Liu, K.; Han, Y.; et al. Rational Design of Single-Atom Catalysts for Efficient Hydrogenation of Nitro Compounds. *Chem. Synth.* **2025**, *5*, 79.
15. Pu, T.; Ding, J.; Zhang, F.; et al. Dual Atom Catalysts for Energy and Environmental Applications. *Angew. Chem. Int. Ed.* **2023**, *62*, e202305964.
16. Xie, Y.; Chen, X.; Sun, K.; et al. Direct Oxygen-Oxygen Cleavage through Optimizing Interatomic Distances in Dual Single-Atom Electrocatalysts for Efficient Oxygen Reduction Reaction. *Angew. Chem. Int. Ed.* **2023**, *62*, e202301833.
17. Xue, D.; Zhao, Y.; Cao, J.; et al. Spin Engineering of Dual-Atom Site Catalysts for Efficient Electrochemical Energy Conversion. *Adv. Mater.* **2025**, *37*, 2504213.
18. Yardimci, D.; Serna, P.; Gates, B.C. Surface-Mediated Synthesis of Dimeric Rhodium Catalysts on MgO: Tracking Changes in the Nuclearity and Ligand Environment of the Catalytically Active Sites by X-Ray Absorption and Infrared Spectroscopies. *Chem. Eur. J.* **2013**, *19*, 1235–1245.
19. Wang, J.; Huang, Z.; Liu, W.; et al. Design of N-Coordinated Dual-Metal Sites: A Stable and Active Pt-Free Catalyst for Acidic Oxygen Reduction Reaction. *J. Am. Chem. Soc.* **2017**, *139*, 17281–17284.
20. Wang, T.; Hu, J.; Ouyang, R.; et al. Nature of Metal-Support Interaction for Metal Catalysts on Oxide Supports. *Science* **2024**, *386*, 915–920.
21. Hu, S.; Li, W.-X. Sabatier Principle of Metal-Support Interaction for Design of Ultrastable Metal Nanocatalysts. *Science* **2021**, *374*, 1360–1365.
22. Zhong, D.-C.; Wang, Y.-C.; Wang, M.; et al. Precise Synthesis of Dual-Atom Catalysts for Better Understanding the Enhanced Catalytic Performance and Synergistic Mechanism. *Acc. Chem. Res.* **2025**, *58*, 1379–1391.
23. Li, Y.; Li, Y.; Sun, H.; et al. Current Status and Perspectives of Dual-Atom Catalysts towards Sustainable Energy Utilization. *Nano-Micro Lett.* **2024**, *16*, 139.
24. Shang, Z.; Feng, X.; Chen, G.; et al. Recent Advances on Single-Atom Catalysts for Photocatalytic CO_2 Reduction. *Small* **2023**, *19*, 2304975.
25. Xue, Z.-H.; Luan, D.; Zhang, H.; et al. Single-Atom Catalysts for Photocatalytic Energy Conversion. *Joule* **2022**, *6*, 92–133.
26. Shang, H.; Jia, H.; Li, P.; et al. Highly Selective and Efficient Photocatalytic NO Removal: Charge Carrier Kinetics and Interface Molecular Process. *Nano Res.* **2024**, *17*, 1003–1026.
27. Xiao, S.; Zhang, D.; Pan, D.; et al. A Chloroplast Structured Photocatalyst Enabled by Microwave Synthesis. *Nat. Commun.* **2019**, *10*, 1570.
28. Xie, Z.; Cheng, W.; Luo, H.; et al. Artificial Photothermal Synthesis of Hydrocarbons from CO_2 and H_2O. *Adv. Energy Mater.* **2026**, *16*, 2501840.
29. Zhang, Y.; Xia, B.; Ran, J.; et al. Atomic-Level Reactive Sites for Semiconductor-Based Photocatalytic CO_2 Reduction. *Adv. Energy Mater.* **2020**, *10*, 1903879.
30. Zhan, H.; Zhou, R.; Liu, K.; et al. Progress and Challenges of Photocatalytic Reduction of CO_2 with g-C_3N^{4-} Based Photocatalysts in the Context of Carbon Neutrality. *Sci. China Mater.* **2024**, *67*, 1740–1764.
31. Chang, X.; Wang, T.; Gong, J. CO_2 Photo-Reduction: Insights into CO_2 Activation and Reaction on Surfaces of Photocatalysts. *Energy Environ. Sci.* **2016**, *9*, 2177–2196.
32. Karamian, E.; Sharifnia, S. On the General Mechanism of Photocatalytic Reduction of CO_2. *J. CO_2 Util.* **2016**, *16*, 194–203.
33. Guo, S.; Deng, Z.; Li, M.; et al. Phosphorus-Doped Carbon Nitride Tubes with a Layered Micro-Nanostructure for Enhanced Visible-Light Photocatalytic Hydrogen Evolution. *Angew. Chem. Int. Ed.* **2016**, *55*, 1830–1834.
34. Hu, S.; Qiao, P.; Zhang, L.; et al. Assembly of TiO_2 Ultrathin Nanosheets with Surface Lattice Distortion for Solar-Light-Driven Photocatalytic Hydrogen Evolution. *Appl. Catal. B Environ.* **2018**, *239*, 317–323.
35. Zhou, S.; Wang, L.; Gao, S.; et al. Research Progress on Preparation of Metal Oxide Catalysts with Porous Structure and Their Catalytic Purification of Diesel Engine Exhausts Gases. *ACS Catal.* **2024**, *14*, 6062–6127.

36. Farber, E.M.; Seraphim, N.M.; Tamakuwala, K.; et al. Porous Materials: The next Frontier in Energy Technologies. *Science* **2025**, *390*, eadn9391.
37. Chen, F.; Li, J.; Li, N.; et al. Noncopper Photocatalysts for Visible-Light-Driven Conversion of CO_2 into C^{2+} Products. *Energy Environ. Mater.* **2026**, *9*, e70177.
38. Xiao, W.; Zhang, J.; Wu, J. Recent Advances in Reactions Involving Carbon Dioxide Radical Anion. *ACS Catal.* **2023**, *13*, 15991–16011.
39. Azzi, E.; Rodríguez-Martínez, M.; Kolusu, S.R.N.; et al. Photolysis of CO_2 Carbamate for Hydrocarboxylation Reactions. *J. Am. Chem. Soc.* **2026**, *148*, 3801–3810.
40. He, H.; Ren, Y.; Zhu, Y.-H.; et al. Continuous Flow Photothermal Catalytic CO_2 Reduction: Materials, Mechanisms, and System Design. *ACS Catal.* **2025**, *15*, 10480–10520.
41. Bian, J.; Zhang, Z.; Liu, Y.; et al. Strategies and Reaction Systems for Solar-Driven CO_2 Reduction by Water. *Carbon Neutrality* **2022**, *1*, 5.
42. Liu, Y.; Zhou, Y. Synergistic Mechanisms of Dual-Metal Single-Atoms Catalysts for Promoting CO_2 Photoreduction: Bifunctional, Intersite Distance, and Electronic Effects. *ACS Catal.* **2025**, *15*, 10957–10970.
43. Li, Q.; Wang, L.G.; Wu, J.B. Recent Advances in Dual-Atom Catalysts for Energy Catalysis. *Rare Met.* **2025**, *44*, 841–867.
44. Hu, Y.; Li, Z.; Li, B.; et al. Recent Progress of Diatomic Catalysts: General Design Fundamentals and Diversified Catalytic Applications. *Small* **2022**, *18*, 2203589.
45. Xu, Z.L.; Ao, Z.M.; Yang, M.; et al. Recent Progress in Single-atom Alloys: Synthesis, Properties, and Applications in Environmental Catalysis. *J. Hazard. Mater.* **2022**, *424*, 127427.
46. Zhang, Z.; Dai, Y.; Guo, P.; et al. Noncovalent Assembly Strategy for Efficient Synthesis of Dual-Atom Catalysts. *Adv. Funct. Mater.* **2024**, *34*, 2407128.
47. Chen, X.; Wang, M.; He, Y.; et al. A Highly Efficient and Regenerable Ir_1–Cu_1 Dual-Atom Catalyst for Low-Temperature Alkane Dehydrogenation. *Nat. Catal.* **2025**, *8*, 436–447.
48. Zhao, Y.; Gao, Z.; Zhang, S.; et al. Asymmetric-Charge-Distributed Co–Mn Diatomic Catalyst Enables Efficient Oxygen Reduction Reaction. *Adv. Funct. Mater.* **2025**, *35*, 2504260.
49. Chala, S.A.; Lakshmanan, K.; Huang, W.-H.; et al. Cooperative Dual Single Atom Ni/Cu Catalyst for Highly Selective CO_2-to-Ethanol Reduction. *Appl. Catal. B Environ. Energy* **2024**, *358*, 124420.
50. Yao, D.; Tang, C.; Zhi, X.; et al. Inter-Metal Interaction with a Threshold Effect in NiCu Dual-Atom Catalysts for CO_2 Electroreduction. *Adv. Mater.* **2023**, *35*, 2209386.
51. Hei, P.; Sai, Y.; Li, W.; et al. Diatomic Catalysts for Aqueous Zinc-Iodine Batteries: Mechanistic Insights and Design Strategies. *Angew. Chem. Int. Ed.* **2024**, *63*, e202410848.
52. Pei, Z.; Lu, X.F.; Zhang, H.; et al. Highly Efficient Electrocatalytic Oxygen Evolution over Atomically Dispersed Synergistic Ni/Co Dual Sites. *Angew. Chem. Int. Ed.* **2022**, *61*, e202207537.
53. Zhang, Z.; Li, F.; Xi, S.; et al. Atomic Metal-Nonmetal Catalytic Pair Cooperatively Drives Efficient Enzyme-Mimetic Catalysis. *Angew. Chem. Int. Ed.* **2025**, *64*, e202508651.
54. Sun, Z.; Li, C.; Wei, Z.; et al. Sulfur-Bridged Asymmetric CuNi Bimetallic Atom Sites for CO_2 Reduction with High Efficiency. *Adv. Mater.* **2024**, *36*, 2404665.
55. Liu, Y.; Yang, Y.; Lin, X.; et al. The Geometric-Electronic Coupled Design of Diatomic Catalyst towards Oxygen Reduction Reaction. *Nat. Commun.* **2025**, *16*, 5158.
56. Roth-Zawadzki, A.M.; Nielsen, A.J.; Tankard, R.E.; et al. Dual and Triple Atom Electrocatalysts for Energy Conversion (CO_2 RR, NRR, ORR, OER, and HER): Synthesis, Characterization, and Activity Evaluation. *ACS Catal.* **2024**, *14*, 1121–1145.
57. Jiao, J.; Yuan, Q.; Tan, M.; et al. Constructing Asymmetric Double-Atomic Sites for Synergistic Catalysis of Electrochemical CO_2 Reduction. *Nat. Commun.* **2023**, *14*, 6164.
58. Wang, H.; Zhuang, G.-L.; Fan, Y.; et al. Steering Artificial Photosynthesis via Photoinduced Conversion of Monometallic to Bimetallic Sites in FeCo Nitroprussides. *Nat. Commun.* **2025**, *16*, 6160.
59. Wu, Y.; Jiang, J.X.; Chen, Q.Q.; et al. Synergistic Interplay of Ni Single Atoms and Neighboring Mn_2 Dual Atoms Enabling Selective Photocatalytic Reduction of CO_2 to Propane. *Angew. Chem. Int. Ed.* **2026**, *65*, e21193.
60. Zhang, Y.; Wei, T.; Ding, D.; et al. Aggregation-Induced Equidistant Dual Pt Atom Pairs for Effective CO_2 Photoreduction to C_2H_4. *ACS Catal.* **2025**, *15*, 5614–5622.
61. Greiner, M.T.; Jones, T.E.; Beeg, S.; et al. Free-Atom-like *d* States in Single-Atom Alloy Catalysts. *Nat. Chem.* **2018**, *10*, 1008–1015.
62. Lian, Z.; Luo, D.; Yang, J.; et al. Spatial Decoupling of Adsorption and Transformation Sites on Ag-Cu Dual-Single-Atom Catalysts for Highly Selective Photocatalytic Nitrate-to-Ammonia Reduction. *Angew. Chem. Int. Ed.* **2026**, *65*, e202516964.
63. Liu, B.; Wang, Y.; Hu, X.; et al. Photothermal Dry Reforming of Methane over Supported Bimetal Dual-Atom Pairs. *J. Am. Chem. Soc.* **2026**, *148*, 4743–4753.
64. Mo, S.; Zhao, X.; Li, S.; et al. Non-Interacting Ni and Fe Dual-Atom Pair Sites in N-Doped Carbon Catalysts for Efficient Concentrating Solar-Driven Photothermal CO_2 Reduction. *Angew. Chem. Int. Ed.* **2023**, *62*, e202313868.
65. Cui, T.; Wang, Y.; Xu, R.; et al. Metalloid Coordination Reinforcing Electronic Synergy in Dual-Atom Sites for Large-Scale CO_2 Electrolysis. *Angew. Chem. Int. Ed.* **2026**, *65*, e16353.
66. Zhang, Y.-X.; Zhang, S.; Huang, H.; et al. General Synthesis of a Diatomic Catalyst Library via a Macrocyclic Precursor-Mediated Approach. *J. Am. Chem. Soc.* **2023**, *145*, 4819–4827.

67. Wang, X.; Zhang, N.; Guo, S.; et al. P-d Orbital Hybridization Induced by Asymmetrical FeSn Dual Atom Sites Promotes the Oxygen Reduction Reaction. *J. Am. Chem. Soc.* **2024**, *146*, 21357–21366.
68. Liu, W.; Long, G.; Xiang, Z.; et al. Extremely Active and Robust Ir-Mn Dual-Atom Electrocatalyst for Oxygen Evolution Reaction by Oxygen-Oxygen Radical Coupling Mechanism. *Angew. Chem. Int. Ed.* **2024**, *63*, e202411014.
69. Li, Q.; Jia, C.; Wang, Q.; et al. Rational Design of Conductive MOF-Based Diatomic Electrocatalysts for Selective Ammonia Synthesis. *J. Am. Chem. Soc.* **2025**, *147*, 39430–39439.
70. Yan, H.; Lin, Y.; Wu, H.; et al. Bottom-up Precise Synthesis of Stable Platinum Dimers on Graphene. *Nat. Commun.* **2017**, *8*, 1070.
71. Wang, X.; Zeng, Y.; Wang, P.; et al. A Universal Metal Ion-Targeting Coordination Strategy for Precise Synthesis of Heteronuclear Dual-Atom Electrocatalysts for Oxygen Reduction. *Angew. Chem. Int. Ed.* **2025**, *64*, e202509360.
72. Tran, D.T.; Nguyen, D.C.; Le, H.T.; et al. Recent Progress on Single Atom/Sub-Nano Electrocatalysts for Energy Applications. *Prog. Mater. Sci.* **2021**, *115*, 100711.
73. Yan, G.; Xu, B.; Zhang, R.; et al. Noble-Metal-Free Ni-W Dual-Atom Sites with Bifunctional Synergy for Efficient Photocatalytic CO_2 Conversion. *Appl. Catal. B Environ. Energy* **2025**, *378*, 125535.
74. Chen, T.; Liu, D.; Zhang, M.; et al. Cascade Catalysis on Dual-Atom Iridium-Tungsten Catalysts for Enhanced Ammonia Selective Oxidation. *Nat. Commun.* **2025**, *16*, 11179.
75. Liu, K.; Sun, Z.; Peng, X.; et al. Tailoring Asymmetric RuCu Dual-Atom Electrocatalyst toward Ammonia Synthesis from Nitrate. *Nat. Commun.* **2025**, *16*, 2167.
76. Wang, X.; Xu, L.; Li, C.; et al. Developing a Class of Dual Atom Materials for Multifunctional Catalytic Reactions. *Nat. Commun.* **2023**, *14*, 7210.
77. Mekkering, M.J.; Laan, P.C.M.; Troglia, A.; et al. Bottom-up Synthesis of Platinum Dual-Atom Catalysts on Cerium Oxide. *ACS Catal.* **2024**, *14*, 9850–9859.
78. Van Deelen, T.W.; Hernández Mejía, C.; De Jong, K.P. Control of Metal-Support Interactions in Heterogeneous Catalysts to Enhance Activity and Selectivity. *Nat. Catal.* **2019**, *2*, 955–970.
79. Gong, F.; Xiao, Y.; Wang, H.; et al. Defects and Oxygen Functional Groups Modulated Soft Carbon with Abundant Closed Pores and Robust Interface for High-Performance Na^+-Ion Batteries. *Adv. Funct. Mater.* **2025**, *35*, 2506205.
80. Jones, J.; Xiong, H.; DeLaRiva, A.T.; et al. Thermally Stable Single-Atom Platinum-on-Ceria Catalysts via Atom Trapping. *Science* **2016**, *353*, 150–154.
81. Steinmiller, E.M.P.; Choi, K.S. Photochemical Deposition of Cobalt-Based Oxygen Evolving Catalyst on a Semiconductor Photoanode for Solar Oxygen Production. *Proc. Natl. Acad. Sci. USA* **2009**, *106*, 20633–20636.
82. Lang, R.; Xi, W.; Liu, J.-C.; et al. Non Defect-Stabilized Thermally Stable Single-Atom Catalyst. *Nat. Commun.* **2019**, *10*, 234.
83. Beutel, T.; Sárkány, J.; Lei, G.-D.; et al. Redox Chemistry of Cu/ZSM-5. *J. Phys. Chem.* **1996**, *100*, 845–851.
84. Wang, Y.; Qu, Y.; Qu, B.; et al. Construction of Six-Oxygen-Coordinated Single Ni Sites on g-C_3N_4 with Boron-Oxo Species for Photocatalytic Water-Activation-Induced CO_2 Reduction. *Adv. Mater.* **2021**, *33*, 2105482.
85. Chen, Y.; Wang, P.; Qu, W.; et al. Cu-Ce Dual-Atom Sites Embedded in Zeolites Boost Resistance to Impurity Interference for Environmental Catalysis. *Angew. Chem. Int. Ed.* **2025**, *64*, e202517918.
86. Yan, L.; Mao, Y.; Li, Y.; et al. Sublimation Transformation Synthesis of Dual-Atom Fe Catalysts for Efficient Oxygen Reduction Reaction. *Angew. Chem. Int. Ed.* **2025**, *64*, e202413179.
87. Zhao, R.; Yang, X.-W.; Li, T.H.; et al. The Application of Diatomic Catalysts in Advanced Oxidation Fenton-like Water Treatment Technology: A Mini Review. *Environ. Funct. Mater.* **2024**, *3*, 59–71.
88. Wang, Y.; Cui, X.; Zhang, J.; et al. Advances of Atomically Dispersed Catalysts from Single-Atom to Clusters in Energy Storage and Conversion Applications. *Prog. Mater. Sci.* **2022**, *128*, 100964.
89. Guo, J.; Che, L.; Qin, Y.; et al. Electronic Modification at Atomic Scale: Design and Preparation of Diatomic Structures by Atomic Layer Deposition for Methanol Steam Reforming. *Angew. Chem. Int. Ed.* **2025**, *64*, e202514431.
90. Chen, S.; Gong, B.; Gu, J.; et al. Dehydrogenation of Ammonia Borane by Platinum-Nickel Dimers: Regulation of Heteroatom Interspace Boosts Bifunctional Synergetic Catalysis. *Angew. Chem. Int. Ed.* **2022**, *61*, e202211919.
91. Chen, X.; Cheng, H.; Shi, R.; et al. Recent Advances in Data-Driven Design of Dual-Atom Catalysts. *Adv. Funct. Mater.* **2026**, *36*, e10647.
92. Sun, Q.; Yue, X.; Yu, L.; et al. Well-Defined Co_2 Dual-Atom Catalyst Breaks Scaling Relations of Oxygen Reduction Reaction. *J. Am. Chem. Soc.* **2024**, *146*, 35295–35304.
93. Ma, Y.; Liu, S.; Mao, J.; et al. Ligand-Restricted Synthesis of Highly Paired Dual-Atom Catalysts. *Nat. Mater.* **2026**, *25*, 80–90.
94. Zhou, A.; Zhao, C.; Dou, Y.; et al. Extension of Charge Separation Distance over Isolated Dual-Metal Sites in Metal-Organic Frameworks for Efficient CO_2 Photoreduction. *Appl. Catal. B Environ. Energy* **2025**, *372*, 125297.
95. Wang, J.; Liu, X.; Zhao, C.-X.; et al. A Post-Modification Strategy to Precisely Construct Dual-Atom Sites for Oxygen Reduction Electrocatalysis. *J. Energy Chem.* **2024**, *90*, 511–517.
96. Tang, T.; Wang, Z.; Guan, J. Structural Optimization of Carbon-Based Diatomic Catalysts towards Advanced Electrocatalysis. *Coord. Chem. Rev.* **2023**, *492*, 215288.
97. Chen, Y.; Lin, J.; Jia, B.; et al. Isolating Single and Few Atoms for Enhanced Catalysis. *Adv. Mater.* **2022**, *34*, 2201796.
98. Wang, H.; Wang, X.; Pan, J.; et al. Ball-Milling Induced Debonding of Surface Atoms from Metal Bulk for

Construing High-Performance Dual-Site Single-Atom Catalysts. *Angew. Chem. Int. Ed.* **2021**, *60*, 23154–23158.
99. Zhou, X.; Han, K.; Li, K.; et al. Dual-Site Single-Atom Catalysts with High Performance for Three-Way Catalysis. *Adv. Mater.* **2022**, *34*, 2201859.
100. Jin, X.; Chang, M.; Sun, H.; et al. Targeting Synthesis of Diatomic Catalysts by Selective Etching and Sequential Adsorption of Metal Atom. *J. Am. Chem. Soc.* **2025**, *147*, 2689–2698.
101. Zhang, Q.; Zhang, M.; Pan, Z.; et al. Seed-Mediated Engineering of Dual-Atom Ag-Pd Synergy on CeO_2 for Selective Transfer Hydrogenation of Nitroarenes. *Appl. Catal. B Environ. Energy* **2026**, *382*, 126019.
102. Gao, M.; Yang, G.; Shen, B.; et al. Engineering Zirconium Metal-Organic Frameworks for Selective Photocatalytic CO_2 Reduction to C_1/C_2 Fuels: A Critical Review. *Chem. Eng. J.* **2025**, *526*, 170896.
103. Hu, S.; Lei, Y.; Zhang, X.; et al. Recent Advances in Carbon Nitride Supported Single-Atom Catalysts: Synthesis, Characterization, and Applications for CO_2 Photoreduction. *ChemCatChem* **2024**, *16*, e202301684.
104. Hu, S.; Qiao, P.; Yi, X.; et al. Selective Photocatalytic Reduction of CO_2 to CO Mediated by Silver Single Atoms Anchored on Tubular Carbon Nitride. *Angew. Chem. Int. Ed.* **2023**, *62*, e202304585.
105. Yuan, L.-J.; Miao, Z.-Y.; Sui, X.-L.; et al. Janus Effect of FeCo Dual Atom Catalyst with Co as Active Center in Acidic Oxygen Reduction Reaction. *Nat. Commun.* **2025**, *16*, 7198.
106. Liu, Q.; Qiao, P.; Shen, D.; et al. Iron Clusters and Single Atom Sites Cooperatively Promote Bifunctional Oxygen Reaction Activity in Ultra-Stable Flexible Zinc–Air Batteries. *Energy Environ. Sci.* **2025**, *18*, 2839–2851.
107. Song, H.; Song, Z.; Zhou, W.; et al. XAFS Method for the Structural Characterization of Single Atom Catalysts. *Sci. China Chem.* **2025**, *68*, 2250–2274.
108. Zhang, T.; Song, W.; Wang, X.; et al. Lattice Coupling Enables Gradient Strain Tuning toward Platinum Skin at Intermetallic Nanocatalysts for Boosting Hydrogen Electrocatalysis. *Adv. Mater.* **2026**, *38*, e11865.
109. Chantler, C.T.; Bunker, G.; D'Angelo, P.; et al. X-Ray Absorption Spectroscopy. *Nat. Rev. Methods Primers* **2024**, *4*, 89.
110. Povia, M.; Herranz, J.; Binninger, T.; et al. Combining SAXS and XAS to Study the *Operando* Degradation of Carbon-Supported Pt-Nanoparticle Fuel Cell Catalysts. *ACS Catal.* **2018**, *8*, 7000–7015.
111. Li, Y.; Wang, H.; Chen, C.; et al. Ten Thousand Hour Stable Zinc Air Batteries via Fe and W Dual Atom Sites. *Nat. Commun.* **2025**, *16*, 8085.
112. Gu, Y.; Qiu, Z.; Lin, S.; et al. Extending Ambient Pressure X-Ray Photoelectron Spectroscopy to Plasma Studies: A Custom-Built Plasma Source Apparatus. *Rev. Sci. Instrum.* **2025**, *96*, 065203.
113. Jia, S.; Lin, X.; Huo, P.; et al. Polarized N^+-Mediated Charge-Transfer State Drives Two-Electron Water Oxidation. *Angew. Chem. Int. Ed.* **2026**, *65*, e18179.
114. Xu, Y.; An, Z.; Tang, Y. Recent Progress in Exploring Heterogeneous Catalyst Surface Chemistry with near Ambient Pressure XPS. *Sci. China Chem.* **2025**, *68*, 2867–2891.
115. Zhao, K.; Wu, D.; Wu, W.; et al. Identifying High-Spin Hydroxyl-Coordinated $Fe^{3+}N_4$ as the Active Centre for Acidic Oxygen Reduction Using Molecular Model Catalysts. *Nat. Catal.* **2025**, *8*, 422–435.
116. Shang, J.; Cao, H.; Ma, P.; et al. Visualizing Interfacial Charge Transfer of Two-Dimensional Heterostructure Photocatalyst for Efficient CO_2 Photoreduction via *in situ* Spectroscopies. *J. Energy Chem.* **2025**, *109*, 798–806.
117. Wang, Z.; Zou, G.; Park, J.H.; et al. Progress in Design and Preparation of Multi-Atom Catalysts for Photocatalytic CO_2 Reduction. *Sci. China Mater.* **2024**, *67*, 397–423.
118. Hu, S.; Qiao, P.; Liu, Z.; et al. Porous C_3N_4 Nanosheet Supported Au Single Atoms as an Efficient Catalyst for Enhanced Photoreduction of CO_2 to CO. *J. Catal.* **2024**, *432*, 115405.
119. Pan, M.; Zhang, T.; Dong, J.; et al. High-Throughput Screening and Interpretable Machine Learning for Rational Design of Bimetallic Catalysts for Methane Activation. *Adv. Sci.* **2026**, e24394. https://doi.org/10.1002/advs.202524394.
120. Mok, D.H.; Li, H.; Zhang, G.; et al. Data-Driven Discovery of Electrocatalysts for CO_2 Reduction Using Active Motifs-Based Machine Learning. *Nat. Commun.* **2023**, *14*, 7303.
121. Bian, Y.; Wang, Y.; Yang, Z.; et al. Accelerating the Prediction of G-C_3N_4-Supported Dual-Atom Catalysts for Photocatalytic CO_2 Reduction to CO and HCOOH: A Machine Learning and DFT Combined Approach. *Adv. Energy Mater.* **2025**, *15*, e03855.
122. Er, C.C.; Putri, L.K.; Ang, Y.S.; et al. Interpretable Machine Learning Framework: Predicting Catalytic Activities of Complex Photocatalysts towards CO_2 Conversion. *Mater. Today Phys.* **2025**, *57*, 101800.
123. Shen, Y.; Ren, C.; Zheng, L.; et al. Room-Temperature Photosynthesis of Propane from CO_2 with Cu Single Atoms on Vacancy-Rich TiO_2. *Nat. Commun.* **2023**, *14*, 1117.
124. Li, X.; Wang, M.; Wang, R.; et al. Construction of Ru Single-Atoms on Ceria to Reform the Products of CO_2 Photoreduction. *ACS Nano* **2024**, *18*, 5741–5751.
125. Cao, Y.; Guo, L.; Dan, M.; et al. Modulating Electron Density of Vacancy Site by Single Au Atom for Effective CO_2 Photoreduction. *Nat. Commun.* **2021**, *12*, 1675.
126. Chen, C.; Wu, M.; Xu, Y.; et al. Efficient Photoreduction of CO_2 to CO with 100% Selectivity by Slowing down Electron Transport. *J. Am. Chem. Soc.* **2024**, *146*, 9163–9171.
127. Si, S.; Shou, H.; Mao, Y.; et al. Low-Coordination Single Au Atoms on Ultrathin $ZnIn_2S_4$ Nanosheets for Selective Photocatalytic CO_2 Reduction towards CH_4. *Angew. Chem. Int. Ed.* **2022**, *61*, e202209446.
128. Li, Y.; Li, B.; Zhang, D.; et al. Crystalline Carbon Nitride Supported Copper Single Atoms for Photocatalytic CO_2 Reduction with Nearly 100% CO Selectivity. *ACS Nano* **2020**, *14*, 10552–10561.

129. Ran, L.; Li, Z.; Ran, B.; et al. Engineering Single-Atom Active Sites on Covalent Organic Frameworks for Boosting CO_2 Photoreduction. *J. Am. Chem. Soc.* **2022**, *144*, 17097–17109.
130. Xiong, X.; Mao, C.; Yang, Z.; et al. Photocatalytic CO_2 Reduction to CO over Ni Single Atoms Supported on Defect-Rich Zirconia. *Adv. Energy Mater.* **2020**, *10*, 2002928.
131. Wang, J.; Heil, T.; Zhu, B.; et al. A Single Cu-Center Containing Enzyme-Mimic Enabling Full Photosynthesis under CO_2 Reduction. *ACS Nano* **2020**, *14*, 8584–8593.
132. Li, H.; Gao, Y.; Xiong, Z.; et al. Enhanced Selective Photocatalytic Reduction of CO_2 to CH_4 over Plasmonic Au Modified g-C_3N_4 Photocatalyst under UV–Vis Light Irradiation. *Appl. Surf. Sci.* **2018**, *439*, 552–559.
133. Karmakar, S.; Barman, S.; Rahimi, F.A.; et al. Developing Post-Modified Ce-MOF as a Photocatalyst: A Detail Mechanistic Insight into CO_2 Reduction toward Selective C_2 Product Formation. *Energy Environ. Sci.* **2023**, *16*, 2187–2198.
134. Wang, G.; He, C.T.; Huang, R.; et al. Photoinduction of Cu Single Atoms Decorated on UiO-66-NH_2 for Enhanced Photocatalytic Reduction of CO_2 to Liquid Fuels. *J. Am. Chem. Soc.* **2020**, *142*, 19339–19345.
135. Hu, S.; Qiao, P.; Liang, X.; et al. Single-Atom Pt–N_4 Active Sites Anchored on Porous C_3N_4 Nanosheet for Boosting the Photocatalytic CO_2 Reduction with Nearly 100% CO Selectivity. *Appl. Catal. B Environ. Energy* **2024**, *346*, 123737.
136. Shi, X.; Huang, Y.; Bo, Y.; et al. Highly Selective Photocatalytic CO_2 Methanation with Water Vapor on Single-Atom Platinum-Decorated Defective Carbon Nitride. *Angew. Chem. Int. Ed.* **2022**, *61*, e202203063.
137. Bian, J.; Zhang, Z.; Feng, J.; et al. Energy Platform for Directed Charge Transfer in the Cascade Z-Scheme Heterojunction: CO_2 Photoreduction without a Cocatalyst. *Angew. Chem. Int. Ed.* **2021**, *60*, 20906–20914.
138. Zhao, Z.; Liu, W.; Shi, Y.; et al. An Insight into the Reaction Mechanism of CO_2 Photoreduction Catalyzed by Atomically Dispersed Fe Atoms Supported on Graphitic Carbon Nitride. *Phys. Chem. Chem. Phys.* **2021**, *23*, 4690–4699.
139. Zeng, D.; Wang, H.; Zhu, X.; et al. Single-Atom Copper Modified Hexagonal Tungsten Oxide for Efficient Photocatalytic CO_2 Reduction to Acetic Acid. *Chem. Eng. J.* **2023**, *451*, 138801.
140. Cheng, L.; Yue, X.; Wang, L.; et al. Dual-Single-Atom Tailoring with Bifunctional Integration for High-Performance CO_2 Photoreduction. *Adv. Mater.* **2021**, *33*, 2105135.
141. Wei, S.; Zhang, S.; Wang, H.; et al. Selective Photocatalytic CO_2 Reduction to C_2H_6 on a Ni–Au Diatomic Catalyst. *ACS Catal.* **2026**, *16*, 392–403.
142. You, X.-M.; Xu, B.; Zhou, H.; et al. Ultrahigh Bifunctional Photocatalytic CO_2 Reduction and H_2 Evolution by Synergistic Interaction of Heteroatomic Pt–Ru Dimerization Sites. *ACS Nano* **2024**, *18*, 9403–9412.
143. Li, W.; Liu, Z.; Rhimi, B.; et al. Nitrogen-Bridged S-N-Cu Sites for CO_2 Photoreduction to Ethanol with 99.5 % Selectivity in Pure Water. *Angew. Chem. Int. Ed.* **2025**, *64*, e202423859.
144. Hu, B.; Li, Z.; Wang, B.; et al. Construction of Co-In Dual Single-Atom Catalysts for Photocatalytic CO_2 Reduction into CH_4. *Appl. Catal. B Environ. Energy* **2025**, *371*, 125196.
145. Ou, H.; Ning, S.; Zhu, P.; et al. Carbon Nitride Photocatalysts with Integrated Oxidation and Reduction Atomic Active Centers for Improved CO_2 Conversion. *Angew. Chem. Int. Ed.* **2022**, *61*, e202206579.
146. Ma, X.; Chen, Q.; Han, C.; et al. Synergistic Optimization of Morphology and Vacancies on Diatomic Rhodium Catalysts Dispersed on Carbon Nitride for Efficient Photocatalytic Reduction of CO_2. *Adv. Funct. Mater.* **2024**, *34*, 2307733.
147. Xie, Z.; Xu, S.; Li, L.; et al. Well-Defined Diatomic Catalysis for Photosynthesis of C_2H_4 from CO_2. *Nat. Commun.* **2024**, *15*, 2422.
148. Jia, G.; Sun, M.; Wang, Y.; et al. Asymmetric Coupled Dual-Atom Sites for Selective Photoreduction of Carbon Dioxide to Acetic Acid. *Adv. Funct. Mater.* **2022**, *32*, 2206817.
149. Du, H.; Fu, Y.; Shi, R.; et al. Spatially Separated C–C Coupling and Protonation on Cl-Bridged Ti–Ag Dual-Site Catalysts for Efficient Photocatalytic CO_2 Reduction to C_2H_4. *Angew. Chem. Int. Ed.* **2026**, *65*, e20354.
150. Cui, Y.; Wang, Y.; Ma, Y.; et al. A Chiral Mesostructured Photocatalyst for Efficient Solar-Driven CO_2 Reduction to Ethanol. *Nat. Synth.* **2026**, *5*, 117–128.
151. Song, W.; Song, B.; Liang, Y.; et al. Precise Dual-Metal Pairs Enable Ultrafast Structural Response for CO_2-to-Ethylene Photoconversion. *J. Am. Chem. Soc.* **2025**, *147*, 39505–39515.
152. Zhou, M.; Wang, Z.; Mei, A.; et al. Photocatalytic CO_2 Reduction Using La-Ni Bimetallic Sites within a Covalent Organic Framework. *Nat. Commun.* **2023**, *14*, 2473.
153. Wang, J.; Zhu, W.; Meng, F.; et al. Integrating Dual-Metal Sites into Covalent Organic Frameworks for Enhanced Photocatalytic CO_2 Reduction. *ACS Catal.* **2023**, *13*, 4316–4329.
154. Tang, J.; Wang, Q.; Ran, M.; et al. Low-Coordinated CuNi Dual-Atom Catalyst for Efficient Flue Gas CO_2-to-C_2H_6 Photoreduction. *Nat. Commun.* **2026**, https://doi.org/10.1038/s41467-026-77025-x.
155. Li, P.; Qi, Z.; Yan, D. Rare Earth Er-Nd Dual Single-Atomic Catalysts for Efficient Visible-Light Induced CO_2 Reduction to $C_nH_{2n+1}OH$ (N = 1, 2). *Angew. Chem. Int. Ed.* **2024**, *63*, e202411000.
156. Shi, H.; Wang, H.; Zhou, Y.; et al. Atomically Dispersed Indium-Copper Dual-Metal Active Sites Promoting C-C Coupling for CO_2 Photoreduction to Ethanol. *Angew. Chem. Int. Ed.* **2022**, *61*, e202208904.
157. Huang, T.; Han, J.; Lu, B.; et al. Electrophile–Nucleophile Paired Heteronuclear Dual-Site for Selective CO_2 Photoreduction to Ethanol via Oxygen-Tethered Asymmetric C–C Coupling. *Angew. Chem. Int. Ed.* **2026**, *138*, e3999411.

158. Zhang, L.; Zhang, J.; Yu, J. Energy Conversion and Loss in Heterojunction Photocatalysts. *Chem* **2026**, *12*, 102719.
159. Dong, X.-Y.; Wang, H.; Zhang, X.-D.; et al. Research Progress on Semiconductor-Based Photocatalytic Hydrogen Peroxide Synthesis. *Chin. Sci. Bull.* **2025**, *70*, 816–834.
160. Meng, Z.; Zhang, J.; Long, H.; et al. Kelvin Probe Force Microscopy Reveals Spatially Resolved Charge-Transfer Mechanism in CdS/BiOBr S-Scheme Heterojunction Photocatalyst. *Angew. Chem. Int. Ed.* **2025**, *64*, e202505456.
161. Chen, Y.; Lin, J.; Pan, Q.; et al. Inter-Metal Interaction of Dual-Atom Catalysts in Heterogeneous Catalysis. *Angew. Chem. Int. Ed.* **2023**, *62*, e202306469.
162. Xiao, M.; Sun, H. Structure, Synthesis and Application of Carbon Based Double Single Atom Catalysts. *Desalination* **2025**, *606*, 118762.
163. Ma, C.; Zhong, X.; Guan, Y.; et al. Tunable-Crystallinity N-Doped Carbon Supports Synergizing with Fe Active Sites for Efficient Nitrate Electroreduction. *Appl. Catal. B Environ. Energy* **2026**, *384*, 126223.
164. Li, Q.; Jiao, Y.; Tang, Y.; et al. Shear Stress Triggers Ultrathin-Nanosheet Carbon Nitride Assembly for Photocatalytic H_2 O_2 Production Coupled with Selective Alcohol Oxidation. *J. Am. Chem. Soc.* **2023**, *145*, 20837–20848.
165. Wang, Y.; Su, B.; Wang, S.; et al. Ultralow-Content PdCu Disordered Nanoalloys on Carbon Nitrides for Unity-Selective CO_2 Hydrogenation to Methanol. *Angew. Chem. Int. Ed.* **2025**, *64*, e202508611.
166. Zang, Z.G.; Cai, W.S.; Zhou, Y. Metal Oxide Semiconductors: State-of-the-Art and New Challenges. In *Metal Oxide Semiconductors: Synthesis, Properties, and Devices*; Wiley: Weinheim, Germany, 2024; pp. 1–13.
167. Ren, C.; Li, Q.; Ling, C.; et al. Mechanism-Guided Design of Photocatalysts for CO_2 Reduction toward Multicarbon Products. *J. Am. Chem. Soc.* **2023**, *145*, 28276–28283.
168. Huang, J.-R.; Chen, H.-Y.; Zhu, H.-L.; et al. Ni–Zn Dual-Atom Sites Enable Synergistic Parallel Pathways for Efficient Photosynthesis of H_2O_2 with Long-Term Stability. *J. Am. Chem. Soc.* **2025**, *147*, 37167–37175.
169. Liu, B.; Cheng, M.; Zhang, C.; et al. Au-Cu Dual-Single-Atom Sites on Bi_2WO_6 with Oxygen Vacancy for CO_2 Photoreduction towards Multicarbon Products. *Appl. Catal. B Environ. Energy* **2024**, *357*, 124263.
170. Zhu, Q.; Xu, Q.; Du, M.; et al. Recent Progress of Metal Sulfide Photocatalysts for Solar Energy Conversion. *Adv. Mater.* **2022**, *34*, 2202929.
171. Zhao, E.; Gao, L.; Yang, S.; et al. *In Situ* Fabrication of 2D SnS_2 Nanosheets as a New Electron Transport Layer for Perovskite Solar Cells. *Nano Res.* **2018**, *11*, 5913–5923.
172. Zhang, Y.; Johannessen, B.; Zhang, P.; et al. Reversed Electron Transfer in Dual Single Atom Catalyst for Boosted Photoreduction of CO_2. *Adv. Mater.* **2023**, *35*, 2306923.
173. Li, S.; Shang, H.; Tao, Y.; et al. Hydroxyl Radical-Mediated Efficient Photoelectrocatalytic NO Oxidation with Simultaneous Nitrate Storage Using a Flow Photoanode Reactor. *Angew. Chem. Int. Ed.* **2023**, *62*, e202305538.
174. Yang, H.; Liu, G.; Zheng, L.; et al. Cu-Fe Bimetallic MOFs with Long Lifetime Separated-State Charge for Enhancing Selectivity for CO_2 Photoreduction to CH_4. *Appl. Catal. B Environ. Energy* **2024**, *359*, 124491.
175. Chen, X.; Zhao, J.; Li, G.; et al. Recent Advances in Photocatalytic Renewable Energy Production. *Energy Mater.* **2022**, *2*, 200001. http://dx.doi.org/10.20517/energymater.2021.24.
176. Wu, Z.; Guo, Y.-R.; Ma, X.-L.; et al. Dual Regulation of Reduction and Oxidation Center in Metal-Organic Frameworks to Boost CO_2 Photoreduction. *Angew. Chem. Int. Ed.* **2025**, *64*, e202514515.
177. Li, Q.; Li, X.; Zhang, B.; et al. Recent Advancements in COFs-Based Heterostructures for CO_2 Photoreduction. *Adv. Funct. Mater.* **2025**, *35*, 2506421.